La Rivista del Nuovo Cimento
https://doi.org/10.1007/s40766-022-00033-2

REVIEW PAPER

Gamma-ray spectroscopy of fission fragments with state-of-the-art techniques

S. Leoni[1,2] · C. Michelagnoli[3] · J. N. Wilson[4]

Received: 21 December 2021 / Accepted: 2 March 2022

Abstract

The paper reviews recent developments in γ-ray spectroscopy of the neutron-rich fragments produced in nuclear fission. This subject has been an intensive area of study spanning more than five decades. Here we highlight key results and describe the evolution of the associated experimental techniques since the last review papers in 1995 (I. Ahmad and W.R. Phillips, Rep. Prog. Phys. 58(11), 1415 (1995); J. H. Hamilton et al., Prog. Part. Nucl. Phys. 35, 635(1995)). Research themes in nuclear structure will be explored along with the fission reaction mechanism and the links to nuclear astrophysics and applications.

Keywords Fission · γ-ray spectroscopy · Nuclear structure and reaction · Nuclear astrophysics and applications

Contents

✉ S. Leoni
Silvia.leoni@mi.infn.it

1 Dipartimento di Fisica, Università degli Studi di Milano, 20133 Milan, Italy

2 INFN sezione di Milano via Celoria 16, 20133 Milan, Italy

3 Institut Laue-Langevin (ILL), 71 Avenue des Martyrs, 38042 Grenoble, France

4 Université Paris-Saclay, CNRS/IN2P3, IJC Laboratory, Orsay, France

Published online: 21 June 2022

1 Introduction

Nuclear fission, where a heavy nucleus splits into two lighter nuclei, is a complex dynamical process. The resulting fission fragments contain many more neutrons than stable nuclei and hence it is a useful reaction mechanism for producing and studying nuclei far from stability. The excited fragments decay by emission of both neutrons and γ rays, and the γ rays in particular carry important information on both the nuclear reaction process and the structure of the exotic nuclei that are decaying.

Spectroscopy of the γ rays emitted during nuclear fission is an experimental technique that has undergone a series of major technical developments during a period spanning over 50 years [3, 4]. The detection of the γ rays emitted from the rapidly cooling fission fragments produced in this reaction is useful for at least two main purposes:

1. Firstly, since fission generates a multitude of excited, unstable, neutron-rich nuclei, spectroscopy of the γ rays emitted as they de-excite gives important information on the nuclear structure of these nuclei. Such exotic fragments are the precursors of the stable nuclei encountered here on earth, which in the wider universe are only produced in extreme astrophysical environments (e.g., supernova, neutron-

start mergers, etc.). Fission allows these nuclei to be accessed and studied in the laboratory.
2. Secondly, the fission reaction mechanism itself is a dramatic rearrangement of nuclear matter and hence interesting to study. The nuclear shape, unstable to Coulomb forces, passes through configurations at extreme deformations before splitting (scission) occurs, giving birth to two new fragments. Gamma-ray spectroscopy can be used to extract probabilities for the production of particular nuclei (i.e., to measure fission yields), and also offers unique information on the excitation energy and angular momentum of the decaying fragments which can help to understand this complex nuclear process.

In this review we aim to give an overview of the use of the γ-ray spectroscopy techniques to gain insights into both the structure of neutron rich nuclei (Sect. 2) and the fission process itself (Sect. 5), with implications for nuclear astrophysics (Sect. 3) and detection of extremely rare decays, e.g., fission shape-isomers (Sect. 4). We aim to describe the current state-of-the-art for both direct and inverse kinematics setups using the most neutron-rich fission reaction mechanisms (Sect. 7) at different facilities, and the link to applications (Sect. 6). We also aim to suggest future research avenues that might be worth pursuing (Sect. 8). We begin with a brief historical overview which has been covered in more detail in previous review papers [1, 2] from the 1990's, to put in context the more recent developments.

1.1 Spectroscopy of fission fragments with the first low-volume Ge detectors

Since hundreds of different fission fragments are produced and each nucleus emits multiple cascades of characteristic γ rays, many thousands of discrete transitions need to be resolved within an energy range of typically 50 keV to 2 MeV. The strongest emission lines have intensities which are at maximum around 2–3 percent of the total γ yield. Hence, an attempt to resolve even the strongest transitions requires a detector with an excellent resolution of less than a few keV. The first detectors of this type were germanium and silicon semiconductor detectors, a technology first developed in the early 1960's [5, 6]. These first groundbreaking detectors had very low efficiency due to the very small detector volumes available at that time (around $1\,\mathrm{cm}^3$). This technological advance opened the door to the detailed spectroscopy of excited nuclei in general and of nuclear fission in particular. The first ever spectrum of spontaneous fission is shown in Fig. 1 [7], where the 477 keV (4^+ - 2^+ transition of the strongly produced fragment ^{140}Xe) is correctly identified at a mass asymmetry of 1.3 for heavy/light fragments detected in the experiment. In the early 1970's these detectors were exploited in a number of ingenious experiments to not only characterize the main transitions in many neutron-rich nuclei (discovery of rotational bands), but also to gather information on excited state lifetimes and identify new regions of deformation and the existence of rotational bands (e.g., in neutron rich Ba, Ce, Zr and Mo nuclei) [8, 9]

Meanwhile, the detection of the unique signatures of individual fragments via their γ decay and the measurement of the relative intensities of the transitions was recognized as a method via which to determine fission product yields. The first experiment

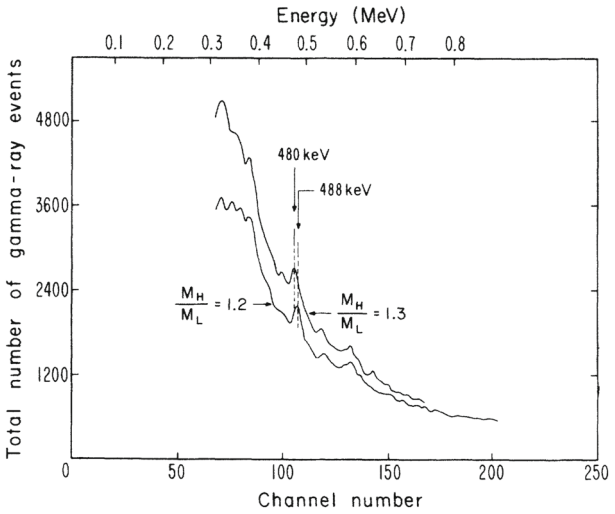

Fig. 1 The first published high-resolution γ-ray spectrum from fission using a low-volume Ge detector and mass selection (taken from [7])

of this type was performed in the early 1970's [10]. Additionally, interesting information on the fission process was also forthcoming [11]. The discovery of angular correlations between the emission direction of γ rays and fission fragments suggested that the angular momentum in fission is generated perpendicular to the fission axis.

1.2 Gamma-ray coincidence spectroscopy of fission fragment decays

The next phase of discoveries had to wait for new technological advances to arrive in the mid 1980's, when large-volume germanium detectors ($> 50\,\mathrm{cm}^3$) were developed and led to the possibility to perform high resolution γ-γ coincidence spectroscopy of fission, provided that enough detectors were placed together in the same setup to achieve a total photo-peak efficiency of around 1%. Since the average number of γ rays emitted in fission is around 8, the probability of detecting significant numbers of events where two γ rays are detected in coincidence became feasible.

Arrays of between 10 and 15 germanium detectors were assembled at Argonne and Oak Ridge laboratories and used to study γ-ray emission from spontaneous fission sources. The extra selection power gained by using γ–γ coincidence techniques allowed for a much more comprehensive spectroscopy. Instead of typically a few yrast transitions, both yrast and non-yrast structures, side bands, etc., became visible for the first time and led to the discovery for example of new phenomena such as octupole correlations in Ba and Ce nuclei [12, 13]. Moreover, coincidence techniques allowed understanding of angular momentum effects with measurements of average spins as a function of fragment mass determined for heavy-ion induced fission reactions [1, 14, 15]. More accurate determination of fission yields in spontaneous fission [16] also became possible.

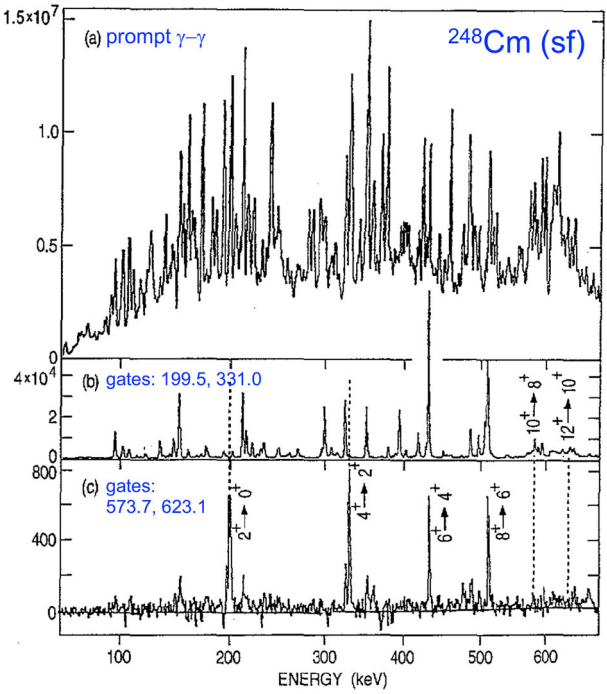

Fig. 2 Gamma-ray spectra produced in the spontaneous fission of ^{248}Cm and measured with the EUROGAM array. Panel (**a**): all prompt γ rays (triple coincidences). Panel (**b**): spectrum gated on the two lowest transitions of ^{144}Ba (i.e., $2^+ \rightarrow 0^+$, and $4^+ \rightarrow 2^+$). Panel (**c**): spectrum gated on the $12^+ \rightarrow 10^+$ and $10^+ \rightarrow 8^+$ transition of ^{144}Ba. Gating energies are given in the legend of each panel. The ^{144}Ba fragment has a fission yield of $\approx$3%. (Adapted from [1])

1.3 The advent of large Ge arrays to study fission

A new development phase in experimental techniques began in the early 1990's and continued for the subsequent two decades. The advent of very high efficiency Compton suppressed spectrometers such as GAMMASPHERE and EUROBALL [17–21] achieved unprecedented sensitivity and resolving power through the use of many (> 100) high-volume Compton-suppressed Ge detectors ($> 300\,\text{cm}^3$). The high detection efficiency of up to 10 percent allowed high-statistics experiments of triple γ-ray coincidences to be performed. Figure 2 shows an example of the quality of data which could be obtained with EUROGAM, a pre-EUROBALL array [7].

Triple γ-ray coincidences contain richly correlated spectroscopic information and allow separation of weakly populated γ-ray cascades with transitions as weak as 10^{-5} of the total fission yield. This permitted more-detailed spectroscopic studies of very weakly populated neutron-rich nuclei, particularly using spontaneous fission and heavy-ion induced fission reactions (eg., ^{12}C, ^{18}O, ^{48}Ca and ^{64}Ni beams at few MeV/u on U and Pu targets, see Table 1 of Sec. 7). Measurements of nuclear moments of neutron-rich fission fragments were also attempted for the first time [22, 23].

However, the use of triple γ coincidences already requires knowledge of transitions in these nuclei from previous experiments. Furthermore, the pure spectroscopic technique began to approach its limits. The background, in the case of pure fission spectroscopy, arises from the "sea" of many thousands of transitions emitted from the many hundreds of fragments produced in the reaction. It becomes progressively harder to resolve weaker transitions, particularly from the most weakly populated neutron-rich nuclei. To advance further requires using fission reactions which are naturally more neutron rich, or deploying techniques to achieve a degree of selectivity in mass to reduce (or ideally eliminate) the background of transitions from other nuclei.

1.4 Microseconds isomer-decay spectroscopy

Complementary to prompt γ measurements (or β-decay experiments) with large detector arrays, such as EUROBALL or GAMMASPHERE, the study of γ decays of microsecond isomers has also been a very powerful tool to access nuclear structure information for nuclei very far from the stability line [24, 25]. Such long-lived states have been measured in the past in experiments employing thermal neutrons from reactors, impinging on thin or thick U or Pu targets, and spectrometer for efficient selection of the reaction products of interest. The detection of the isomer decay is based on event-by-event time correlation between the fragments and the delayed γ-rays or conversion electrons. Pioneering work was performed with such techniques at the OSIRIS facility in Studsvik (Sweden) [26], and at the recoil fragment spectrometers JOSEF, in Julich (Germany) [27], and LOHENGRIN, at Istitut Laue-Langevin [28] in Grenoble (France), where this vital research program is still ongoing.

1.5 More recent developments

During the last two decades or so, two new technical developments have been pursued in parallel. The first is the exploitation of neutron-induced reactions (both thermal and fast) to access lighter and more neutron-rich nuclei than are accessible with spontaneous fission [29–31]. The second development is the exchange of direct kinematics fission reactions for inverse kinematics to facilitate an unambiguous identification of fragments in mass and charge at the focal plane of separators [32–35]. A rich γ-spectroscopy program can be carried out, for example, for isomeric states in the stopped fragments, with intrinsic Ge energy resolution (see Sect. 2.6). For facilities which use relativistic beams (e.g., RIKEN and GSI), fission fragments can further be used to perform secondary reactions. However, this is beyond the scope of this review.

The availability of new halide scintillator materials, such as $LaBr_3$(Ce) and $CeBr_3$, has also opened up the possibility to perform fast timing measurements to extract direct information on the lifetimes of short-lived nuclear states and the associated nuclear moments.

Details on these more recent developments can be found in the Technical Aspects Sect. 7.

2 Nuclear structure

The spectroscopic study of the excited states of any particular nucleus on the nuclear chart is limited by the available production mechanisms. For this reason only about 3000 or so of the 7000 isotopes that can theoretically exist are currently amenable to study. Since the valley of stability has a curvature favoring nuclei with higher N/Z ratios with increasing mass, nuclear fission is a very important reaction mechanism for the production and subsequent study of neutron-rich nuclei. When a heavy nucleus splits into two, the resulting nuclei are significantly more neutron-rich than stable isotopes with the same Z. The Q-value of the reaction is strongly positive (typically 200 MeV), i.e., the process is strongly exothermic. While the largest portion of energy goes into the Coulomb repulsion of the fragments, a significant amount of energy (30–40 MeV) ends up as internal excitation of the fragments which is released in the subsequent decay process via prompt neutron and γ-ray emission. Fragments are typically populated at moderate spins, around 6–12 $\hbar$.

Fission typically produces several hundred isotopes at significant levels, with fission yields which vary considerably with the fissioning system A and Z, and E^*, the excitation energy of the compound nucleus. For fissioning systems in the actinide region, neutron rich fragments from a lower limit of $Z = 28$ (Ni isotopes) and the upper limit of around $Z = 64$ (Gd isotopes) are accessible. Over the past several decades, a large body of experimental information has already been built up for numerous fission fragments produced via a wide variety of fission mechanisms, as described in Sect. 5.

In this review, we focus on γ-ray spectroscopy investigations which probe yrast or near-yrast structures of secondary fission fragments, produced after neutron emission. Spectroscopy of daughter nuclei populated after β-decay will be only briefly mentioned, as a complementary production mechanism which usually populates different sets of states at much lower spin.

A number of examples will be given of detailed investigations usually profiting from combined information from various data sets obtained with different instruments (e.g., HPGe arrays, stand-alone or coupled with fission fragments spectrometers, active targets, etc...). This will demonstrate the great potential of fission studies performed with state-of-the-art setups currently available (see Sect. 7).

Figures 3 and 4 shows the (N,Z) portions of the nuclear chart in the high- and low-mass peaks associated to fragments post-neutron emission from ^{252}Cf spontaneous fission (as a reference case for discussion). Mass numbers are given for nuclei specifically mentioned in this review. Outlined regions indicate major nuclear structure topics which are addressed by fission studies employing the reaction mechanisms summarized in Table 1 of Sect. 7. They comprise, in particular, (i) the study of single particle levels and residual interactions around doubly magic ^{132}Sn and towards doubly magic ^{78}Ni, (ii) couplings with core excitations (around doubly magic ^{132}Sn, in particular) (iii) the evolution of nuclear shapes along isotopic chains, and the appearance of shape-coexistence phenomena, (iv) triaxiality and collective phonon excitations, (v) higher-order of deformation, in particular octupole shapes, and (vi) isomer spectroscopy studies. In the following sections, selected examples for each topic will be presented from the vast literature accumulated over the last three decades of fission fragment γ-spectroscopy investigations. We will show how the gathering of cumulative

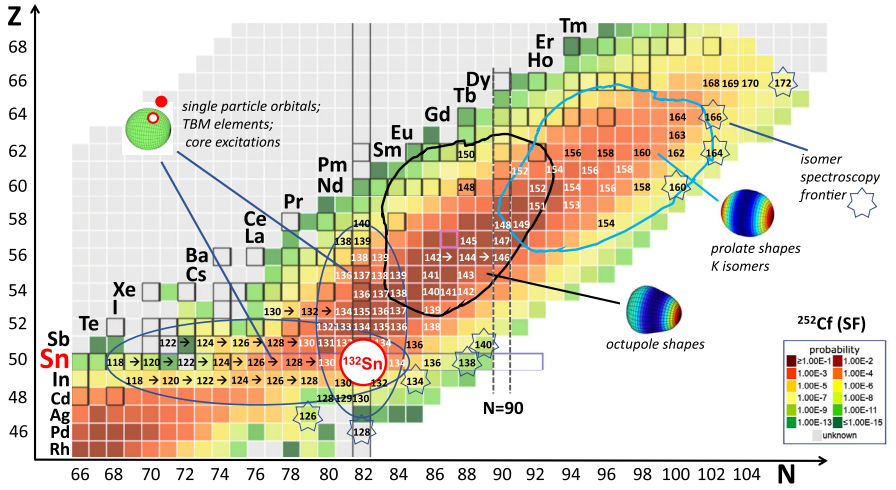

Fig. 3 Portion of the nuclear chart focusing on the high-mass peak associated to post-neutron emission fragments from ^{252}Cf spontaneous fission (with yields given in the legend). The outlined regions point to nuclear structure topics discussed in this work. Mass numbers are given for nuclei explicitly mentioned. Arrows indicate isotopic chains systematically investigated in fission experiments. (Adapted from NNDC [36])

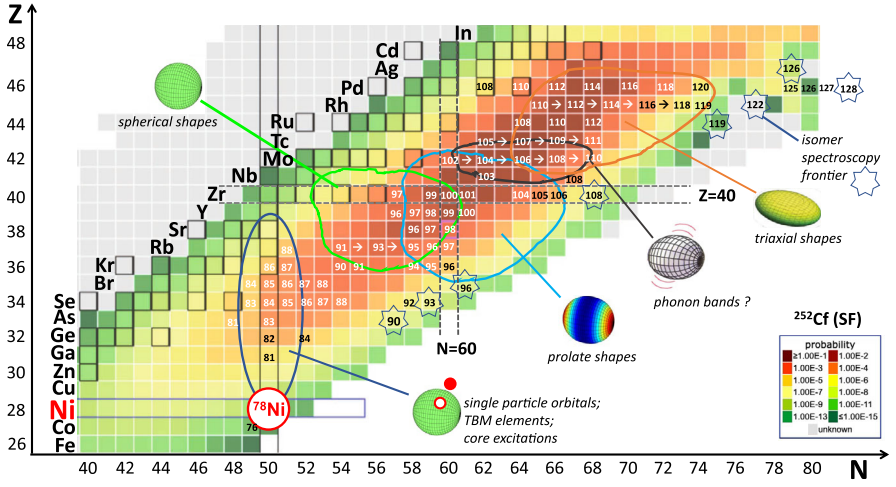

Fig. 4 Same as Fig. 3, for the low-mass peak associated to post-neutron emission fragments from ^{252}Cf spontaneous fission. (Adapted from NNDC [36])

experimental information on these phenomena has given strong guidance to nuclear structure theory. Moreover, the knowledge of properties of neutron-rich nuclei in these mass regions has also had a significant impact on understanding the synthesis of heavy elements in astrophysical processes, as briefly discussed in Sect. 3.

2.1 Single particle levels and residual interactions around shell closures

Nuclei in the vicinity of shell closures are of primary importance to determine the most basic ingredients of shell model calculations, namely single-particle energies (SPE) and two-body matrix elements (TBME) of the nucleon-nucleon interaction [37, 38]. Indeed, in such systems, states at low excitation energy are usually formed by a few valence nucleons in a small number of orbits, while the magic core can often be considered in its ground state, acting as a spectator. Furthermore, particle-hole excitations in which one nucleon is promoted across the shell gap can be very efficiently used to establish the size of the gap, an essential characteristic to assess the robustness of a shell closure. In the following section, we concentrate on nuclei in the vicinity of *i)* ^{132}Sn (i.e., in the neighborhood of the $Z = 50$ and $N = 82$ shell closures), and of *ii)* $N = 50$. Both regions have been extensively investigated in spectroscopic studies of fission fragments of actinides (see Fig. 3 and 4).

2.1.1 The ^{132}Sn doubly magic shell closure

The doubly magic nucleus ^{132}Sn is produced with a significant yield in asymmetric fission of actinides. This has allowed extensive spectroscopic investigations in the neighborhood of ^{132}Sn, providing strong benchmarks for shell model calculations, together with complementary information obtained from β-decay studies. As shown in Fig. 5, the Z = 50 shell gap is formed between the proton $g_{9/2}$ and $d_{5/2}$ or $g_{7/2}$ orbits, while the $N = 82$ shell closure is given by the $h_{11/2}$ (or the nearby $s_{1/2}$ and $d_{3/2}$) and the $f_{7/2}$ orbit. This neutron shell closure is so strong that seven $N = 82$ isotones with $54 < Z < 62$ are stable [37].

In high-statistics experiments with large arrays (e.g., EUROBALL [18, 19] and GAMMASPHERE [4, 21]), using in particular ^{248}Cm fission sources, multi-fold γ coincidences have been employed to identify yrast cascades in a number of nuclei around ^{132}Sn, often exploiting prompt and delayed cross coincidences with known γ rays from fission partners. Such experimental approaches have contributed to accessing key ingredients for shell model interpretations, such as single-particle energies, mainly at the highest spins, from the analysis of one-valence particle/hole nuclei (see Fig. 6). This is the case of the $d_{5/2}$ and $h_{11/2}$ proton orbitals above Z = 50, from the study of ^{133}Sb [46], and of the $h_{9/2}$ and possibly $i_{13/2}$ neutron orbitals above $N = 82$, from ^{133}Sn investigations [47]. Information on the energies of low-spin nucleonic orbitals has very often been obtained from fission fragments spectroscopy after β decay ([48–51] and references therein), complementing more traditional studies based on transfer reactions (e. g., for ^{133}Sn: [52, 53]). We note that only limited information on single-particle energies is currently available in the region of doubly magic ^{78}Ni, mainly obtained from in-flight fission of ^{238}U, at relativistic energies. This is due to the lower fission yields around mass A=80, with respect to the ^{132}Sn region [36, 39] (see Fig. 5 and Sect. 2.1.2).

The excitation spectrum of doubly magic ^{132}Sn, itself, has been extensively investigated in spontaneous fission experiments: the first three states, the 2^+ at 4041 keV, the 3^- at 4352 keV and the 4^+ at 4416 keV, have been interpreted as phonon excitations with a sizable collectivity (i.e., ∼7, 17 and 4.4 W.u., respectively) [55, 60], while the

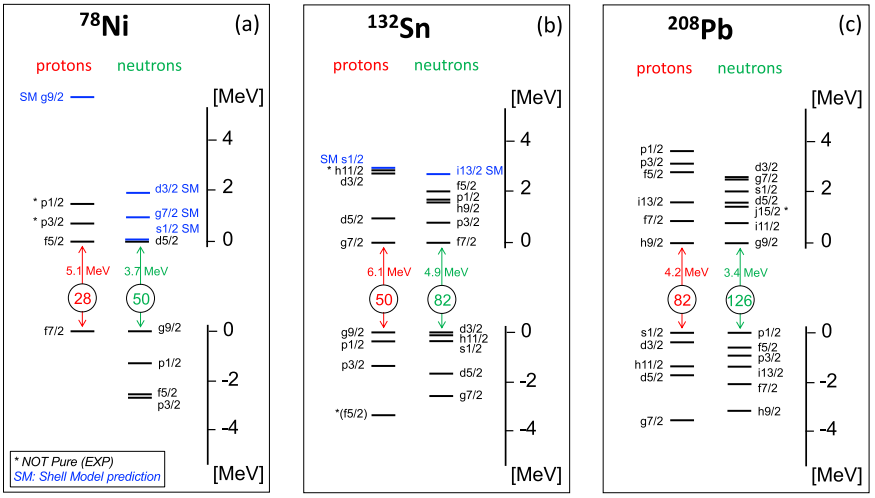

Fig. 5 Experimental single-particle proton and neutron energies for the doubly magic ^{78}Ni (**a**), ^{132}Sn (**b**) and ^{208}Pb (**c**) [36]. States assigned in experimental studies, but considered of not pure single-particle character, are marked by * [37, 39–41], predictions from Shell Model calculations are displayed by blue color and labeled by SM [42–44]. The size of the proton and neutron shell gaps are given in MeV. Information on single-particle states for ^{78}Ni and ^{132}Sn have been partially obtained from fission studies (see, e.g., Fig. 6). Single-particle energies for ^{208}Pb are shown for comparison purposes. See text and Refs. [37, 38, 45] for additional discussions

other states have one-particle-one-hole (*1p-1h*) character (see Fig. 7). In particular, all members of the $f_{7/2}\, h_{11/2}^{-1}$ multiplet (with spin 2^+ to 9^+), resulting from excitations across the neutron shell gap, have been identified between 4 and 5 MeV, as well as the 4^- and 5^- excitations of $f_{7/2}\, d_{3/2}^{-1}$ nature, located at 4831 and 4942 keV, respectively [59].

Being the lowest core excitations of ^{132}Sn located above 4 MeV (what supports a strong shell closure for both protons and neutrons), it follows that in nuclei close to ^{132}Sn, states up to few MeV of excitation energies are expected to be very well described by the motion of valence nucleons only. A vast literature exists on the study of states arising from the couplings among specific valence particles in the neighborhood of ^{132}Sn. For examples, in the $N = 83$ isotones of ^{134}Sb, ^{135}Te and ^{136}I [61–63], with two, three and four valence particles, respectively, information on high-spin states arising from $g_{7/2}$, $d_{5/2}$, $h_{11/2}$, $f_{7/2}$, $h_{9/2}$ orbitals were obtained (see Fig. 5b). In the $N = 81$ isotones of ^{132}Sb and ^{133}Te [54, 64], characterized by two and three valence particles, excitations were explained in terms of proton-neutron hole states, as well as *2p-2h* excitations (in ^{132}Sb). In the $N = 84$ two-valence-neutron nucleus ^{134}Sn, the $(f_{7/2})^2$ multiplet was identified up to a 6^+ isomeric state at 1246 keV [65], while yrast states in the two- and three-proton $N = 82$ isotones ^{134}Te and ^{135}I, located up to above 5.5 MeV, were interpreted in terms of valence proton and particle-hole core excitations [66]. By employing fusion- and transfer-induced fission of ^{238}U at 6.2 MeV/u the structure of ^{132}Te ($N = 80$), with two proton particles and two neutron holes outside of the ^{132}Sn doubly magic core, has been recently extended up

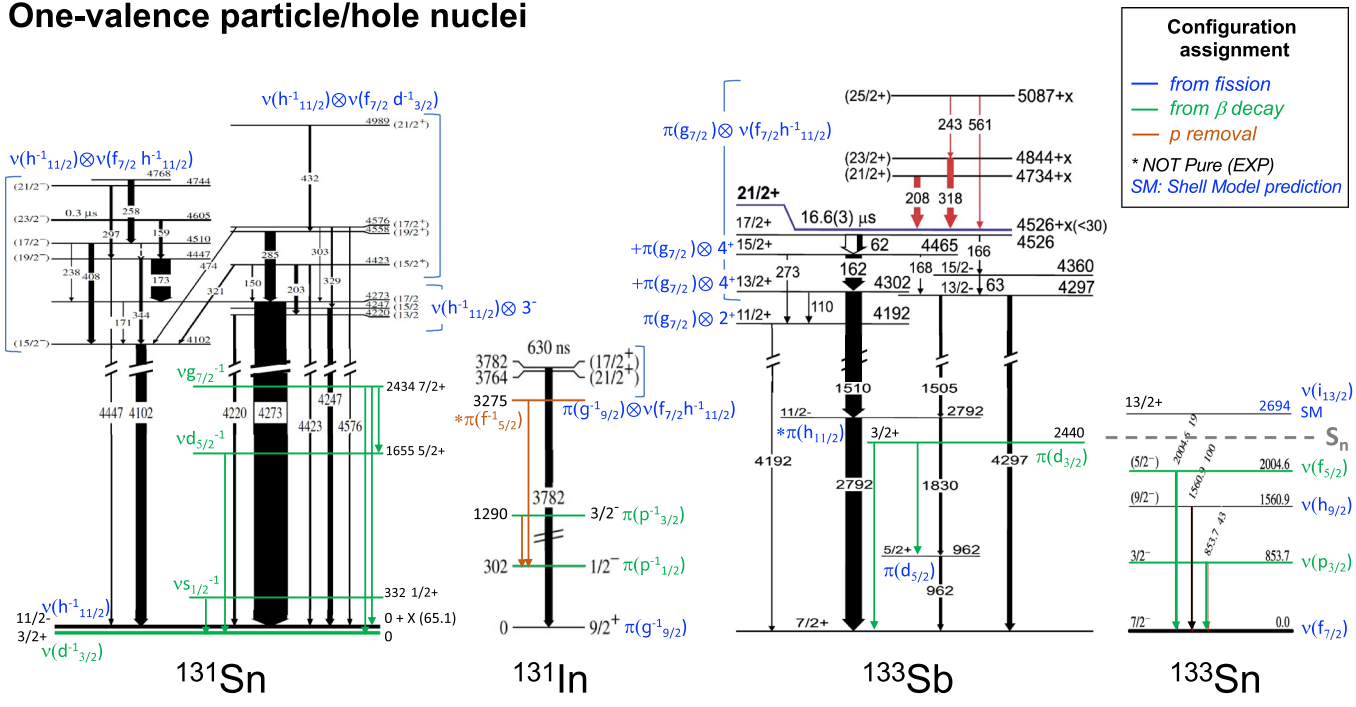

Fig. 6 Partial level schemes of one-valence particle/hole nuclei around doubly magic ^{132}Sn. Configurations are given for single-particle/hole states and for members of multiplets arising by the coupling of the odd particle/hole to collective as well as particle-hole excitations of the ^{132}Sn core (see also Figs. 5 **(b)** and 7). Configurations established from fission studies are shown in blue/black, while single-particle states obtained from β-decay investigations are displayed in green. For completeness, the $\pi(f_{5/2}^{-1})$ proton-hole state of ^{131}In is also shown, as follows from single-proton removal reaction studies. Both the $\pi(f_{5/2}^{-1})$ and $\pi(h_{11/2})$ excitations of ^{131}In and ^{133}Sb, marked by *, are considered to not be pure, while the energy of the $\nu(i_{13/2})$ excitation in ^{133}Sb is deduced from shell model extrapolations [36, 37, 40, 47, 51, 54–58]. See Fig. 5 **(b)** for single-particle energies. (Adapted from [36] and [54, 55, 58])

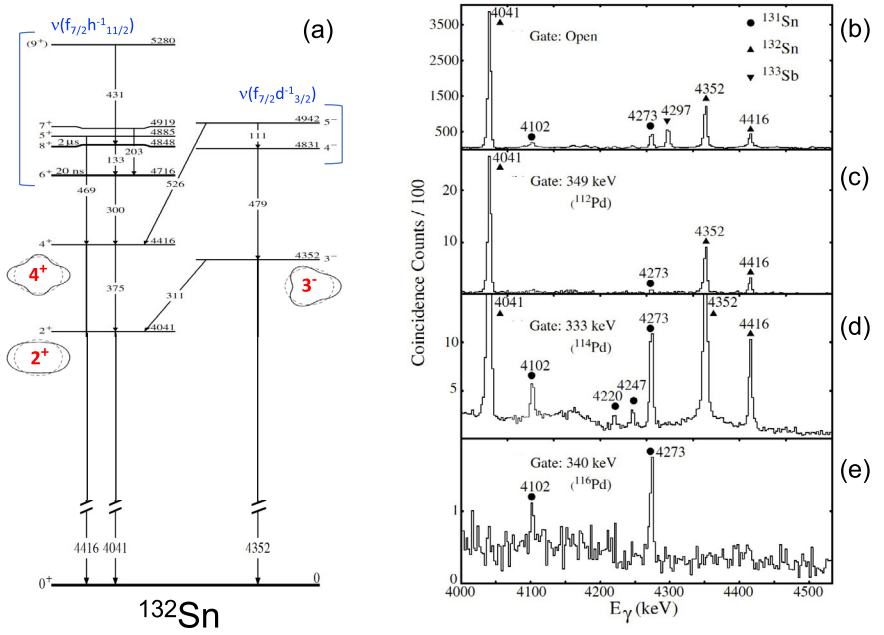

Fig. 7 Panel **(a)**: Level schemes for ^{132}Sn, showing the yrast γ-ray cascades observed with the GAMMASPHERE array, following spontaneous fission of ^{248}Cm. Cartoons illustrate the phonon nature of the 2^+, 3^- and 4^+ states, while higher-lying multiplets originate from the indicated single particle-hole excitations. Panels **(b)**-**(e)**: Gamma-ray spectra above 4 MeV, from the ^{248}Cm fission source, obtained requiring the conditions given in each panel (i.e., no condition in **(b)**, coincidence with Pd fission partners in **(c)**-**(e)**). Strong transitions from ^{131,132}Sn and ^{133}Sb are marked by labels. (Adapted from [59])

to spin 17 and excitation energy of 6.17 MeV, with positive-parity states, above 10^+, expected to be dominated by particles in the high-j orbitals lying close to the Fermi surface, and corresponding to the $\pi g_{7/2}^2$, and the $\nu h_{11/2}^{-2}$ configurations [67]. Still at N = 80, in ^{131}Sb (with one proton and two neutron holes outside ^{132}Sn), a large fraction of the members of the $\pi g_{7/2}^2 \nu\,(h_{11/2}^{-1} d_{3/2}^{-1})$ and $\pi g_{7/2}^2 \nu h_{11/2}^{-2}$ multiplets were observed combining information from β-decay and microsecond-isomer decay [68].

Moving north of ^{132}Sn, along the N = 82 shell closure, high-spin structures have been identified in the five isotones ^{136}Xe, ^{137}Cs, ^{138}Ba, ^{139}La, and ^{140}Ce, and interpreted as due to various proton excitations involving the three high-j subshells located above the Z = 50 shell closure, i.e., $\pi g_{7/2}$, $\pi d_{5/2}$, and $\pi h_{11/2}$, as well as excitations of the neutron core $h_{11/2}^{-1} f_{7/2}$ [69]. The same high-j proton orbits were found to be involved in the high-spin structures of odd-odd ^{136}Cs and ^{138}La (N = 81 isotones [70, 71]. Similarly, moving along the N = 84 shell closure, high-spin structure of the three- and five-valence proton ^{137}I and ^{139}Cs nuclei could be well described as excitations among valence particles outside the ^{132}Sn core [72].

Figure 8 summarizes partial excitation spectra of two-valence-particle/hole nuclei around ^{132}Sn, as follows from spectroscopic studies of fission fragments [36]. Such systems are especially important, since the experimental location of the members

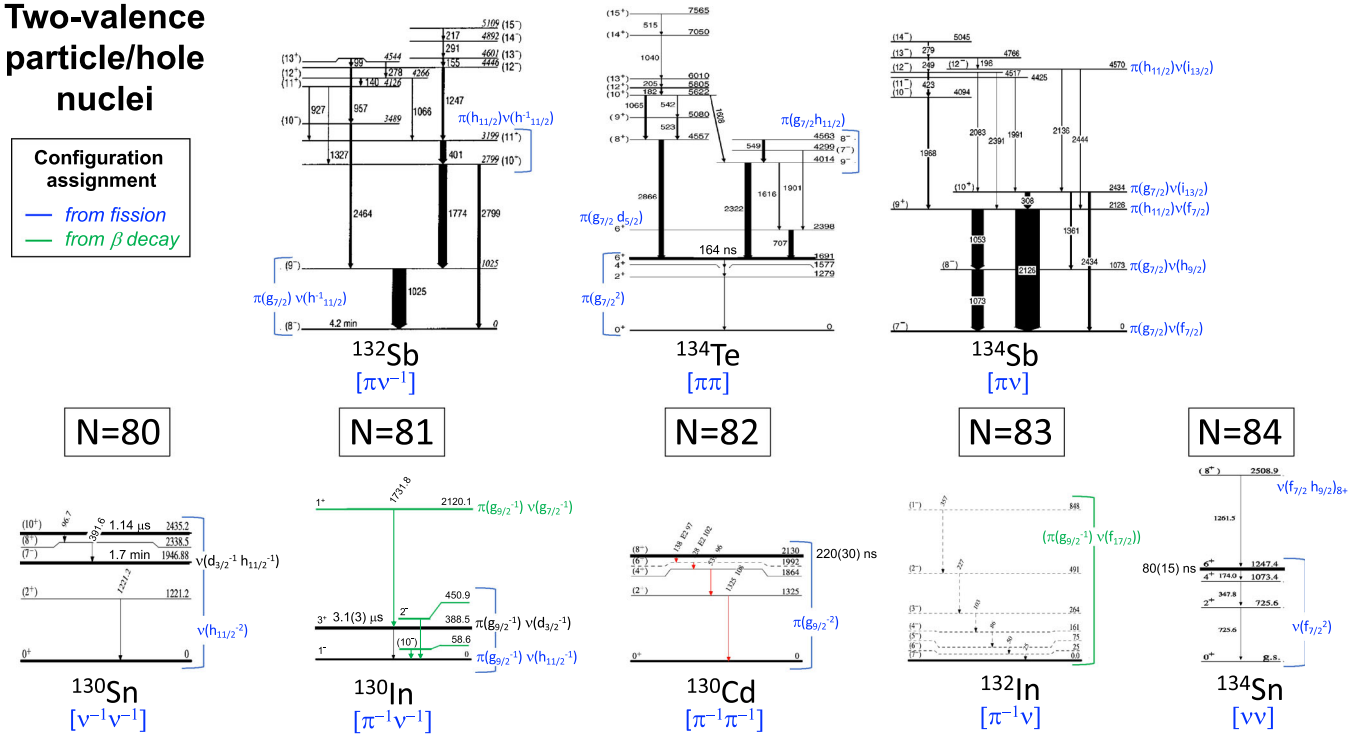

Fig. 8 Partial level schemes of two-valence particle/hole nuclei around doubly magic ^{132}Sn. Configurations are given for states which are members of multiplets formed by the two-valence particles. In blue/black (green) configurations established from fission (β-decay) studies [36, 54, 62, 65, 66, 74–79]. See Fig. 5 (**b**) for single-particle energies. (Adapted from [36] and [54, 62, 66])

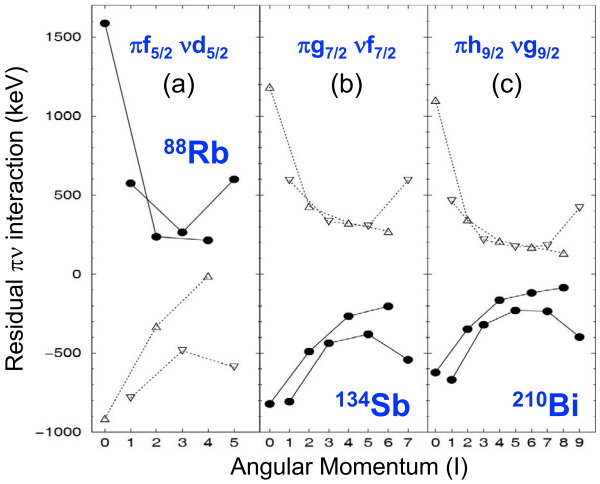

Fig. 9 Examples of empirical values of residual *pn* interactions for three particular configurations having $j_p = j_n$, with $l_p = l_n + 1$. Experimental results for ^{88}Rb, ^{134}Sb and ^{210}Bi are given by filled symbols, while open symbols refer to values obtained by applying the Pandya transformation (bringing particle-particle into particle-hole and viceversa). Similar studies are also reported in Refs. [42, 87]. See Fig. 5 for single-particle energies. (Adapted from [88])

of nucleon-nucleon multiplets allows for empirical estimates of effective two-body matrix elements of the residual nucleon-nucleon interactions, $V_{res}(I)$, for specific values of orbital angular momenta and spin orientations of the two odd nucleons (see the prescription given in Refs. [37, 73]). Examples of empirical values of $V_{res}(I)$ for the $g_{7/2}f_{7/2}$ configuration of ^{134}Sb, in comparison with values extracted from analogous configurations in ^{88}Rb and ^{210}Bi, are given in the middle panel of Fig. 9 (see discussion below). These types of empirical two-nucleon interactions have been extensively used to perform shell model calculations especially designed to give a good representation of experimental level energies in $N = 82$ isotones, from Sb to Ba, as discussed for example by Blomqvist in Ref. [44].

Odd-odd systems, around the doubly magic ^{132}Sn core, are also ideal for testing the predictive power of shell-model calculations based on realistic effective interactions, without introducing any phenomenological adjustments. This is the case, for example, of the effective interactions derived from the realistic CD-Bonn free nucleon-nucleon potential [80], using a V_{low-k} approach [81]. Such studies have been extensively performed, for example, by the Napoli group, making close comparisons between the ^{132}Sn and ^{208}Pb regions, as a consequence of the strong similarity between the two shell closures [82]. As previously pointed out in the 80's, every single-particle proton or neutron state in the ^{132}Sn region, characterized by quantum numbers $(n\ l\ j)$, has its counterpart around ^{208}Pb with quantum numbers $(n\ l + 1\ j + 1)$ (see Fig. 5b, c), therefore matrix elements of the effective interactions in ^{132}Sn and ^{208}Pb regions are expected to be proportional to one another, via a mass scaling factor $A^{1/3}$. As shown in Fig. 10a, a very satisfactory agreement is obtained in the case of the lowest lying proton-neutron multiplets of ^{134}Sb and ^{210}Bi, as well as for other corresponding systems like

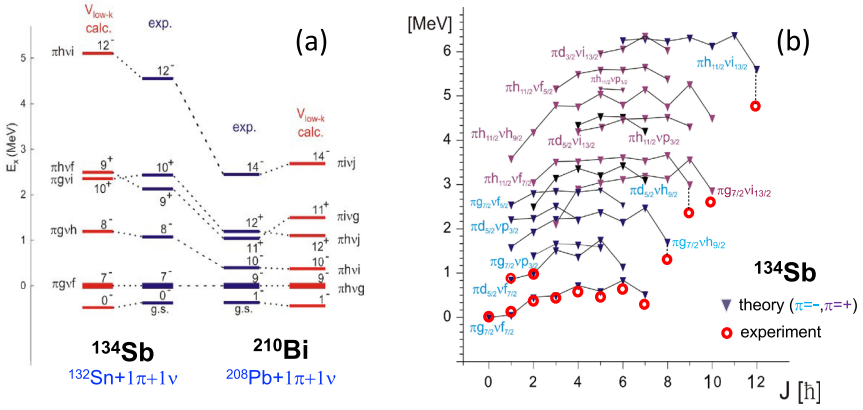

Fig. 10 Panel (**a**): Comparison of experimental two-particle yrast states in ^{210}Bi and ^{134}Sb [62], with shell-model calculations using the V_{low-k} realistic nucleon-nucleon interaction [81]. Panel (**b**): Multiplets of states in ^{134}Sb, as predicted by the same shell-model calculation below 6 MeV excitation energy. Labels refer to the proton- and neutron-single-particle orbitals involved. The experimental information (red symbols) are obtained from fission and β-decay studies: only the lowest-lying multiplet has been located, plus few highest-spin states. No information is available on lifetimes [36]. See Fig. 5**b** and **c** for single-particle energies in ^{132}Sn and ^{208}Pb

^{136}Sb and ^{212}Bi, and ^{136}I and ^{212}At, which are naturally found to be reproduced by the realistic nucleon-nucleon interactions without any empirical adjustment [82] (see Fig. 11). Such a striking result strongly supports the quality of the calculations and their predictive power for higher-lying multiplets, although larger discrepancies are expected at higher excitation energies, owing to a larger amount of configuration mixing, which is more difficult to predict starting from bare interactions (see Fig. 10b) [83]. As discussed in Ref. [84], a further test of shell-model calculations with a two-body effective interaction derived from the CD-Bonn nucleon-nucleon potential comes from g-factors measurements of valence nuclei in the vicinity of the doubly-magic ^{132}Sn core. Magnetic moments are indeed a useful probe of the single-particle structure of the orbitals outside the major shells, and g factors are particularly sensitive to the two-body interactions of the valence particles and their interactions with the core [85]. The experimental g factors of the $N = 82$ isotones of ^{134}Te, ^{135}I, and of the $N = 83$ isotones of ^{135}Te, ^{136}I, ^{137}Xe, and ^{138}Cs, from fission studies, were measured with GAMMASPHERE by placing a ^{252}Cf spontaneous fission source between two iron foils. The g-factor results for Te, Xe and Cs nuclei turned out to be well reproduced by the shell-model calculations with realistic effective interactions [84, 86]. We note that an alternative technique was pioneered with EUROBALL for g-factor measurements in mass A$\sim$100, as discussed in Sect. 7.5.

In recent years, lifetime measurements of a number of excited states in ^{134,135,136,138}Te, ^{135,137,139}I and ^{138,140,142}Xe [90–94], performed by fast-timing techniques with mixed arrays (i.e., EXILL [29] and nu-Ball [31] coupled to $LaBr_3$ detectors), provided additional information on B(E2) values, to be confronted with shell model calculations based on different interactions (see Fig. 12). The data allow to test predictions for the two- and three-valence protons isotopic chains with $N = 82$, 84 and 86 [90, 91], also

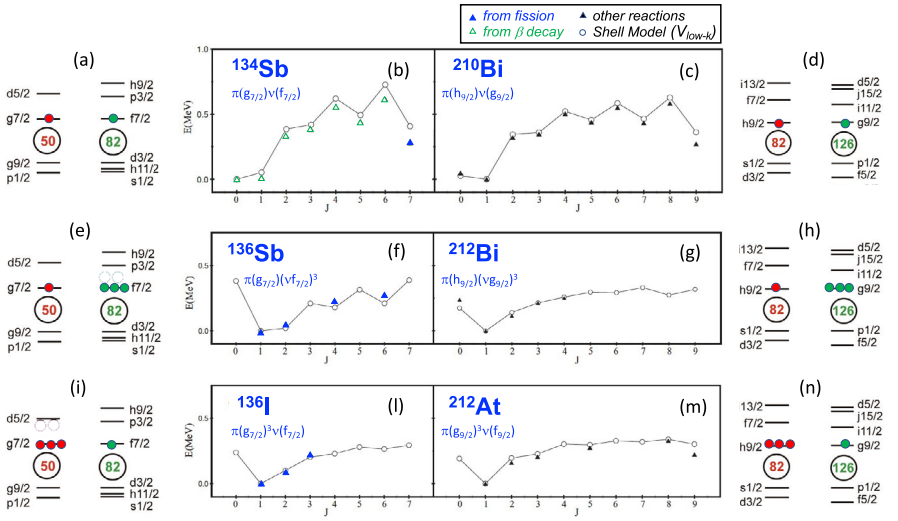

Fig. 11 Comparisons between experimental energies (triangles) and shell-model predictions (circles) for corresponding low-lying proton-neutron multiplets in ^{134}Sb (**b**) and ^{210}Bi (**c**), ^{136}Sb (**f**) and ^{212}Bi (**g**), and ^{136}I (**l**) and ^{212}At (**m**). Calculations are performed using realistic nucleon-nucleon interactions (V_{low-k}) [82]. Dominant configurations are given in the legends and illustrated by the occupation of single-particle orbitals in panels (**a**) and (**d**), (**e**) and (**h**), and (**i**) and (**n**), respectively. Experimental data for ^{134}Sb, ^{136}Sb and ^{136}I are obtained from fission (full triangles) and β-decay studies (empty triangles) [36, 47, 61, 62, 89]

in terms of the role played by the three-body component of the E2 operator, which seems to be small [92].

The predictive power of large-scale shell model calculations has also been tested on extensive data in light neutron-rich fission fragments of In, Sn and Sb isotopes, in the neighborhood of the $Z = 50$ shell closure. These calculations, performed by the codes OXBASH, NATHAN, NUSHELLX and ANTOINE, used different computational schemes and effective nucleon-nucleon interactions (see [95–97] and references therein). Such studies suggested modifications of several components of the two-body matrix elements to reach a consistent agreement with excitation energies and B(E2) transition probabilities. In particular, $^{118-128}$Sn were investigated with GAMMASPHERE employing heavy-ion-induced fusion-fission reactions with different projectile-target combinations (e.g., ^{48}Ca and ^{64}Ni beams at $\sim$ 7 MeV/u on ^{208}Pb and ^{238}U targets) [98], and with EUROBALL coupled to the fission fragment detector SAPhIR, using ^{12}C+^{238}U and ^{18}O+^{208}Pb heavy-ion reactions at $\sim$ 7 MeV/u [99]. In the same EUROBALL experiments, odd A $^{115-121}$In nuclei were also studied [100]. In more recent years, fusion- and transfer-induced fission of ^{238}U at 6.2 MeV/u have been employed to populate $^{122-131}$Sb [101], $^{118-128}$In [102, 103] and $^{130-134}$I [104] isotopes, using setups consisting of EXOGAM+VAMOS++ or AGATA coupled to VAMOS++, with EXOGAM HPGe detectors placed behind the focal plane [105].

In the case of even-A Sn isotopes, a common feature is the presence of long-lived (microseconds) 10^+ isomers with dominantly pure $(h_{11/2})^n$ neutron configurations (the so-called ν_n seniority isomers, where ν_n refers to the number of unpaired neutrons),

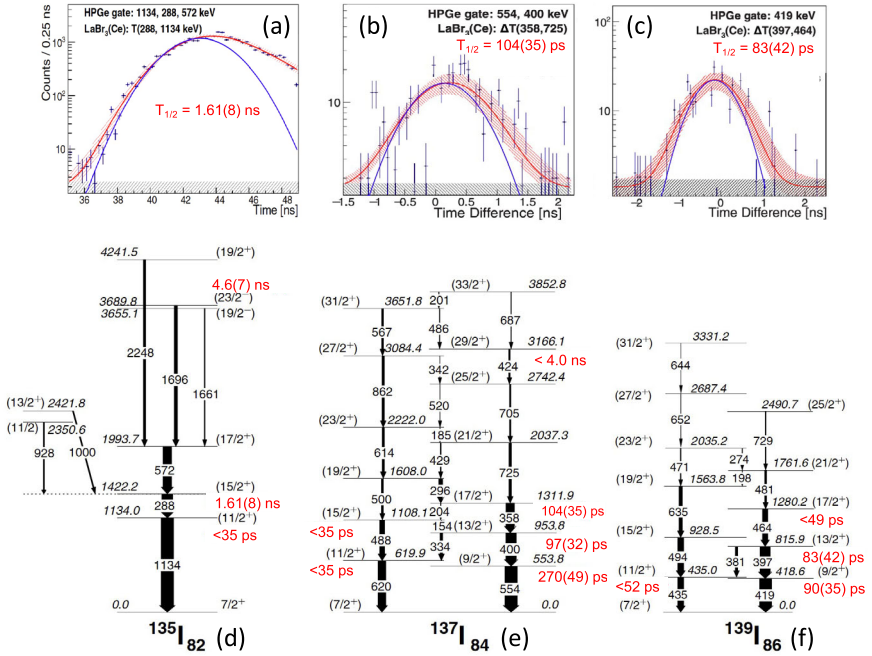

Fig. 12 Botton panels: level schemes of ^{135,137,139}I isotopes, as measured with the nu-Ball array following fast neutron-induced fission of ^{238}U. The widths of the arrows correspond to the relative γ-ray intensities. Red labels give state half-lives measured by fast-timing technique employing the 20 $LaBr_3$(Ce) detectors present in the array. Top panels: examples of time difference spectra used for the lifetime analysis of selected states, i.e., the $(15/2^+)$ state at 1422.2 keV of ^{135}I (**a**), the $(17/2^+)$ state at 1311.9 keV of ^{137}I (**b**), and the $(13/2^+)$ state at 815.9 keV of ^{139}I (**c**). (Adapted from [91])

caused by the presence of the high-j, unique parity $h_{11/2}$ orbital, which is being filled in the A =116–130 tin isotopes [106]. Such 10^+ isomers all decay by $10^+ \rightarrow 8^+ \rightarrow 7^-$ two γ-ray cascades to 7^-- isomeric states of $h_{11/2}d_{3/2}$ character, thus providing a crucial probe of the underlying neutron-neutron ($\nu\nu$) interaction. The level structure above these isomers is instead expected to give information on the involvement of the $h_{11/2}$ orbital in generating high-spin states above the isomeric states. By using prompt-delayed coincidence techniques of various types [98, 99], the level schemes of Sn isotopes have been extended to 8 MeV excitation energy (see Fig. 13a). Additional 15^- and 13^- isomeric states (with half-lives of the order of 5–250 ns) were established around 4.5 MeV in even-even Sn, and states located above 3 MeV were found to be ascribed to several broken pairs of neutrons occupying the $\nu h_{11/2}$ orbit. States having the maximum value of angular momentum of either the $(\nu h_{11/2})^n$ configurations or the $(\nu h_{11/2})^n(\nu d_{3/2})$ ones, with n = 1 to 6, were also identified in the even-A and odd-A systems. As shown in Fig. 13a, the evolution of both positive- and negative-parity states is observed to be very smooth. This indicates that their main configurations are the same, with a gradual filling of the three $\nu s_{1/2}$, $\nu h_{11/2}$, $\nu d_{3/2}$ neutron orbits, which are very close in energy for $69 < N < 81$. From the half-lives of the isomeric states, E2 transition amplitudes could also be extracted and used to determine the half-filling

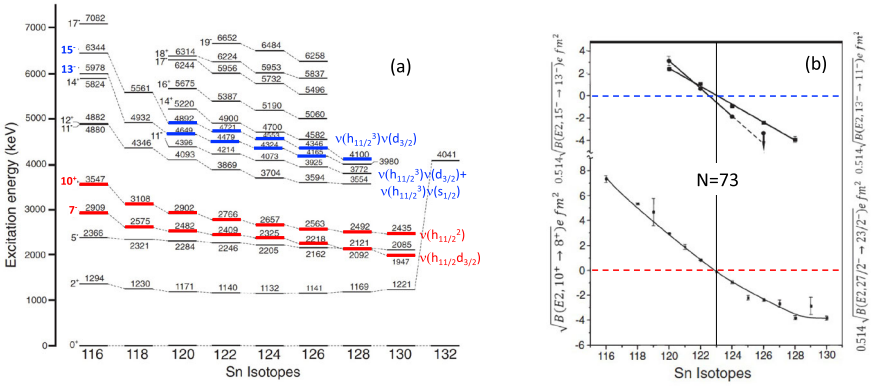

Fig. 13 Panel (**a**): Energy systematics of the yrast states observed in neutron-rich even-even Sn isotopes. Isomeric states with spin-parity assignments $J^{\pi} = 7^{-}, 10^{+}$ (in red) and $J^{\pi} = 15^{-}, 13^{-}$ (in blue) are all found to be dominated by pure neutron excitations, involving $\nu s_{1/2}$, $\nu h_{11/2}$, $\nu d_{3/2}$ neutron orbits, as indicated by labels. Panel (**b**): Transition amplitudes for the isomeric decays observed in the Sn isotopes. Upper part: E2 amplitudes for transitions associated with the 15^{-} (squares) and 13^{-} (circles) isomeric decays. Lower part: complete set of E2 transition amplitudes known for the $(h_{11/2})^{n}$ isomers in Sn isotopes. The smooth variation with Z of the B(E2) reduced transition probabilities reflects the filling of the proton $h_{11/2}$ subshell, which is found to be half-filled at $N = 73$ (i.e., ^{123}Sn) [98, 99, 106]. Experimental data from heavy-ion-induced fusion-fission reactions and GAMMASPHERE. (Adapted from [98])

of the $\nu h_{11/2}$ orbit, that happens for $A = 123$ or $N = 73$ [98, 106], when particle and hole contributions exactly cancel one another (see Fig. 13b).

As a counterpart, in odd-A Sn isotopes, microsecond yrast isomers were observed in the $^{119-129}$Sn nuclei, with spins $19/2^{+}$ and $27/2^{-}$ [25, 107, 108]. In these systems, the $27/2^{-}$ isomers (which are sub-microseconds in ^{127,129}Sn), have dominant configuration $\nu(h_{11/2})^{n}$, with seniority 3. In addition, $23/2^{+}$ and $19/2^{+}$ microsecond isomers are also observed, with dominant configuration $\nu(h^{-2}_{11/2}d^{-1}_{3/2})$, the latter being known only in ^{123}Sn and ^{129}Sn.

Similar studies performed for neutron-rich In ($Z = 49$) and Sb ($Z = 51$) isotopes showed the existence of high-spin isomeric states. The configurations are relatively pure, with the additional proton hole $(\pi g^{-1}_{9/2})$ and proton particle $(\pi g_{7/2})$ (occupying adjacent spin-orbit partners) coupled to the 7^{-} and 10^{+} isomers in even-A Sn isotopes, which tests the role of the particle-hole and hole-hole symmetry of the $\nu\pi$ interaction [101, 102]. In contrast with the smooth behavior observed for excitations above isomeric states in Sn, In and Sb isotopes, low-lying high-spin yrast states in odd-odd $^{124-128}$Sb and $^{118-128}$In nuclei show a striking difference in their observed γ-ray decay. As shown in Fig. 14a and e, for the example cases of ^{126}Sb and ^{124}In, dominant electric quadrupole (E2) transitions occur in Sb as opposed to magnetic dipole (M1) transitions in In. Such properties have been explained as a consequence of the magnetic moment of a proton in spin-orbit partner orbits, as indicated by large-scale shell-model calculations as well as schematic approaches, both pointing to the importance of the neutron-proton interaction over the like-nucleon pairing interaction in these nuclei far from stability [103].

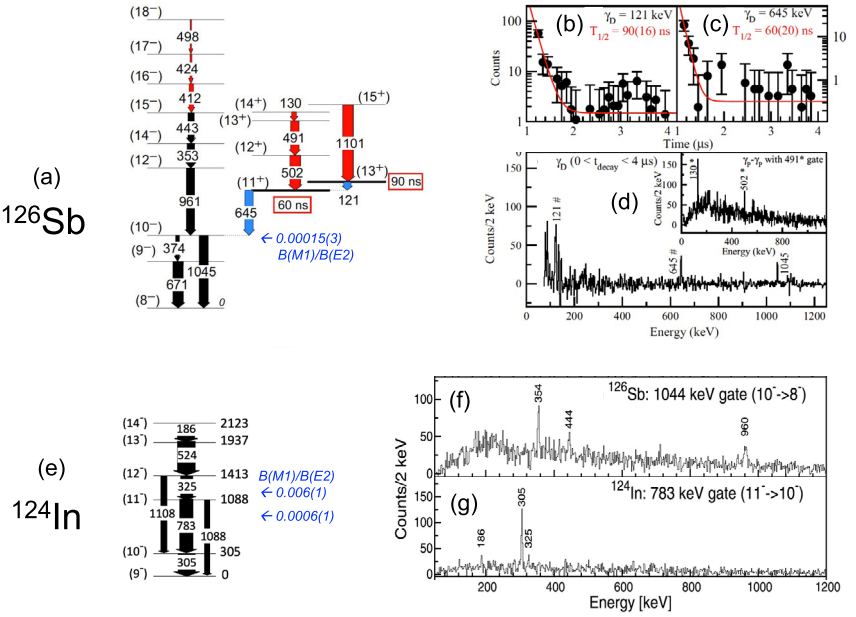

Fig. 14 Spectroscopic studies of ^{126}Sb ($Z = 51$) (**a**–**d**) and ^{124}In ($Z = 49$) (**e**–**g**), performed with the tracking array AGATA, coupled to the VAMOS++ magnetic spectrometer (with EXOGAM detectors at the focal plane) [101–103]. Panel (**a**): Level schemes of ^{126}Sb, highlighting the 11^+ and 13^+ seniority isomers, characterized by rather pure $(\pi g_{7/2} \nu h_{11/2}^{-2} d_{3/2}^{-1})$ configurations. Red (blue) arrows indicate transitions populating (depopulating) the isomers. Panels (**b**) and (**c**): decay curves of the 11^+ and 13^+ isomers of ^{126}Sb, based on the analysis of the 121- and 645-keV depopulating transitions. Panel (**d**): γ-ray spectra probing the coincidence relationships among prompt and delayed γ rays. Panel (**e**): Level schemes of ^{124}In, constructed from the analysis of gated γ-ray spectra of the type displayed in panels (**f**) and (**g**). B(M1)/B(E2) ratios of low-lying states in ^{126}Sb and ^{124}In are given by blue labels, highlighting the dominance of electric quadrupole (E2) transitions in Sb as opposed to magnetic dipole (M1) transitions in In. The difference is attributed to the properties of the p-n interaction [103]. (Adapted from [101, 103])

Prompt-delayed γ-ray spectroscopy, with very selective setups such as AGATA+ VAMOS++ with EXOGAM detectors at the focal plane, have also been instrumental to locate excited states in neutron-rich $^{130-134}$I, above high-spin isomers (8^- and $19/2^-$ in even and odd systems, respectively) [104]. In particular, comparisons with large-scale shell model calculations show that the structure of the excited negative-parity states is dominated by the three proton particles, outside $Z = 50$, in the $\pi g_{7/2}$, $\pi d_{5/2}$ and $\pi h_{11/2}$ orbitals, and by the three neutron holes in the $\nu d_{3/2}$, $\nu s_{1/2}$, $\nu h_{11/2}$, while all other orbitals remain relatively inactive (cfr. Fig. 5b). Moreover, for all high-spin states the main contributions come from the hole occupancy in the $\nu h_{11/2}$ orbital. The configuration is almost a pure neutron hole in ^{133}I, while it varies significantly in the other I isotopes, in favor of two or three neutron holes in $\nu h_{11/2}$.

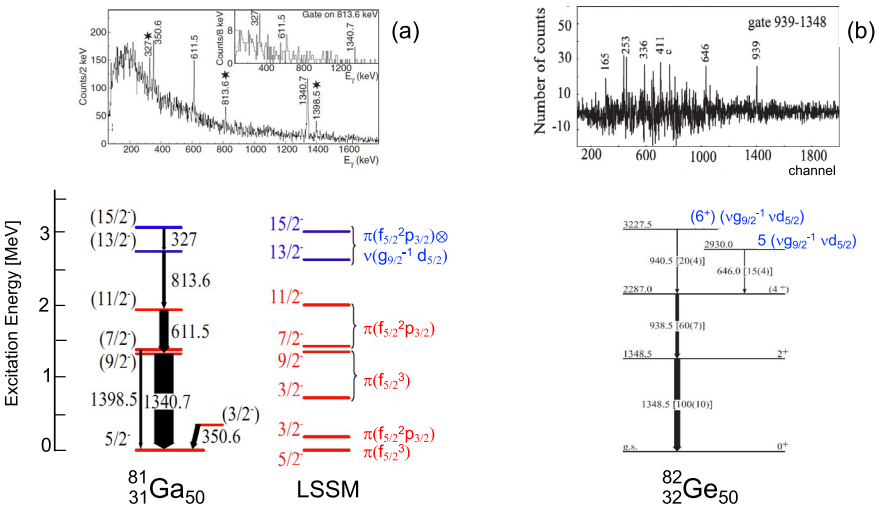

Fig. 15 Level schemes of the $N = 50$ isotones ^{81}Ga (left) and ^{82}Ge (right), constructed exploiting the coincidence relationships deduced from gated γ-ray spectra of the type shown in the corresponding top panels. In ^{81}Ga, the needed sensitivity is reached by gating on the fission fragment mass detected in VAMOS++ (AGATA data) [109], while multiple γ-ray gates are used in the case of ^{82}Ge (EUROGAM-2 data) [110]. In both cases, state configurations are assigned on basis of comparisons with large scale shell model calculations. The (15/2$^-$) and (13/2$^-$) states in ^{81}Ga, and the (6$^+$) and (5) states in ^{82}Ge are found do be dominated by neutron-core excitations involving the $g_{9/2}$ and $d_{5/2}$ orbits (see Fig. 5**a**), therefore their energies can be used to assess the size of the $N = 50$ shell gap (see also Fig. 16)

2.1.2 The $N = 50$ shell closure

In this section, we will discuss selected examples of fission-fragments studies in the vicinity of the $N = 50$ gap, which have greatly contributed to establishing the size of the shell gap, as well as the residual interaction energies for various proton-neutron configurations. As shown in Fig. 5a, in the case of $N = 50$, the size of the gap is determined by the energy of the $g_{9/2}$ and $d_{5/2}$ orbits, and corresponding *1p-1h* states will have a $(g_{9/2})^{-1}(d_{5/2})^{+1}$ configuration. This gives rise to a multiplet of six states with spin values J between 2 and 7.

In general, a complete identification of all members of such *1p-1h* multiplets is experimentally very challenging, in particular when moving away from the valley of stability. As pointed out in the discussion of the $Z = 50$ and $N = 82$ shell closures (see Sect. 2.1.1), the fission production mechanism has been one of the most valuable tools to populate the highest spin states of valence-particle/hole multiplets, if located near the yrast line. In the case of the $N = 50$ gap, extensive studies performed with the EUROBALL array, using both spontaneous fission and fusion-fission reactions, allowed identification of medium-spin states in $N = 50$ isotones above ^{78}Ni (e.g., in ^{86}Kr [111], ^{84}Se [111], and ^{82}Ge [110, 112]), assigned to neutron-core excitations involving the $g_{9/2}$ and $d_{5/2}$ orbits (Fig. 15b). Neutron excitation across the $N = 50$ gap were also found in the odd systems ^{83}As [113], and ^{81}Ga with AGATA+VAMOS [109] (Fig. 15a), as well as in ($Z = 49$) ^{83}Se and ^{85}Se, in earlier studies with EUROBALL

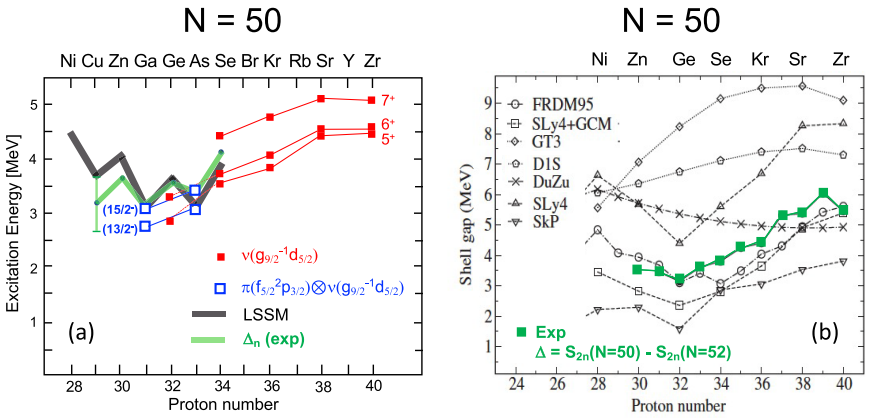

Fig. 16 Panel (**a**): evolution, along the $N = 50$ shell closure, of the low-lying (5^+), (6^+) and (7^+) excited states from Zr to Ge (full squares), and of the $(13/2^-)$ and $(15/2^-)$ low-lying states in ^{81}Ga and ^{83}As (open squares). All states are dominated by neutron-core excitations from the $g_{9/2}$ to the $d_{5/2}$ orbit (see Fig. 5a), therefore their energies can be used to assess the size of the $N = 50$ shell gap. The green line gives, for comparison, the amplitude of the shell gap Δ_n, calculated from the binding energies BE(Z,N) using the expression Δ_n = BE(Z, 51) + BE(Z, 49) - 2 × BE(Z, 50), which includes correlations present in the ground state. Large scale shell model (LSSM) predictions are given by the black line [109, 110]. Panel (**b**): the amplitude of the $N = 50$ shell gap Δ (solid squares), obtained experimentally from the two-neutron separation energies $\Delta = S_{2n}(N=50) - S_{2n}(N=52)$, in comparison with different model predictions. (Adapted from [116])

[114] (an extended low-spin study of ^{85}Se was reported by Kurpeta et al. [115]). Such spectroscopic observations suggested a possible weakening of the $N = 50$ shell closure, moving towards ^{78}Ni, as shown in Fig. 16a. Two-neutron separation energy measurements provided further evidence for the reduction of the $N = 50$ shell gap energy towards germanium (Z =32), followed by a subsequent increase around gallium ($Z = 31$), what confirms the persistent rigidity of the shell gap towards nickel ($Z = 28$) [116–118] (Fig. 16b).

Accurate predictions of the evolution of the shell gaps and of single particle levels at very large neutron excess need the knowledge of the energies of the residual interactions for the different nucleon-nucleon configurations [37]. In the case of the N = 50 spherical shell gap, residual interaction energies for various proton-neutron configurations, associated with protons in fp ($28 < Z < 38$) and neutrons in dg ($N \sim 50$) orbitals, have been obtained from high-spin states observed in odd-odd ($N = 51$) ^{88}Rb and ^{86}Br nuclei [88], as shown in Fig. 17 for ^{88}Rb. Such states were interpreted in terms of configurations involving proton excitations from three sub-shells located close to the Fermi levels, $\pi\, p_{3/2}$, $\pi\, f_{5/2}$, and $\pi\, g_{9/2}$, the neutron in the $\nu d_{5/2}$ orbital acting as a spectator (see Fig. 5). In ^{88}Rb, empirical values of residual proton-neutron interactions from the multiplets of states resulting from the $\pi\, p_{3/2}\nu d_{5/2}$ and $\pi\, f_{5/2}\nu d_{5/2}$ configurations could be extracted and compared with similar configurations having $j_p = j_n$ with $l_p = l_n + 1$ in the mass regions of ^{132}Sn (i.e., $\pi\, g_{7/2}\nu\, f_{7/2}$) and ^{208}Pb (i.e., $\pi h_{9/2}\nu g_{9/2}$) [88], allowing for stringent tests of shell model approaches. As shown in Fig. 9, after applying the so-called Pandya transformation [119], interactions extracted

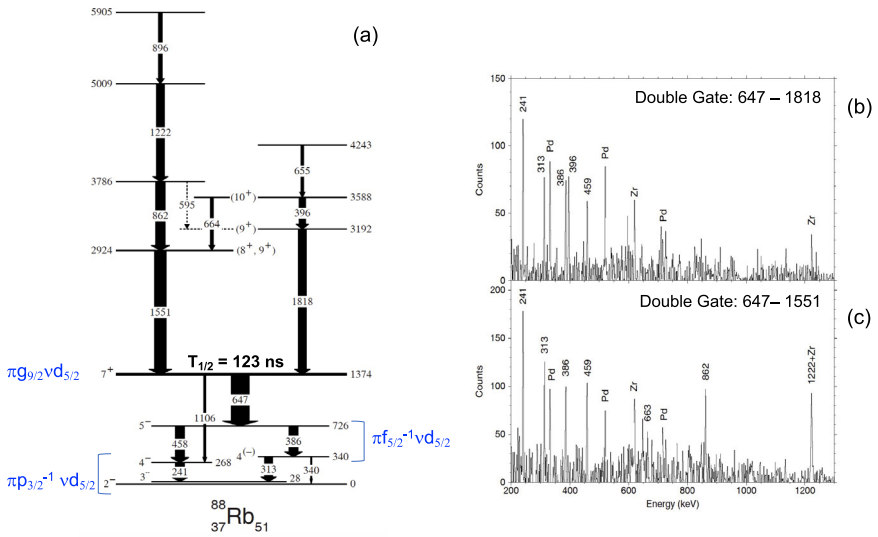

Fig. 17 Level schemes of ^{88}Rb ($N = 51$) (panel (**a**)), constructed from coincidence γ-ray spectra measured with EUROBALL (examples in panels **(b)** and **(c)**), following the fusion-fission reaction ^{18}O+^{208}Pb, at 85 MeV bombarding energy. Low-lying states, grouped in multiplets, are labeled by the dominant configuration involving $\pi\, p_{3/2}$, $\pi\, f_{5/2}$, and $\pi\, g_{9/2}$ proton orbitals and the $\nu d_{5/2}$ neutron, acting as a spectator. From the excitation energies of the multiplets, values of residual proton–neutron interactions have been extracted (see also Figs. 5 and 9). (Adapted from [88])

from (particle-particle) and (particle-hole) excitations could be directly compared in the three mass regions. Strong similarities of values for the empirical interactions were obtained, what suggests an underlying universal character of the nucleon-nucleon force. The important role played by the tensor force in the $\pi\, f_{5/2}\nu d_{5/2}$ configuration was also highlighted.

High-spin studies in ^{84,85}Br [120] with EUROBALL and, more recently, in ^{87,88}Br and ^{90}Rb nuclei [42, 121, 122], at EXILL, led to the location of few-particle configurations also involving proton excitations from the $f_{5/2}$, $p_{3/2}$ and $g_{9/2}$ orbitals, above the Z = 28 shell closure. Members of the $\pi\, p_{3/2}\nu(d_{5/2})^3$, $\pi^{-1}_{3/2}\nu\ (d_{5/2})^3$ and $\pi\, f^{-1}_{5/2}\nu\ (d_{5/2})^3$ multiplets were identified, as well as a triplet of yrast states (5^+, 6^+ and 7^+), in ^{88}Br and ^{90}Rb, arising by coupling the $g_{9/2}$ proton to the $(\nu d_{5/2})^3$, seniority-3 multiplet, as shown in Fig. 18 for ^{88}Br. A first level scheme of the neutron-rich ^{88}Se was also established with the EXILL setup [123], giving indication for an onset of quadrupole deformation. Such detailed and systematic investigations have provided important inputs for large shell model calculations, as for example the position of the $g_{9/2}$ proton intruder in the ^{78}Ni core, at 5.7 MeV above the $f_{5/2}$ proton level (cfr., Fig. 5), which is also supported by the spectroscopic studies of ^{83}As [113]. In addition, they have significantly contributed to improve effective interactions especially designed for the ^{78}Ni region, in particular for what concerns the proton-proton matrix elements (e.g., the $\pi\, f_{5/2} - \pi\, p_{3/2}$ single-particle energy splitting was reduced) [123]. Further support to the shell model calculations also comes from recent extended inves-

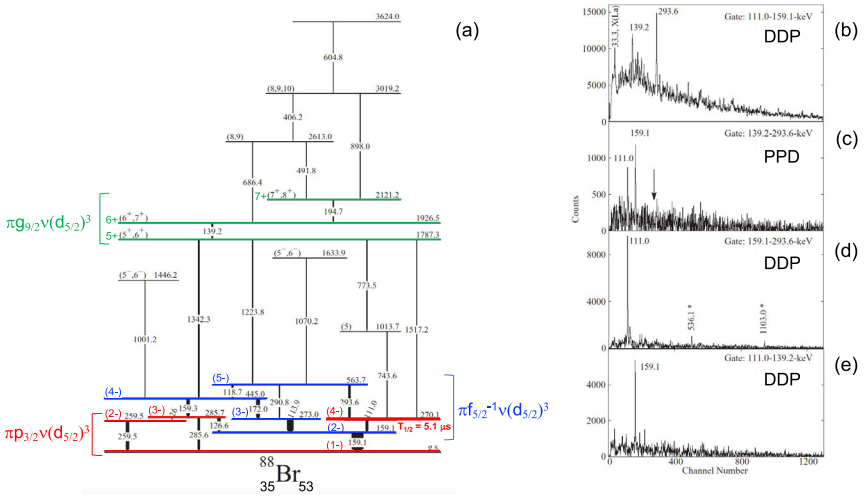

Fig. 18 Level schemes of ^{88}Br ($N = 53$) (panel (**a**)), as obtained from γ-ray spectra measured with EXILL in triggerless mode, which allowed construction of three-dimensional histograms with various conditions on coincidence times. Examples of gated spectra are shown in panels **(b)**-**(e)**, where (P) and (D) refer to "prompt" and "delayed" γ-rays, namely transitions registered within the 0–300 ns and 400 to 2400 ns time windows (with respect to the "0" time arrival of the first prompt γ ray), respectively. The analysis considerably expanded the ^{88}Br level scheme above the (4^-) long-lived isomeric state located at 270.1 keV and allowed to identify multiplets of states involving $\pi\, p_{3/2}$, $\pi\, f_{5/2}$, and $\pi\, g_{9/2}$ proton and $\nu d_{5/2}$ neutron orbitals (as labelled in the figure), from which values of residual proton-neutron interactions could be extracted. The spin of the ground state was also assigned to (1^-), changing the adopted (2^-) value. (Adapted from [42])

tigations of low-spin states of nuclear systems in the same region (e.g., ^{86}Br and ^{86}Kr, following β-decay and neutron-induced fission of ^{235}U [124]).

2.2 Couplings with core excitations around the ^{132}Sn shell closure

One-valence particle/hole nuclei around doubly magic shell closures are primary sources of information for effective single-particle orbitals (as discussed in Sect. 2.1), as well as more complex states involving excitations of the core. In this respect, the region around ^{132}Sn is ideal to simultaneously test the coupling of valence particles with core excitations of various natures. For example, in Fig. 7, ^{132}Sn shows 2^+, 3^- and 4^+ excitations below 5.3 MeV of collective nature (named "phonons"), plus other states of *1p-1h* character [36, 54]. It follows that one-valence particle/hole nuclei such as ^{131}Sn, ^{133}Sb and ^{131}In, (being bound up to 5.2, 7.4 and 6.2 MeV, respectively and unlike ^{133}Sn with a neutron binding energy of only 2.4 MeV), are perfect cases for the investigation of particle/hole-core-coupled excitations, provided they can be populated with sufficient intensities. As shown in Fig. 6, spectroscopic studies based on spontaneous and neutron induced fission of actinides [36, 55–57, 59, 68], as well as relativistic fission of a ^{238}U beam [58], have permitted the identification of members of multiplets involving the odd particle/hole (e.g., the $g_{7/2}$ proton, and the $h^{-1}_{11/2}$ neu-

tron and $g_{9/2}^{-1}$ proton) coupled to the 2^+, 3^- and 4^+ phonons and the less collective $\nu(f_{7/2}h_{11/2}^{-1})$ excitation of the ^{132}Sn core.

While states involving *1p-1h* core excitations can be well accounted for by large scale shell model calculations [59], more collective (phonon-type) core excitations require alternative approaches [125–127]. In such a heavy-mass region, phonons cannot be fully treated by the shell model, as it would require full calculations in a configuration space that encompasses proton and neutron orbitals below and above ^{132}Sn. For this purpose, a new microscopic and self-consistent model (named "Hybrid Configuration Mixing" (HCM)) has been developed, with the aim of describing states with different degrees of collectivity [55, 128, 129]. The HCM model has no free parameters and is self-consistent in the sense that both single-particle states and phonons come out of Hartree-Fock (HF) and Random Phase Approximation (RPA) calculations performed with the Skyrme SkX interaction [130]. In the case of ^{133}Sb and ^{131}Sn [55, 131], the model is found to reproduce well the energy sequence of the high-spin states observed experimentally, pointing to a fast evolution of the wave function composition, from collective to non-collective character, with increasing spin. In the case of ^{133}Sb, as indicated by the configurations reported in Fig. 6, the low spin states are interpreted as dominated by the $g_{7/2}$ proton coupled to the 2^+ phonon, while the highest spin excitations arise mostly from this valence proton coupled to the neutron $h_{11/2}^{-1}f_{7/2}$ non-collective core excitation. The intermediate states, at spin $13/2^+$ and $15/2^+$, show instead a fragmented wave function involving the coupling of the valence proton to both the 4^+ phonon and $h_{11/2}^{-1}f_{7/2}$ non-collective particle-hole excitations.

2.3 Evolution of nuclear shapes and shape-coexistence phenomena

Shape is one of the most intriguing properties of the atomic nucleus. While spherical shapes naturally appear in the vicinity of double shell closures, different nuclear shapes emerge in regions lying away from doubly magic nuclei. Quadrupole symmetric forms are usually dominant, although they often compete and may even coexist with spherical ones in the same nucleus, at low excitation energy [38, 132]. The evolution of the atomic nuclear shape along isotopic chains and the occurrence of shape-coexistence phenomena are a clear manifestation of the subtle interplay between macroscopic (collective) and microscopic (individual nucleons) effects, which are nowadays recognized to occur all over the nuclear chart, from rather light through to the heaviest systems (e.g., [133–138]).

In this context, the most striking change of deformation along isotopic chains is observed in neutron-rich nuclei of Rb, Sr, Y and Zr in the A$\sim$ 100 region. Such nuclei are also astrophysically relevant, since they lay in the proximity of the r-process nucleosynthesis path (see Sect. 3). The lower and upper boundaries of this mass region are represented by the Kr (Z = 36) and Mo (Z = 42) isotopic chains, for which the transition between different deformations is smoother, with possible sign of triaxialities, in particular for heavier Z (see Fig. 4). Already in the '70 s, γ spectroscopy of fission fragments of ^{252}Cf revealed a region of stable deformation, beyond neutron number N = 60, in sharp contrast with dominant spherical shapes for nuclei with only one, two neutrons less. This was in agreement with mean-field predictions by Ragnarsson

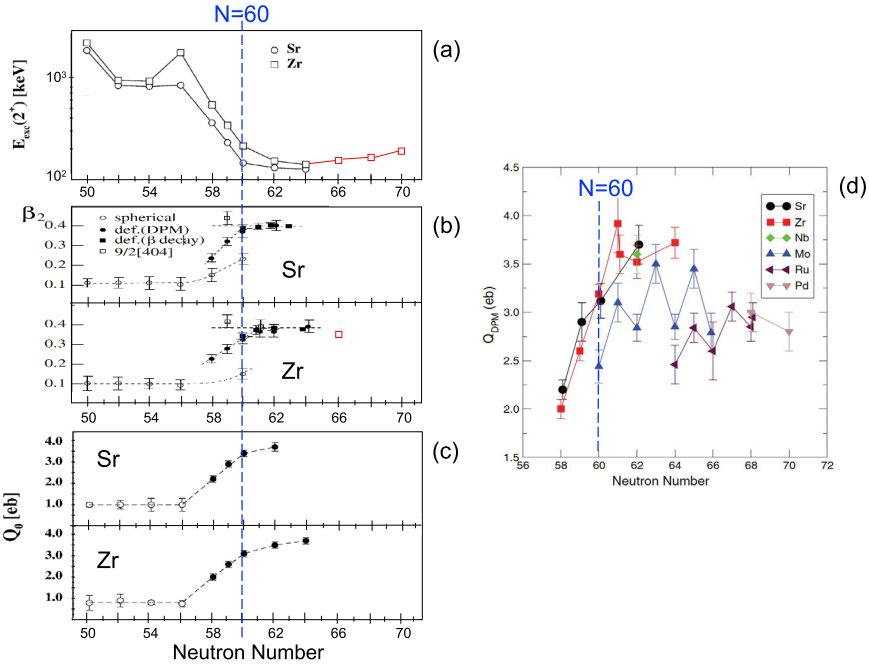

Fig. 19 Spectroscopic information for neutron-rich Sr and Zr isotopes, as obtained from γ-spectroscopy studies of fission fragments produce by spontaneous fission of ^{248}Cm (N = 50–64, EUROGAM-2 data) [141] and fission of ^{238}U in inverse kinematics (N = 66–70, EXOGAM+VAMOS and RIKEN data, the latter in red) [36, 79, 146]. Panel (**a**): energy of the first 2^+ state. Panel (**b**): β_2 deformation for various configurations, with dashed lines to guide the eye. Panel (**c**): intrinsic quadrupole moment Q_0 for various configurations of Sr and Zr (empty circles for spherical/weakly deformed, full symbols for deformed). All quantities point to a shape transition (from spherical to deformed) occurring around N = 60, as also supported by the trend of the B(E2; $2^+ \rightarrow 0^+$) values, obtained from lifetime measurements [144] (see also Fig. 23c). Panel (**d**): Transition quadrupole moments deduced from the lineshape analysis of γ decays from states at spin $\sim 10\hbar$ for nuclei in the A$\sim$100 mass region. (Adapted from [23, 141, 142])

and Nilsson [139] and by Arseniev, Sobiczewski and Soloviev [140]. More recently, extended investigations of fission fragments in this mass region, produced with various mechanisms (see Table 1 in Sect. 7), have consolidated this picture. For example, Fig. 19 shows that moving along the Sr and Zr isotopic chains reveals a drop in the first 2^+ state energy, accompanied by an increase of the β_2 deformation parameter and quadrupole moment values, clearly demonstrating that nuclei with N>60 are strongly deformed rigid rotors [141, 142]. Such a picture is also supported by the trend of the corresponding B(E2; $2^+ \rightarrow 0^+$) values, as measured with various approaches, including fast-timing techniques within the EXILL campaign [143, 144] (see also Fig. 23 and related discussion). Moreover, the analysis of Doppler-broadened lineshapes corresponding to transitions from excited rotational states in Sr, Zr, Mo, Ru, and Pd fission fragments, beyond N = 60, confirmed the persistence of deformation at nuclear spins $\sim 10\hbar$ [23, 145] (see Fig. 19 in Sect. 7.4.2.2).

Further detailed γ-spectroscopy studies of fission fragments, also based on isomer- and β-decay spectroscopy (often complemented by neutron capture investigations) have shown a complex scenario of nuclear excitations, pointing to the coexistence of spherical, oblate and prolate shapes in nuclei such as ^{96,97}Rb [153, 154], ^{96,97,98}Sr [143, 154–157], $^{96-98}$Y, $^{98-100}$Zr [158, 159]. In these nuclei, the excited spherical or deformed structures are most often built on long-lived (e.g., ∼1–10's μs) isomeric states (see also Refs. [24, 25] and Sect. 2.6). Lighter systems in this region are instead mainly of spherical nature [160], often displaying shorter living isomers (e.g., ∼10–100's ns), as for example in $^{91-95}$Rb nuclei [161–163], studied at ILL in ^{235}U neutron-induced fission experiment with the FiFi spectrometer [164].) Contrary to heavier isotopes, the isomeric nature of these states is caused by the presence of high-j, single-particle orbitals (e.g., $\pi(g_{9/2})$, $\nu(g_{7/2})$, and $\nu(h_{11/2})$), which makes them useful probes of single-particle energies in this region (see also Sect. 2.6).

As shown in Figs. 20 and 21, the yttrium (Z = 39) and zirconium (Z = 40) isotopic chains offer a perfect example of such a shape evolution and coexistence phenomena across neutron number N = 60: while the ground state of ^{96}Y and ^{97}Zr (N = 57) are considered almost spherical, ^{99,100}Y and ^{100,101}Zr have a strongly deformed ground state [36, 142, 147, 150, 151]. In yttrium nuclei, deformed structures are found to appear at high excitation energy already in ^{96}Y (N = 57) [147, 148], and ^{98}Y becomes and extraordinary example of shape coexistence, with a spherical ground state and two low-lying isomeric states (i.e., below 500 keV), with prolate deformation [149]. A similar scenario of shape coexistence is also observed in ^{99}Zr [141], while systematic investigation of heavier ^{104,105,106}Zr isotopes, performed with EXOGAM+VAMOS in GANIL, point to a rather smooth structure change characterized by collective (prolate) excitations with some degree of triaxiality [146].

In contrast to the sharp onset of quadrupole deformation observed in Sr (Z = 38) and Zr (Z = 40) isotopes, when going from neutron number N = 58 to N = 60, a much smoother development of collectivity has been reported along the krypton (Z = 36) isotopic chain, beyond N = 50. This follows from a complete systematic investigation of B(E2; $2_1^+ \rightarrow 0_1^+$) transition probabilities, obtained from Coulomb excitation experiments using the MINIBALL γ-ray array at the REX-ISOLDE facility [166, 167] and, in the case of ^{90}Kr, via electronic γ-γ timing (fast-timing) technique performed during the neutron-induced fission EXILL campaign, with the FATIMA spectrometer [168]. Isomers are reported in ^{94,95}Kr only [165, 169]. While the 195.5-keV, ($7/2^+$) isomer of ^{95}Kr is very-long lived ($T_{1/2}$=1.4(2) μs) and possibly of spherical nature (as follows from studies at the LOHENGRIN mass spectrometer [169]), a (9^-) short-lived isomer, with a half-life of 32(3) ns, has been located at 3.4 MeV excitation energy in ^{94}Kr, using the nu-Ball hybrid spectrometer and fast-neutron-induced fission of ^{238}U. The ^{94}Kr isomer has a two-quasineutron structure with dominant configuration $\nu(h_{11/2}g_{7/2})$ and oblate deformation β = -0,22 [165], very similar to that of the neighboring isotones ^{92}Se and ^{96}Sr, observed in relativistic fission of ^{238}U and spontaneous fission of ^{248}Cm, respectively (see Fig. 22) [170, 171]. Such data allow testing the single-particle energies in the region of ^{78}Ni, in particular for what concerns the position of the $\nu h_{11/2}$ orbital, which is not fully established, experimentally.

According to very recent high-sensitivity measurements of neutron induced fission at EXILL [174] and of fusion-induced fission performed with the AGATA track-

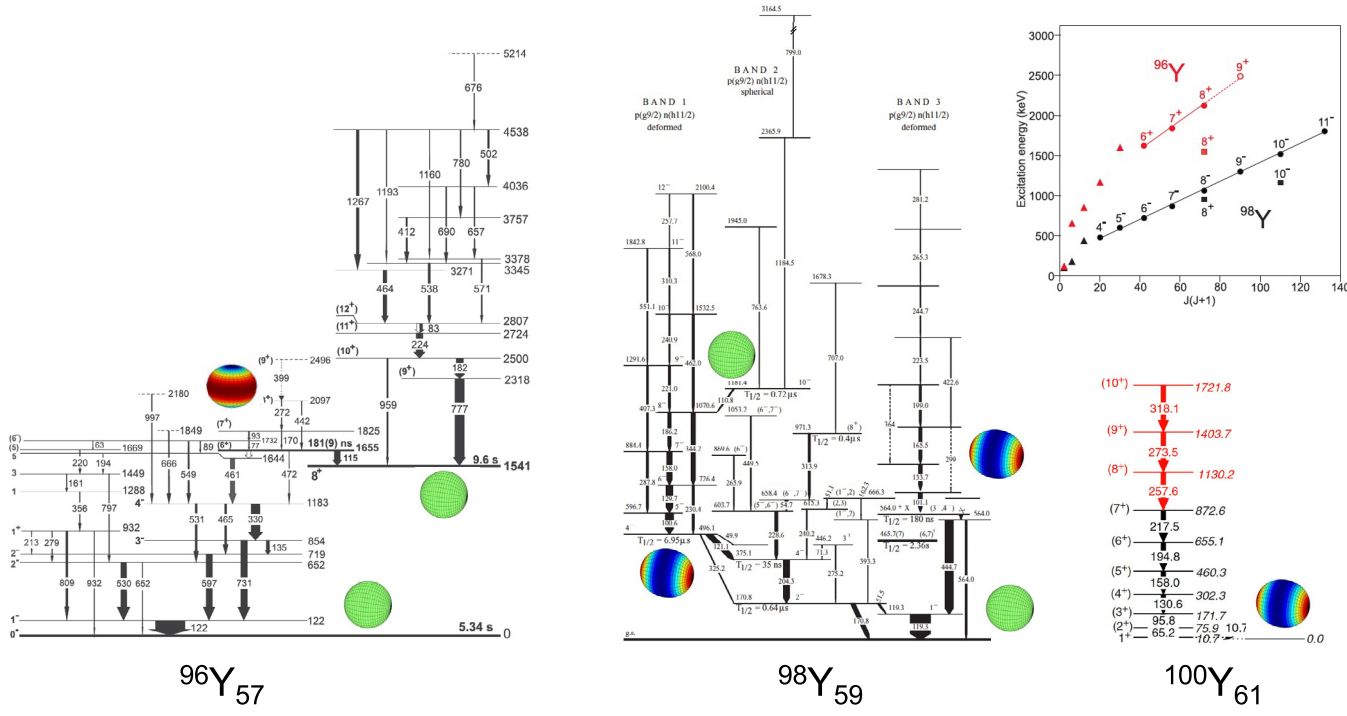

Fig. 20 Partial level schemes of ^{96}Y (left), ^{98}Y (center) and ^{100}Y (right). An evolution from spherical to deformed shapes is observed, with coexistence of both types of structures in ^{96}Y and ^{98}Y, as indicated by cartoons. In ^{96}Y, the short band built on the 181 ns isomer is interpreted as oblate deformed. Inset: dependence of the excitation energies on $J(J+1)$ for the short oblate band in ^{96}Y and the prolate band in ^{98}Y, built on the 4.1 μs isomer, what shows the typical pattern of rotational bands. The level schemes have been constructed from γ-spectroscopy studies of fission fragments populated in neutron induced fission of ^{235}U (^{96}Y, FIPPS data [147, 148]; ^{98}Y, data from EXILL and LOHENGRIN combined with GAMMASPHERE data [149]) and from ^{238}U fission in inverse kinematics (^{100}Y, EXOGAM+VAMOS data [150]). (Adapted from [147, 149, 150])

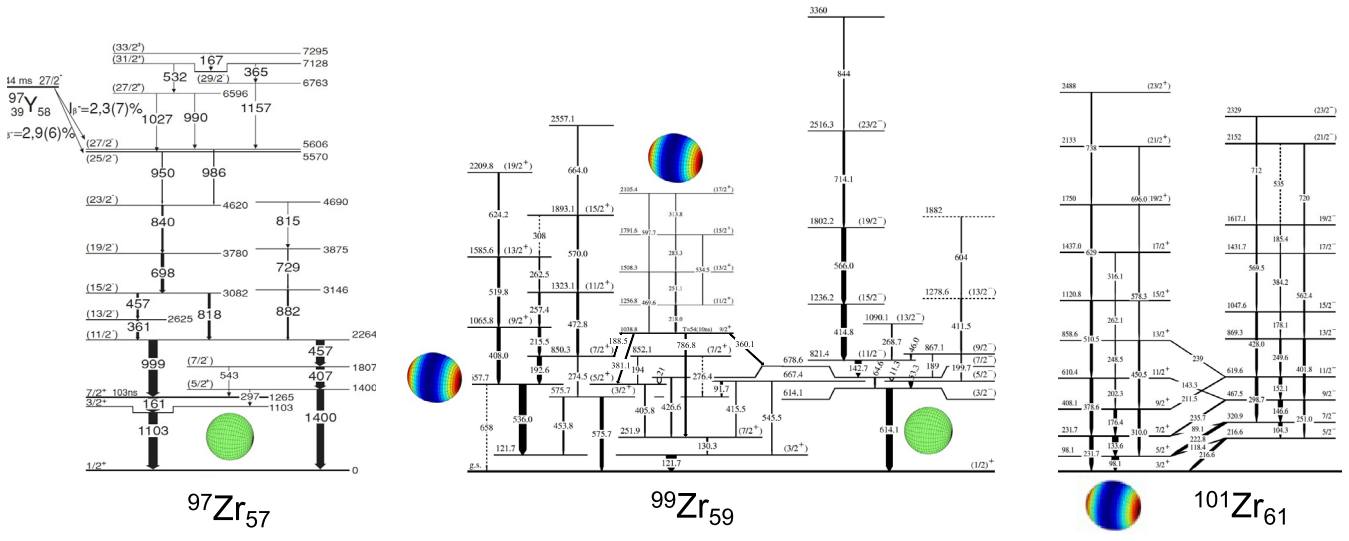

Fig. 21 Partial level schemes of ^{97}Zr (left), ^{99}Zr (center) and ^{101}Zr (right). A clear evolution from spherical to deformed shapes is observed, with coexistence of both types of structures in ^{99}Zr (N = 59), as indicated by cartoons. The level schemes were obtained from γ-spectroscopy studies of fission fragments populated in the ^{48}Ca+^{238}U reaction (^{97}Zr, GAMMASPHERE data) [151] and spontaneous fission of ^{248}Cm (^{99,101}Zr, EUROGAM-2 data) [141, 142, 152].(Adapted from [141, 142, 151, 152])

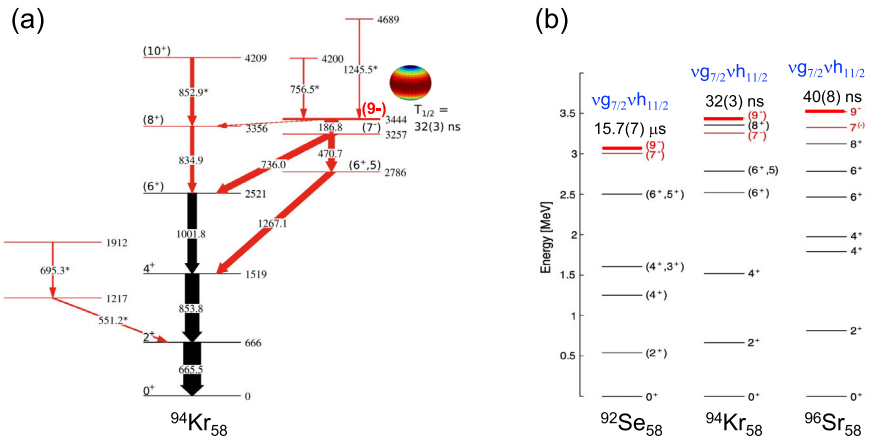

Fig. 22 Panel **(a)**: Level schemes of ^{94}Kr, obtained from the analysis of multi-fold γ coincidences measured with the nu-Ball array, following fast-neutron induced fission of ^{238}U [165]. Newly observed states and transitions are marked in red, including the (9^-), 32(3) ns isomer, located at 3444 keV and interpreted as an oblate deformed state. Panel **(b)**: Excitation spectra of the $N = 58$ isotones ^{92}Se, ^{94}Kr and ^{96}Sr, all characterized by long-lived (9^-) isomers located around 3.5 MeV, with dominant component $\nu g_{7/2}\, \nu h_{11/2}$ and oblate character. (Adapted from [165])

ing array and the VAMOS spectrometer, the Kr isotopic chain represents the low-Z boundary of the island of deformation for $N = 60$ isotones. The ^{96}Kr does not show a well-developed collectivity as found in heavier isotones (see Fig. 23) [172]. Hints of shape transition phenomena have been found beyond $N = 50$, as low in mass as the hard-to-reach ^{84}Ge nucleus [175] and with traces of a possible onset of γ collectivity in ^{86}Se ($N = 52$) [176].

From the discussion above the high relevance of experimental studies of neutron-rich A$\sim$100 nuclei for testing mechanisms producing nuclear deformation becomes clear. As previously mentioned, mean-field-based calculations first attributed strong shape variations in this region to shell effects associated with large spherical and deformed subshell closures in the single-particle spectrum. In particular, the strongest shell effects were expected for subshell closures at $N = 56$ and $Z = 40$, as shown for example by the Nilsson diagrams on Fig. 24a and b. According to various calculations, the occupation of $h_{11/2}$ neutron and $g_{9/2}$ proton orbitals is essential for understanding the appearance of deformed configurations occurring near $N = 58$, although the details of the shape transition are predicted differently by various models, since the onset and rapidity of the transition is very sensitive to the ingredients of the specific theory approach [132, 179–181]. Panel (c) of Fig. 24 shows an example of early predictions for Sr, Zr and Kr isotopes obtained in the 90's by Skalski and Nasarewicz [178] with the Nilsson-Strutinsky method with the cranked Woods-Saxon average potential and a monopole pairing residual interaction. Two minima, corresponding to prolate and oblate shapes, were found to appear in the nuclear Potential Energy curves, separated by a relatively high barrier. The largest prolate deformations were predicted at the middle of the shell, i.e., around $Z = 38$, 40, and $N = 60$, 62, and 64, associated to the large prolate gaps in the single-particle diagram. While Sr and Zr isotopes were predicted to be axially deformed, Mo-Pd isotopes were calculated to be soft with

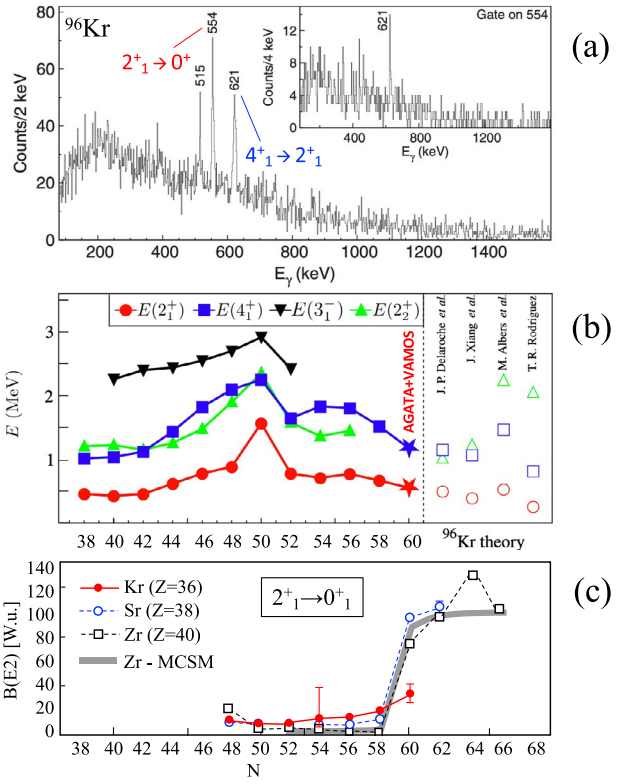

Fig. 23 Panel (**a**): γ-ray spectrum measured with the tracking array AGATA, in coincidence with the isotopically identified fission fragment of ^{96}Kr ($Z = 36$, $N = 58$), detected by VAMOS++ [172]. The 621- and 554-keV transitions are seen in coincidence (as shown in the inset) and are assigned to the $4^+ \rightarrow 2^+ \rightarrow 0^+$ cascade. Panel (**b**): Systematic evolution of 2^+_1, 4^+_1, 3^-_1 and 2^+_2 states along the Kr isotopic chain. Predictions from various theoretical mean-field calculations for the ^{96}Kr nucleus are given on the right. Panel (**c**): Systematics of B(E2; $2^+ \rightarrow 0^+$) values for Kr, Sr and Zr, showing the gradual onset of deformation in Kr, in contrast to the sharp shape-phase transition, occurring around $N = 60$, in Sr and Zr, as predicted, for example, by Monte Carlo Shell Model calculations (thick solid line). Experimental values were obtained with various methods, including lifetime measurements with differential plunger (EXOGAM at VAMOS campaign [173], see also Fig. 55) and fast-timing techniques (EXILL campaign [143, 144, 168])

respect to triaxial deformation, as shown in panel (d) (see discussion on triaxiality in Sect. 2.4).

In recent years, state-of-the-art calculations based on beyond mean-field as well as shell model approaches (using various types of realistic interactions), started to become available to describe the properties of this $A = 100$ region [143, 175, 182–184]. In particular, predictions based on Monte Carlo Shell Model computational schemes pointed out that the shape-change phenomenon near $N = 60$ has typical characteristics of a quantum-phase transition, and in Sr and Zr isotopes it can be associated with massive proton particle-hole excitations to the $g_{9/2}$ orbit from the pf shell [143, 175, 182]. Interactive Boson Model calculations with configuration mixing also confirmed

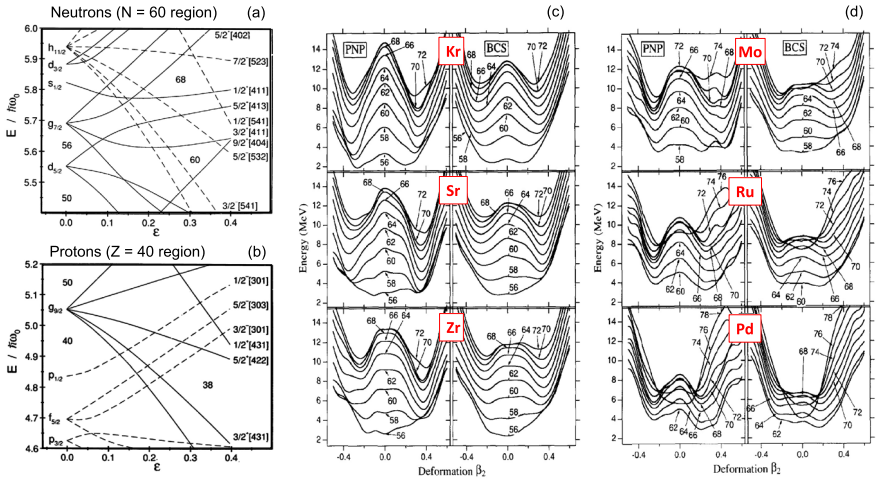

Fig. 24 Expanded portions of the Nilsson diagrams for neutrons (**a**) and protons (**b**) in the $N = 60$ and $Z = 40$ regions, respectively, highlighting the relevance of the $h_{11/2}$ neutron and $g_{9/2}$ proton orbitals for the appearance of deformation in the A=100 region [177]. Early predictions by Skalski et al., of potential-energy curves for even–even neutron-rich isotopes are given in panel (**c**) for Kr, Sr, and Zr and in panel (**d**) for Mo, Ru and Pd [178]. Calculations were performed using the Nilsson-Strutinsky method with the cranked Woods-Saxon average potential and a monopole pairing residual interaction (with two-different variant calculations, i.e., standard BCS (right) and the particle number projection method (PNP, left). Shape coexistence phenomena were obtained in Kr–Zr–Sr, and onset of triaxial instability in Mo–Ru–Pd isotopes. (Adapted from [177, 178])

that Zr isotopes provide a clear example of quantum-phase transition, originating from the crossing of two configurations with different degree of deformation [185].

A shape/phase transition has also been observed in the heavy mass, rare earth, region around A∼150, which is very well populated by fission reactions (see Fig. 3). In this case, the transition occurs from spherical to prolate, strongly deformed rotational nuclei in the even-even $N = 90$ isotones with $Z = 56$–66 [187, 188]. The change of the deformation along the proton number Z is still an open question, especially for what concerns the low-Z limit of this deformation region, while the evolution of the nuclear deformation along the neutron number N has been rather well studied [186] (see Fig. 25a and b). To describe the aspects of this phase transition and the structure changes as a function of neutron and proton numbers, both macroscopic (geometric or algebraic) and microscopic (shell-model) approaches have been used [188]. Within the algebraic models, the E(5) and the so-called X(5) are critical-point symmetries (CPSs), namely solutions of the geometrical Bohr-Hamiltonian describing nuclei at the critical points of the second- and first-order Quantum Shape Phase Transition, respectively. Such CPSs are placed between the quadrupole vibrator and the soft triaxial rotovibrator (the E(5)) and between the quadrupole vibrator and the axially symmetric rigid rotor (the X(5)), as shown in the "symmetry triangle" for nuclear structure of Fig. 26a. According to this picture, the $N = 88/90$ shape phase transition evolves into a gradual change of nuclear deformation for proton numbers Z< 60, due to increasing γ softness. In particular, the ^{148}Ce nucleus ($Z = 58$, $N = 90$) is interpreted

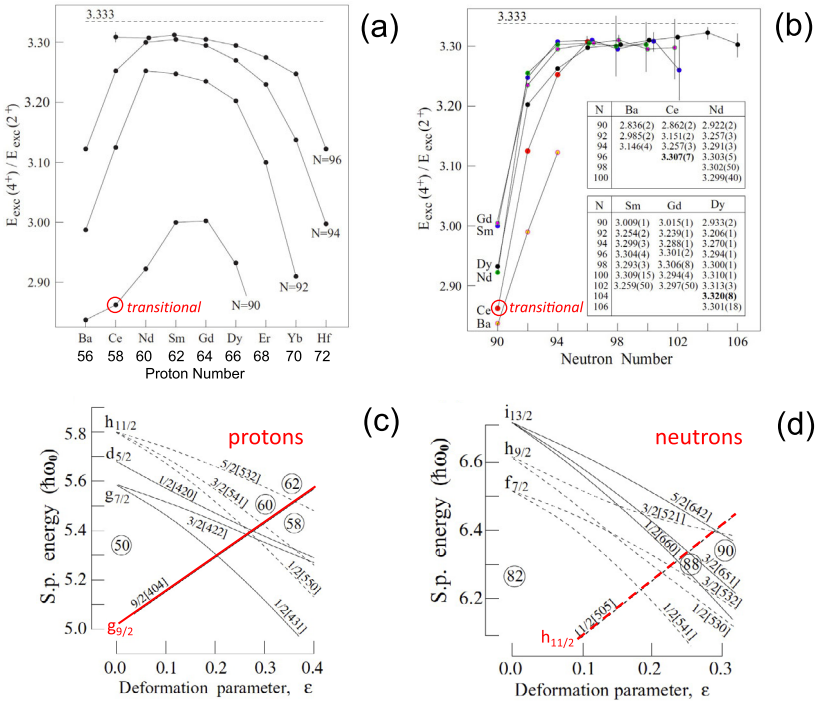

Fig. 25 Evolution of the $R_{4/2} = E(4^+)/E(2^+)$ ratio as a function of proton (**a**) and neutron (**b**) number. In the latter case, the inset tables give the $R_{4/2}$ ratio calculated using high-precision measurements of γ radiation from ^{248}Cm and ^{252}Cf spontaneous fission, performed with the EUROGAM-2 and GAMMASPHERE arrays. The limit $R_{4/2} = 3.333$, expected for a pure rigid rotor, is shown by the dashed line. Values corresponding to the transitional nucleus ^{148}Ce, located at $N = 90$, are also highlighted (see Fig. 26 and related discussions). Panels (**c**) and (**d**): schematic Nilsson diagrams for protons and neutrons, which are relevant for understanding the generation of nuclear deformation in the $Z = 60$ and $N = 90$ region (with the key orbitals $\pi g_{9/2}$ and $\nu h_{11/2}$ marked in red) [186, 187]. (Adapted from [186])

as a transitional nucleus. This is suggested by the energy ratios E_{J^+}/E_{2^+} of the excited states with J $\leq$14, with respect to the energy of the first 2^+ state, which is very close to the X(5) limit, as shown in Fig. 26b. A strong support to this picture is also given by the ratio of transition probabilities $B(E2; 4^+ \rightarrow 2^+)/B(E2; 2^+ \rightarrow 0^+) \sim 1.5$ (in between the 1.4 and 2.0 limits for a rigid rotor and a vibrator), as obtained by the lifetime analysis of the 2^+ and 4^+ states performed by fast-timing technique with the EXILL+FATIMA setup, in neutron-induced fission of a ^{235}U target [189] (see Fig. 26c).

Studies of spontaneous fission of ^{248}Cm and ^{252}Cf ahave also revealed excited states of the very-neutron rich ^{154}Ce [186]. The analysis of the ratio $R_{4/2} = E(4^+)/E(2^+) = 3.307(7)$ indicates that, in the Ce isotopic chain, the rigid-rotation limit is reached at $N = 96$, namely two neutrons "later" than in the chain of Nd isotopes. This is attributed to the proton $g_{9/2}$ Nilsson orbital in generating nuclear deformation in the A$\sim$150 region, in addition to the analogous role played by the neutron $h_{11/2}$ Nilsson orbit,

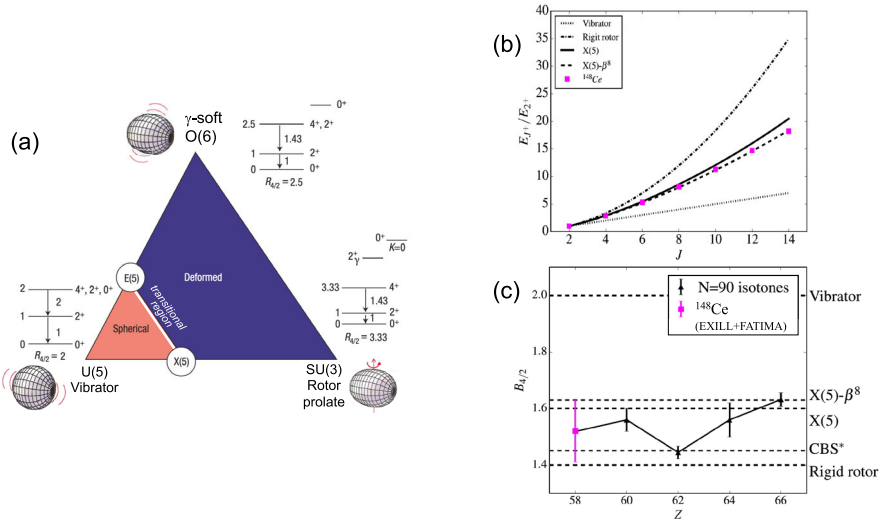

Fig. 26 Panel (**a**): The symmetry triangle for nuclear structure, showing at the vertices the traditional excitations, i.e., spherical vibrator (U(5)), prolate rotor (S(U3)) and deformed γ soft (O(6)). Corresponding schematic level schemes are also given. The critical point symmetries, E(5) and X(5), are located at the two extremes of the phase-transitional region between spherical and deformed nuclei. Panels (**b**) and (**c**): Experimental studies of ^{148}Ce (full squares), in terms of ratios of excitation energies E_{J+}/E_2^+ (for states with J $\leq$ 14) (**b**) and of transition probabilities $B_{4/2}$ (**c**) (in comparison with values for other N = 90 isotones). Both analyses point to the transitional character of the ^{148}Ce nucleus. Experimental $B_{4/2}$ values were obtained by fast-timing technique with the EXILL+FATIMA setup (^{235}U neutron-induced fission campaign). (Adapted from [188, 189])

as illustrated in Fig. 25c and d. Such high-precision studies turn out to be crucial for testing the mechanism leading to nuclear deformation in mass A=150, and the nature of the rotational bands based on "β and γ vibrations", currently disputed [187, 190].

Another characteristic feature of nuclei in the A = 150 region is the presence of isomers, in a rather wide time range (from ~20 ns to 2 μs). More than 50 isomeric states were reported by Gautherin at al., in fission fragments of ^{252}Cf, studied using coincidences between γ rays identified in EUROGAM-2 and fission fragments detected in photovoltaic cells (SAPhIR) [194]. In several cases, comparison with theory give evidence for K-isomer nature, where K is the quantum number associated with the projection of the angular momentum of a nucleus on its symmetry axis [195]. K isomerism arises from an axially symmetric deformation in the nucleus, enabling the system to be 'trapped' in an aligned spin orientation relative to its symmetry axis. The structure of such states is usually associated with breaking of one or more coupled nucleon pairs to form multiquasiparticle (multi-qp) states. This is the case, for example, of the Nd and Sm fission fragments (also studied at LOHENGRIN and GAMMASPHERE [191]). In ^{154,156}Nd and ^{156,158,160}Sm extended $K^{\pi}=(4^-)$ and (5^-) rotational bands are also observed on top of the isomeric states, in good agreement with QuasiParticle-rotor model and HFB calculations which predict two-neutron-quasiparticle isomeric excitations built on well deformed collective quadrupole deformations of the ground

state [191, 194] (see Fig. 27). In ^{160}Sm, further studied at RIKEN by in-flight fission of ^{238}U at relativistic energy, the γ decay was measured from a four-quasiparticle isomeric state, with half-life of 1.8(4) μs and a $K^{\pi}=11^{+}$ assignment (with $2\pi\otimes 2\nu$ configuration), as suggested by blocked-BCS calculations [193]). This is the lightest four-quasiparticle K isomer observed to date. The analysis of its decay pattern shows a highly K-forbidden E1 transition, in line with what observed for multi-qp high-K isomers reported in the A =160–190 region, as well as from quasi-continuum studies performed with the AGATA array in ^{174}W [196], thus supporting the important role of the level density in the determination of K-forbidden transition. At RIKEN, isomeric states were also observed in the $N = 100$ isotones of ^{162}Sm, ^{163}Eu and ^{164}Gd (with $K^{\pi} = 4^{-}$) [197, 198], in the $N = 102$ isotones of ^{166}Gd and ^{164}Sm (with $K^{\pi} = 6^{-}$) [199], in ^{168,169,170,172}Dy (with $K^{\pi} = 4^{-}$, $1/2^{-}$, 6^{-} and 8^{-}) [200–202], and in ^{158,160}Nd with (4^{-}) and (6^{-}) assignments [192]. The detailed investigation of the structure of such systems has also significant impact on the understanding of the element abundances at the A$\sim$160, which is believed to arise from a strong deformed shell closure, around $N = 100$ [203].

2.4 Triaxiality

Triaxiality describes a nuclear shape where all three axes have different lengths. In addition to oblate and prolate axially-symmetric deformed shapes, atomic nuclei were predicted since the 50's to display static or dynamic triaxial deformation [204–206] and evidence points to it being a widespread phenomenon [207]. Significant experimental and theoretical efforts have followed to establish the signature of triaxial shapes of nuclei in various mass regions, in terms of level-energy staggering as a function of angular momentum, γ-decay patterns and transition probabilities. In particular, the phase of the energy staggering has been suggested to be a measure of the degree of stiffness or softness of the γ deformation (being γ the asymmetry parameter), which is predicted to be opposite for rigid-triaxial [204] and soft-asymmetric nuclei [205] (see Fig. 28). However, an unambiguous, direct experimental signature of the presence of triaxility in most specific cases remains elusive.

While static triaxial deformation has been firmly established at high spin (in terms of wobbling mode [209–211] and breaking of chiral symmetry under rotation [212, 213]), the existence of stable triaxiality at low spin, including the ground state, is still a subject of great debate. Rare examples of rigid triaxiality have been found in low-lying structures of moderately neutron-rich ^{76,78}Ge isotopes [214, 215], following transfer and deep-inelastic reactions, while most of the nuclei, for any region of the nuclear chart, are observed to exhibit vibrational modes or "softness" with respect to the triaxiality parameter γ. As early discussed by Skalski et al. in Ref. [178], ideal systems for testing theoretical models of nuclear triaxiality are nuclei lying above the Kr-Zr region, where a sudden transition from spherical to deformed shapes is observed (see Sect. 2.3). As displayed in Fig. 24c, potential energy curves for ^{100,102}Mo isotopes (with $N = 58$, 60) were predicted to be very shallow, with γ-unstable valleys corresponding to axial deformation β_2 ranging from 0.22 to 0.30. The heavier $^{104-108}$Mo isotopes (with $N = 62$–66) were instead characterized by shallow triaxial minima at

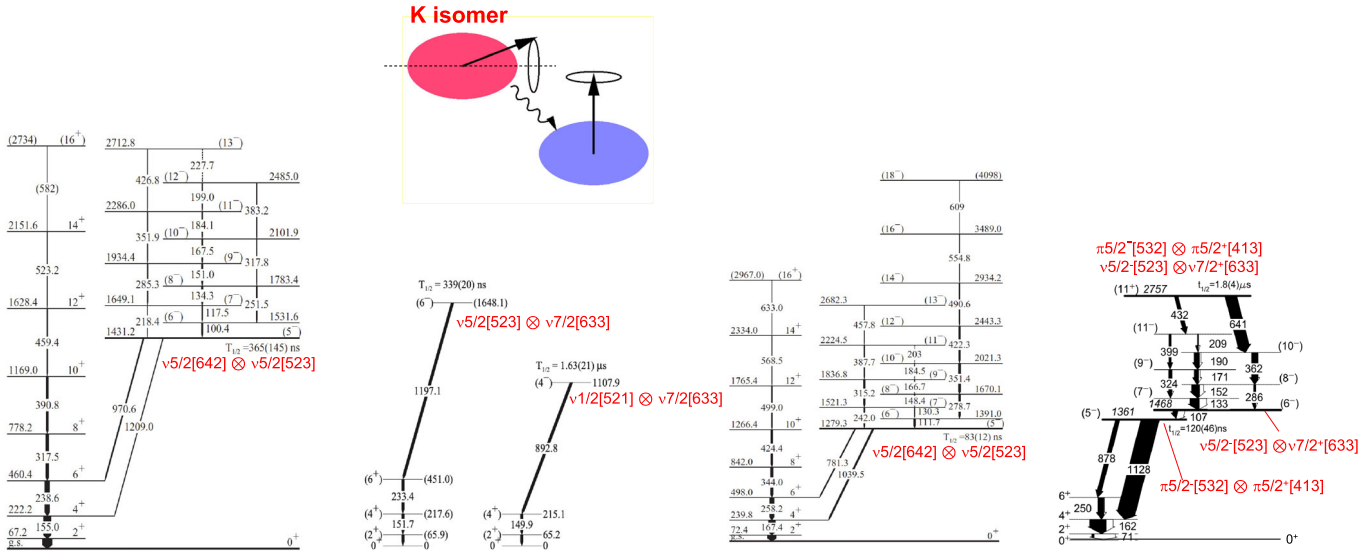

Fig. 27 Level schemes of the ^{156}Nd (**a**), ^{158}Nd and ^{160}Nd (**b**), ^{158}Sm (**c**) and ^{160}Sm (**d**) fission fragments, showing the presence of K isomers with $K^{\pi} = (4^{-})$, (5^{-}), (6^{-}) and (11^{+}). The corresponding dominant quasi-particle configurations are indicated by labels, as follows from Quasiparticle-rotor model and blocked-BCS calculations. The high $K^{\pi} = (11^{+})$ isomer of ^{160}Sm is the lightest 4 quasiparticle (2 protons and 2 neutrons) K isomer existing in the neutron-rich A=150 mass region. Rotational bands are observed on top of the low-K isomeric states. (Experimental data from LOHENGRIN and GAMMASPHERE (^{156}Nd and ^{158}Sm), and from RIKEN (^{158,160}Nd and ^{160}Sm)). (Adapted from [191–193])

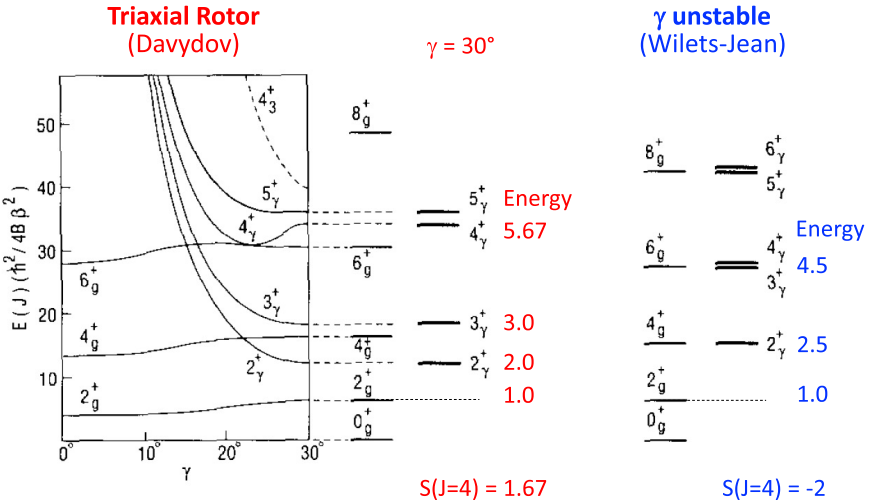

Fig. 28 Model predictions for a triaxial (or Davydov) rigid rotor and γ-soft rotor (or Wilets-Jean), for the yrast band (labelled by "g") and the γ band (labelled by "γ"). The Davydov results for γ=30^o are shown in the middle for direct comparison with the γ-soft case. The energy of the γ-band levels are also given relative to the first excited 2_g^+ state (with energy set to 1). The staggering parameter, S(J)=[E(J)-2E(J-1)+E(J-2)]/E(2_1^+), is calculated for the γ band for spin J=4, resulting in opposite sign values for the two models. (Adapted from [208])

$\gamma \sim 20^o$ and $\beta_2 \sim 0.32$. All Ru isotopes were predicted to be triaxial in their ground states, with shallow minima at $\gamma \sim 20°$.

Indeed, extensive studies of fission fragments (produced with various different fission reactions) have given indications of γ-softness and triaxial deformation at moderate spins (i.e., $\lesssim 15\ \hbar$) in the even molybdenum $^{102-110}$Mo (Z = 42) [145, 216–218], ruthenium $^{108-112}$Ru (Z = 44) [219], palladium $^{108-116}$Pd (Z = 46) [23, 220, 221] and in the $^{109-119}$Rh [222, 223] isotopic chains, in clear contrasts with the more stable behavior observed in Zr and Sr nuclei. A modest γ deformation was also reported in ^{101}Nb, ^{103}Nb, and ^{105}Nb isotopes [224].

A first indication of soft-triaxial deformation in neutron-rich Mo nuclei was reported in the 90's, when a well-developed rotational band was observed in ^{106}Mo, with the characteristics expected for a rotation based on a harmonic two-phonon γ-vibrational state (i.e., a rotational band based on a vibrational phonon with a component of angular momentum along the axis given by the quantum number $K^\pi = 4^+$) [218]. Similar structures were later observed in other neighboring systems as, for example, in the odd ^{105}Mo and ^{103}Nb nuclei [225, 226], and more recently in ^{110}Mo, following β-decay studies at RIKEN [227], which significantly extended the level scheme earlier reported by Urban et al. from spontaneous fission of ^{248}Cm [228]. We note that some doubts have been recently raised on the relevance of this multi-phonon band interpretation (i.e., the so-called β/γ band picture which follows the nuclear collective picture of Bohr and Mottelson [229]). In particular, critical reviews of experimental findings, in both spherical (A$\sim$110) and deformed (A$\sim$150) systems [187, 230], seem to point

to an alternative interpretation for a number of re-examined cases. For example, the γ-vibrational band previously reported in ^{166}Er [231] has been re-interpreted as rigid triaxial rotation, in the light of state-of-the-art large scale shell model Monte Carlo calculations [190, 232].

Establishing the nature of the triaxiality in the Mo region is, therefore, not straightforward and it is still an open question. Complementary investigations in the neighboring even-even ^{104,108}Mo nuclei seemed to point to axially symmetric nuclei [227, 234], while experimental level energies and γ-decay patterns of the odd systems ^{103,105,107}Mo were better reproduced by simple particle-rotor calculations, assuming that these nuclei have an asymmetric shape [233, 235, 236], as shown in Fig. 29a. Increasing triaxiality with neutron number was also suggested for $^{105-111}$Tc (Z = 43) isotopes (see [237] and references therein) and a possible triaxial shape was also attributed to a very low-lying band in ^{107}Tc, measured at LOHENGRIN. The band is based on a 30.1-keV, $1/2^+$ μs isomer, and is very likely the most deformed band possibly observed in the A=100 region (with quadrupole deformation $\epsilon_2 \geq 0.35$ and $\gamma \sim$ -19^o) [238]. Isomeric states were also observed at GSI in ^{112}Tc and ^{113}Tc, following the relativistic fission of ^{238}U, and their nature was interpreted as being associated with a shape change from triaxial excited states to low-lying oblate structures [239].

Moving now to Z = 44–46, in neutron-rich Rh isotopes, spontaneous fission of ^{252}Cf has revealed the existence of rotational bands in agreement with quite rigid triaxial shape: while ^{108}Ru is best described as a γ-soft nucleus, ^{110,112}Ru are more like rigid triaxial rotors [219]. In the study of triaxiality, Pd isotopes are also considered particularly interesting: high-spin states in ^{108,110}Pd, studied in heavy-ion-induced fission [220], have indicated a behavior similar to a γ-soft rotor, which moves back to an anharmonic vibrator, with less collectivity, in higher mass $^{116-120}$Pd isotopes [240, 241]. The nucleus ^{114}Pd (N = 68), which lies very close to the mid shell at N = 66, between the N = 50 and N = 82 neutron shell closures, has attracted considerable attention: it shows an energy spacing of the yrast band, in particular, following quite remarkably the ∼J(J + 6) pattern expected for both the Wilets-Jean γ-soft model [205] and the Davydov-Filippov rigid-triaxial rotor model [204], as displayed in Fig. 30a and b. Moreover, as shown in Fig. 30c, the ratio E(4_1^+)/E(2_1^+)∼ 2.6 is maximum in ^{114}Pd, although far from the rotational limit of 3.33 for axially symmetric nuclei. An inspection of the staggering parameter S(J) for the γ-band observed in Pd isotopes (Fig. 30e) also supports an inversion of the type of triaxiality in ^{114}Pd, from γ-soft to rigid rotor. In fact, for a γ-soft nucleus S(J) is expected to take positive (negative) values for the odd (even)-spin levels, and viceversa in the case of a triaxial-rigid rotor. Such a scenario has been further strengthened by recent lifetime measurements of the first excited yrast states of ^{114}Pd, by fast-timing technique, which have confirmed that ^{114}Pd is one of the most deformed Pd isotopes, pointing to a triaxiality that reaches a maximum in this nucleus (see Fig. 30d) [221].

The evolution of triaxiality as a function of neutron number has also been studied in $^{110-113}$Rh isotopes (Z = 45) with GAMMASPHERE, following ^{252}Cf spontaneous fission [242], and in the very neutron-rich $^{116-119}$Rh isotopes (far from stability), using low-energy ^{328}U fission in inverse kinematics and the EXOGAM+VAMOS setup [222]. When compared with predictions from most advanced approaches, such as the Triaxial Projected Shell Model (TPSM) [243], the energy patterns of the observed

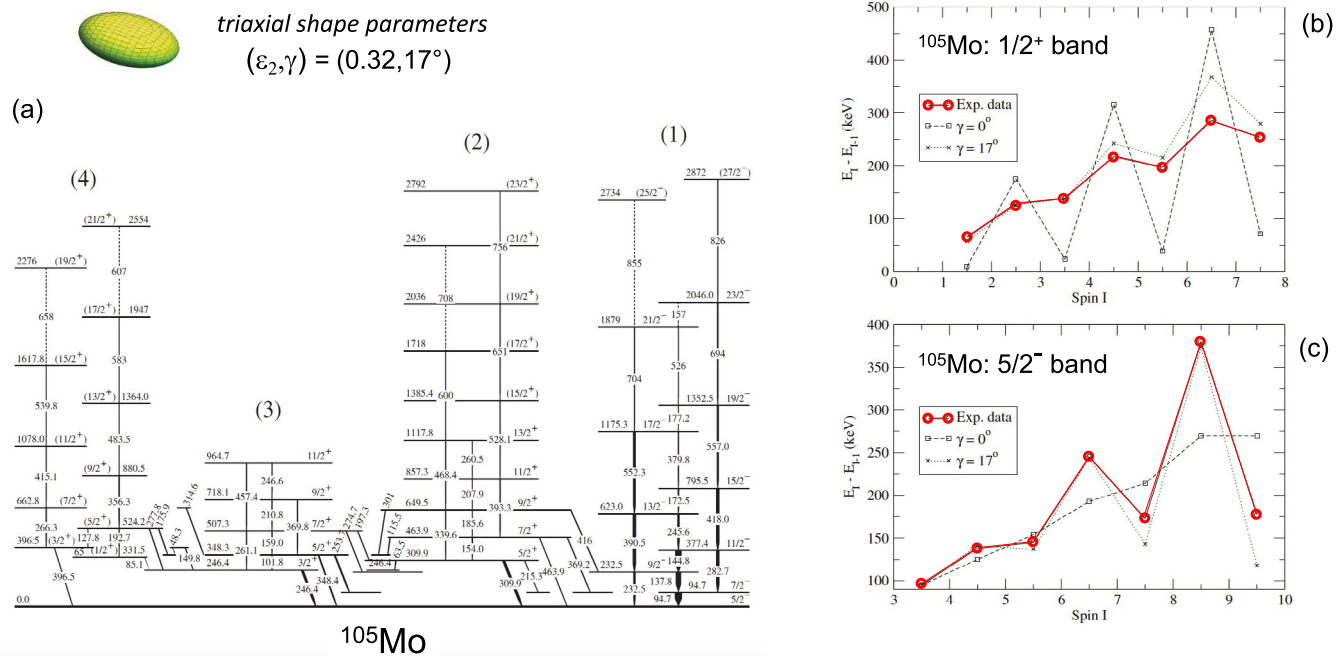

Fig. 29 Panel (**a**): Partial level scheme of ^{105}Mo (a), constructed from the analysis of prompt γ rays emitted from the spontaneous fission of ^{248}Cm and detected with the EUROGAM-2 multidetector array. The four rotational bands were interpreted in terms of simple particle-rotor model calculations assuming a well-defined asymmetric equilibrium shape (i.e., a triaxial deformation). Panels (**b**) and (**c**): Comparison of the experimental staggering (e.g., E(I)-E(I-1)) of the $1/2^+$ and $5/2^-$ bands of ^{105}Mo with particle-rotor predictions for γ deformations 0° and 17°, respectively. The best fit of the experimental data is obtained for the deformation parameters (ϵ_2, γ) = (0.32,17°), which supports the triaxiality of the ^{105}Mo nucleus. (Adapted from [233])

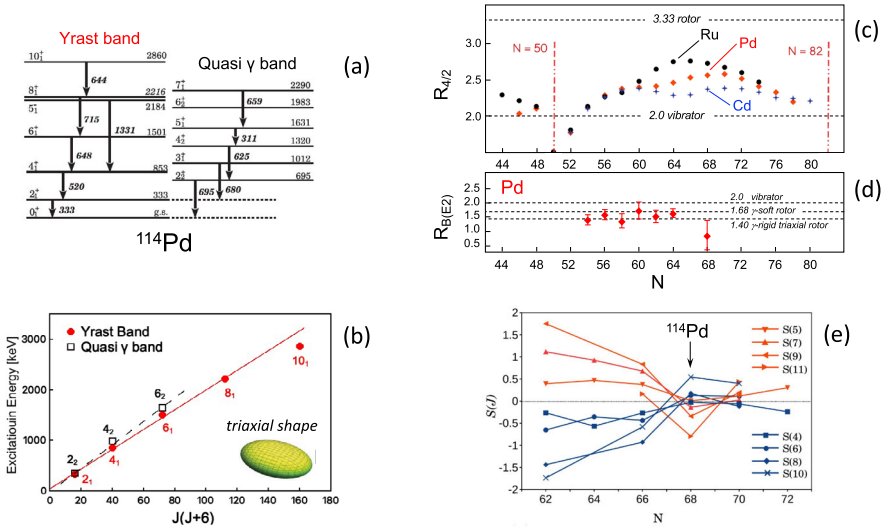

Fig. 30 Overview of spectroscopic observables for neutron-rich Pd isotopes, supporting the triaxial character of ^{114}Pd. Left, panel (**a**): Partial level scheme of ^{114}Pd (e.g., ground-state yrast band and the quasi-γ band) (panel (b)). Panel (**b**): corresponding dependence of the state excitation energy E(J) on J(J+6), being J the angular momentum (a linear trend is expected by both the γ-soft and rigid-triaxial rotor models). Right, panel (**c**): The ratio $R_{4/2}$=E(4_1^+)/E(2_1^+) for even Cd, Pd and Ru nuclei, as a function of neutron number N = 44–80 (dashed lines for expected values for an ideal rotational nucleus (3.33) and a vibrator (2.0)). Panel (**d**): corresponding $R_{B(E2)}$=B(E2;$4_1^+ \rightarrow 2_1^+$)/ B(E2:$2_1^+ \rightarrow 0_1^+$) ratios for Pd isotopes, together with the expected limits for a γ-rigid triaxial rotor (1.40), a γ-soft rotor 1.68) and a vibrator (2.0). Panel (**e**): trend, for the γ band, of the staggering parameter S(J)=[E(J)-2E(J-1)+E(J-2)]/E(2_1^+), for odd-J and even-J levels of $^{108-118}$Pd nuclei. An inversion from γ-soft to triaxial-rigid rotor is observed at ^{114}Pd. See text for details. (Adapted from [221])

rotational bands (in the most exotic systems) are found to be very sensitive to the deformation parameters, even at low spin. This points to the need for a substantial and nearly constant triaxial deformation for the yrast bands of both even and odd-mass Rh isotopes beyond ^{114}Rh, as shown in Fig. 31. These experimental results are in sharp contrast with global predictions for the evolution of non-axial shapes in the periodic table, which foresee a local maximum for triaxial shapes around N∼74 (i.e., for ^{119}Rh).

2.5 Higher-order of deformation: octupole shapes

The investigation of higher-order deformation of nuclei, for example static octupolar asymmetric shapes, is at present an experimental challenge. Since the first observation of octupole vibrations in the actinides [246–248], searches have been made for nuclei with stable octupole equilibrium shape [1, 244]. Addressing this topic is of general interest, as it can also influence the description of clusters in nuclei, evaporation of heavy fragments and asymmetric fission processes. Atoms with octupole-deformed nuclei are also very important in the search for permanent atomic electric-dipole

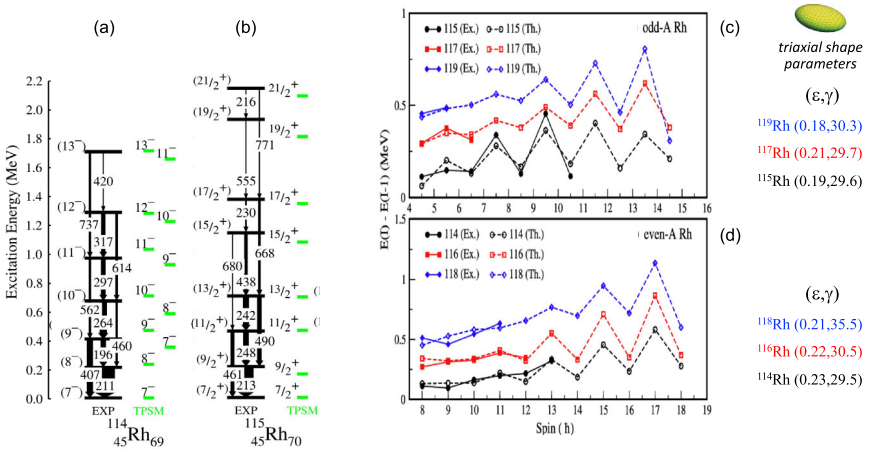

Fig. 31 Panels (**a**) and (**b**): Level schemes of ^{114}Rh and ^{115}Rh, constructed from the measurement of prompt γ rays from isotopically identified fragments, produced in the fission of a ^{238}U beam on a ^{9}Be target (at 6.2 MeV/u, EXOGAM+VAMOS setup). Corresponding excitation spectra from the Triaxial Projected Shell Model (TPSM) are also shown (in green). Panels (**c**) and (**d**): Experimental and calculated energy staggering for odd-A ^{115,117,119}Rh and even-A ^{114,116,118}Rh, respectively, showing the need for large, nearly constant, triaxial deformation (with deformation parameters given on the right of each panel). (Adapted from [222])

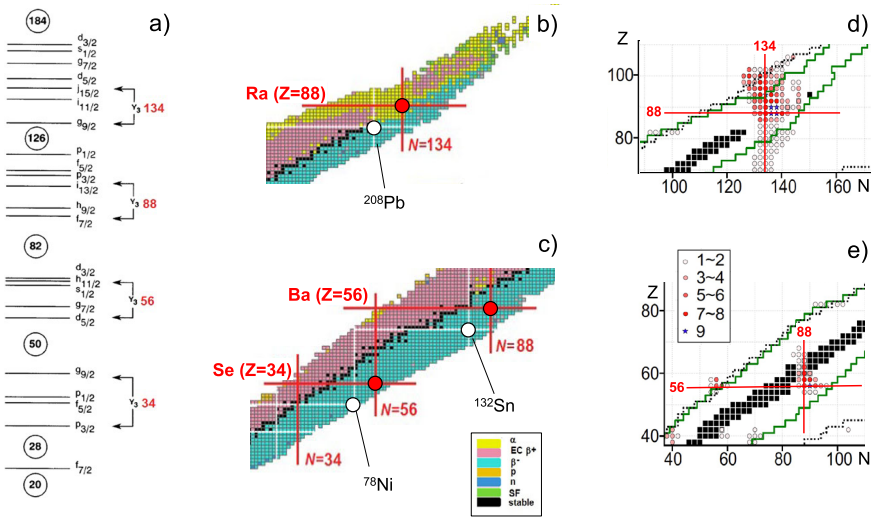

Fig. 32 Panel (**a**): the nuclear spherical single-particle levels, with indicated the most important octupole couplings, corresponding to $\Delta_j = \Delta_l = 3$. Panels (**b**) and (**c**): regions of the nuclear chart with highlighted the proton and neutron numbers having the strongest octupole coupling. White lines indicate the positions of the magic numbers. The modes of radioactive decay are given in the legend of (**c**), with stable isotopes in black. Neutron-rich nuclei around ^{144}Ba ($Z = 56$, $N = 88$) and ^{90}Se ($Z = 34$, $N = 56$), for which maximum probability of octupole correlations is expected, can be populated by fission of actinides. Panels (**d**) and (**e**): predictions for ground state octupole deformation for even-even nuclei (circles and stars) in the vicinity of ^{222}Ra ($Z = 88$, $N = 134$) and ^{144}Ba ($Z = 56$, $N = 88$), as follows by predictions based on 9 different Energy Density Functionals. The number of models predicting non-zero octupole deformation are defined in the legend. (Adapted from [244] and [245])

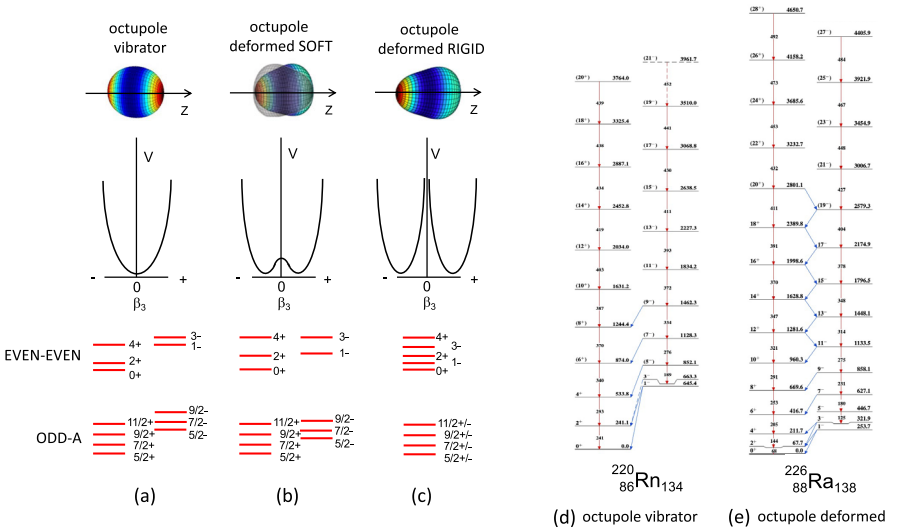

Fig. 33 Panels (**a–c**): Potential energy versus β_3 deformation plots (top), for different axially symmetric shapes – (**a**) an octupole vibrator, i.e., a rigid spheroidal nucleus (with β_3=0 in the ground state), unstable to octupole vibrations, (**c**) a rigidly octupole-deformed nucleus (with two-minima at $\pm\ \beta_3$, separated by an infinite barrier), and (**b**) the intermediate case of a soft-octupole deformed nucleus (with two-minima at $\pm\ \beta_3$, separated by a smaller barrier, though which the system can tunnel). The corresponding energy patterns for even–even and odd-A systems are given at the bottom. Panels (**d**) and (**e**): band structures for an octupole rotor (^{220}Ra) and a nucleus with stable octupole deformation (^{226}Rn). The examples are from the actinides region, where the strongest octupole correlations have been reported [36, 250]. (Adapted from [244] and [36])

moments (EDMs) that would indicate CP violation and, in consequence, the existence of physics beyond the standard model [244, 249].

Octupole vibration and octupole deformation in nuclei are produced by long range octupole-octupole correlations between nucleons, which depend on the single-particle levels present near the Fermi surface, both differing in l and j quantum numbers by 3 units (i.e., $j = l = 3$). This condition is met for proton number Z∼34, 56 and 88 and neutron number N∼34, 56, 88 and 134, as illustrated in Fig. 32a–c. Systematic calculations of octupole shapes, carried out with different techniques, indeed confirm these regions as the most promising for searching evidence for stable octupole excitations (cfr., Fig. 32d and e, and the recent work of Cao et al., [245], and references therein). It also follows that fission, as later discussed, is an ideal mechanism to search for octupole correlations in the neutron-rich regions around the "octupole-doubly magic" ^{144}Ba and ^{90}Se nuclei.

In even–even nuclei, the signature of octupole deformation is the presence of interleaved positive- and negative-parity levels forming a single rotational band, with opposite parity levels connected by large electric octupole (E3) matrix elements and decaying by fast electric dipole (E1) transitions. In odd-mass nuclei, the octupole deformation signature is the appearance of parity doublets, i.e., pair of states with the same spin, opposite parities and large E3 matrix elements between them. Much faster E1 rates are expected for members of the parity doublet as compared to neigh-

boring systems without octupole deformation (see Fig. 33). Moreover, from the study of the band structure in terms of B(E1)/B(E2) branching ratios associated to the out-of-band/in-band decay, and from the knowledge of the electric quadrupole moment Q_0, the intrinsic electric dipole moment D_0 can be deducted, assuming the rotational formula $D_0 = \sqrt{5/16}B(E1)/B(E2) \times Q_0$. Its size (of the order of 0.1 and 0.3 efm in the Ba and Ra region, respectively) is an important indication of the magnitude of the octupole correlations, whose nature (static or dynamical) can be inferred from the plot of the ratio of the rotational frequency of the parity doublets, $\omega(\pi = -1)/\omega(\pi = +1)$, as a function of the angular momentum I. This ratio should become 1 for perfectly reflection-asymmetric nuclei (i.e., octupole deformation), but equal to $4(I\text{-}3)/(4I\text{-}2)$ for rotation of an aligned-octupole phonon (i.e., octupole vibration) [251] (see also Fig. 35). Octupole shell effects for nuclei around the octupole doubly-magic ^{144}Ba nucleus have also been shown to enhance the asymmetric mass distributions produced in the fission process itself [252].

In this context, the best cases for appearance of octupole correlation are actinide nuclei with Z∼88 and N∼134, e.g., along the Rn and Ra chains. At ISOLDE, firm evidence for static octupole deformation has been recently found in ^{224,226}Ra, via Coulomb excitation experiments [255, 256]. The other extended region of octupole deformation, predicted by theory near $Z = 56$, i.e., in neutron-rich Xe, Te and Ba isotopes [206, 251] is in the well populated heavy-mass fission fragments region (see Fig. 32). Indeed, this region has been investigated at the CARIBU facility, in Argonne, in Coulomb excitation experiments with accelerated fission fragments [257, 258], at ISOLDE in β-decay studies [259], and in extended searches following fission experiments using ^{252}Cf and ^{243}Cm sources and cold/thermal neutron-induced fission on ^{235}U targets. The latter studies, already in the 80's and 90's, gave the first evidence for octupole collectivity in neutron-rich Ba nuclei [12, 254]. Figure 34 gives the most recent example of spectroscopic investigation of ^{144}Ba, performed with GAMMASPHERE, which substantially extends the original work performed with EUROGAM-2 and gives a first identification of coexistence of reflection asymmetric and symmetric shapes in a nucleus [253]. As shown in Fig. 35a and b, the entire region around ^{144}Ba is characterized by sizable intrinsic electric dipole moment D_0. In particular, ^{142}Xe, ^{144,146}Ba, ^{145,147}La and ^{148}Ce are found to display the strongest octupole correlations [12, 254, 260–264], while weaker collectivity was found in the neighboring systems of ^{140,141}Xe, ^{141,143}Cs, ^{142,144}Cs, ^{149}Ce and ^{151,153}Pr [171, 265–268]. In Pm isotopes ($Z = 61$), octupole deformed shapes beyond $N = 90$ seem unlikely to be present, as follows from recent EXOGAM+VAMOS experiments with in-flight fission of ^{238}U [269]. By inspecting the quantity ω-/ω+, shown in Fig. 35c, one notices that ^{144}Ba seems to deviate more strongly towards the stable octupole deformation limit, similarly to the heavier systems of ^{148}Nd and ^{150}Sm, mainly studied by Coulomb excitation and fusion reactions [251, 265].

As shown in Fig. 32, the region around ^{90}Se also meets the conditions for maximum probability of permanent octupole deformation. Since this region is very difficult to explore until recently only scarce information is available. In ^{90}Kr, a 3^- level found at 1506.4 keV, significantly lower than in neighboring systems, could be seen as an indication of a new region of increased octupole correlations, connected to a possible

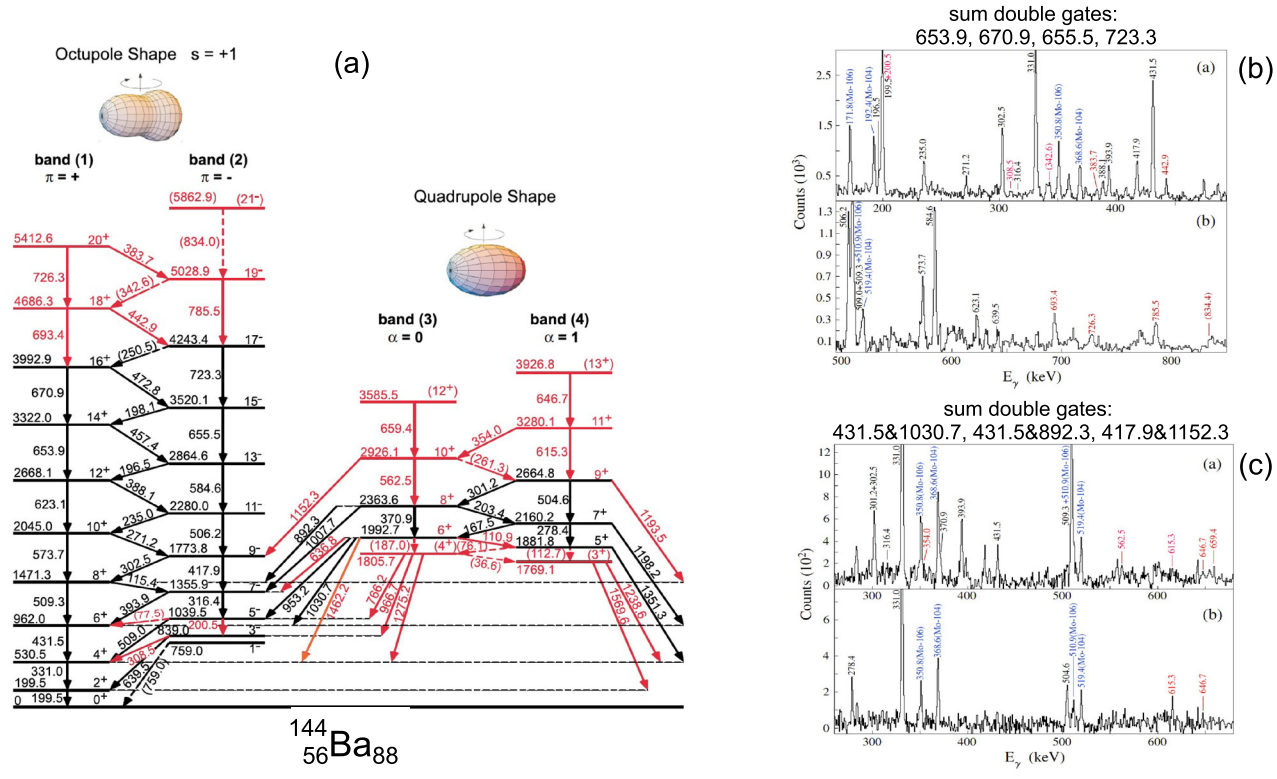

Fig. 34 Panel (**a**): Level scheme of ^{144}Ba, constructed from the measurement of prompt γ rays from spontaneous fission of ^{252}Cf (GAMMASPHERE data) [253]. Levels and transitions in black were originally identified in the analysis of ^{248}Cm spontaneous fission with the EUROGAM-2 setup [254]. Panels (**b**) and (**c**) give examples of double gated spectra obtained with GAMMASPHERE summing over the combinations of γ transitions given in the legends. They were used to expand the level scheme of ^{144}Ba (red levels and transitions). The analysis provides a first evidence of coexisting reflection asymmetric (octupole shape) and symmetric shapes (quadrupole shape) in the nuclear chart, as indicated by cartoons. (Adapted from [253])

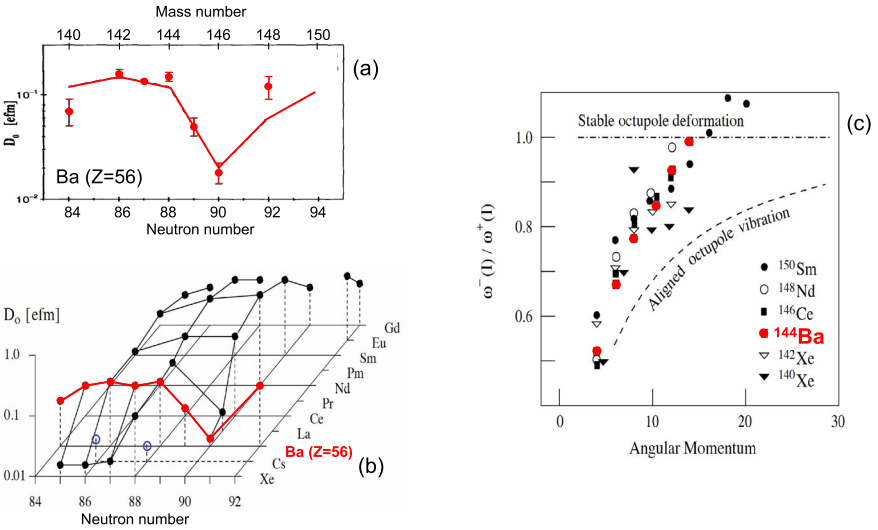

Fig. 35 Panel (**a**): Values of the dipole moment D_0 for even-even Ba isotopes with $N = 84$–94, as obtained from experimental data (symbols) [261] and theoretical predictions by Nazarewicz et al. (dashed line) [251]. Panel (**b**): Experimental values of the D_0 moment in the neutron-rich lanthanides, with lines drawn to guide the eye [266]. Panel (**c**): Ratio of the rotational frequency of the parity doublets ω-/ω+ versus spin, I, for the neutron-rich lanthanide nuclei. In all panels, red symbols refer to ^{144}Ba, one of the isotopes which deviates more strongly towards the stable octupole deformation limit [265]. (Adapted from [261, 265, 266])

growing contribution of the $\nu(d_{5/2}h_{11/2})$ pair of $\Delta l = \Delta j = 3$ orbitals to the octupole phonon [270].

2.6 The isomer spectroscopy frontier

Isomeric states generally appear in a nucleus for several different reasons [195, 271]. The nucleus may have difficulties in changing its shape to match the final state shape: this is the case of shape isomers, where a reduced overlap between initial and final state wave functions results in a significantly hindered γ decay – the most remarkable examples of shape isomers are the fission isomers in the actinide region, as discussed in Sect. 4. Additionally, the nucleus may have difficulties to change its spin, owing to a large spin difference with respect to lower energy states, which implies the emission of high-multipolarity γ rays: this is the case of the so-called spin traps. Finally, a significant change in spin orientation relative to a symmetry axis, as in the case of K isomers, can also lead to unusually long half-lives. In all cases, the details of the shell structure play a role, in particular the neutron and proton orbits. It follows that isomers give valuable nuclear structure information, owing to their unique character among the sea of many other excited states.

Isomers are present over the whole chart of atomic nuclei and can be produced by various reaction mechanisms, including fission. Long-lived (μs) isomers produced in fission reactions can be identified using mass separators, thus providing a unique access to the structure of excited states of neutron-rich nuclei. In such cases, the

detection is based on the time correlation between the fission fragment, selected by the mass spectrometer, and the γ rays (and conversion electrons) from the isomeric state, detected at the spectrometer focal plane (see Refs. [24, 25, 79]). A substantial literature exists on microsecond isomer spectroscopy in the vicinity of the doubly magic nuclei ^{78}Ni and ^{132}Sn, and in the heavy mass region around $A = 150$. As discussed in previous sections, taking advantage of neutron-induced fission (mainly of ^{235}U and ^{241}Pu targets) at the LOHENGRIN mass spectrometer at Istitut Laue-Langevin, high-sensitivity spectroscopy investigations could be performed. By moving along isotopic chains (e.g., Rb, Y, Zr, Sn, Sb, Te,...) information could be provided on single-particle orbitals (Sect. 2.1)[24, 25, 56, 57, 68, 77, 89, 94, 107, 169, 272], K isomerisms in the A=150 mass region (Sect. 2.3) [191, 268], and on complex phenomena such as shape coexistence (Sect. 2.3) [149, 153, 154, 156–160, 233, 238].

By employing similar techniques with relativistic fission of U beams, isomer spectroscopy has allowed information to be gathered on exotic, weakly populated nuclei at the extreme edges of the fission fragment population (marked by stars in Figs. 3 and 4). For example, studies performed with large HPGe arrays such as RISING [273] at the fragment separator at GSI, and EURICA [274] at the BigRIPS in-flight separator at RIKEN, pushed the investigation to the south of ^{132}Sn, by reaching high-spin isomers in ^{131}In [58], ^{134}In [275], ^{128}Cd [276, 277], ^{129}Cd [278], and ^{130}Cd [76]. Similarly, studies were carried out to the east of ^{132}Sn, towards very neutron rich systems of ^{136,138}Sn [279], ^{136}Sb [280] (also observed at LOHENGRIN [89]), and ^{140}Sb [281] (see Fig. 36). In this exotic region, isomeric states often involve high-j orbitals, therefore their study provides a strong benchmark for shell model calculations. This is the case of the $(17/2^+)$ isomer in the one-valence-hole nucleus ^{131}In, interpreted as a proton hole in the $g_{9/2}$ orbital coupled to a $\nu(h^{-1}_{11/2} f_{7/2})$ core excitation (see also Fig. 6). In the case of the 6^+ seniority isomers in ^{134,136,138}Sn, and for the 8^+ isomers in ^{128}Pd and ^{130}Cd, the isomeric configuration is based on pairs of neutrons in the $f_{7/2}$ or on maximally aligned pair of proton holes in the $g_{9/2}$ orbit, respectively (see also Fig. 8).

As already mentioned above, in the high-mass fission peak, extensive investigations were also performed in the deformed $A = 150$ mass region, mapping a number of high-K isomers in Nd, Sm, Gd, Eu and Dy nuclei, [192, 193, 197–202]. Selected examples are shown in Fig. 27.

At RIKEN, extensive searches of microsecond isomers were also performed in the low-mass fission peak: the γ decays of more than 50 microsecond isomers with half-lives of $\sim$0.1–10 μs were observed in very neutron-rich isotopes from ^{59}Ti to ^{126}Ag [79], using at first a limited γ array. Further detailed investigations, with the EURICA setup, provided additional information in the neighborhood of ^{78}Ni (e.g., on ^{76}Co [282]), and on nuclei in the upper edge of the low-A mass peak, such as ^{125,126,127,128}Pd (with three to zero neutron holes relative to the $N = 82$ shell closure, respectively), which are also relevant for the r-process nucleosynthesis [283–285].

The rather pure single-particle configuration of long-lived high-spin isomers in the region of doubly-magic nuclei has also motivated g-factor measurements to help with assignment or confirmation of spin and parity of nuclear states in far-from-stability regions. At GSI, within the RISING campaign [273], a dedicated setup was

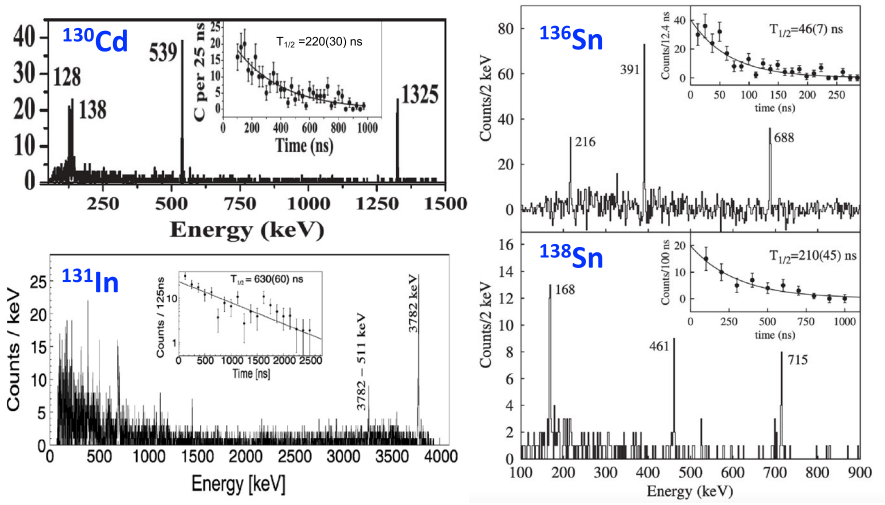

Fig. 36 Examples of isomer-spectroscopy investigations performed at the focal plane of the mass separator at GSI (left) and RIKEN (right). Fission of ^{238}U beams at 650 MeV/u and 345 MeV/u, respectively, impinging on thick ^{9}Be targets, is used to populate isomeric states in the one- and two-valence-proton nuclei ^{131}In ($17/2^+$) and ^{130}Cd (8^+), and in the four- and six-valence-neutron systems ^{136}Sn (6^+) and ^{138}Sn (6^+), located at the edge of the fission fragment population. In all cases, the isomer configuration is based on high-j orbitals (see Figs. 5b, 6 and 8). Experimental data are from the RISING [273] and EURICA [274] campaigns. (Adapted from [58, 76, 279])

used to measure the g factor of microsecond isomeric states produced by relativistic fission of a ^{238}U beam [286] (see Sect. 7.5). In particular, the study of the $19/2^+$ isomer of ^{127}Sn gave evidence, for the first time, of significant alignment in fission fragments produced at relativistic energies [286]. Moreover, the deduced g factor of the 7^- ($T_{1/2} = 5.9(8)$ μs) isomeric state of ^{126}Sn, located at 2219 keV, confirmed the $\nu(h_{11/2}^{-1}d_{3/2}^{-1})$ configuration proposed for the 7^- isomers in neutron-rich Sn isotopes [287]. With the same setup, additional g-factor investigations of high-spin isomers in Sn and Pb isotopes were also performed exploiting relativistic fragmentation reactions [288, 289].

As discussed in this work, complementary information on isomeric states with shorter half-lives (below 1 μs) can also be obtained with large arrays coupled to large-angle magnetic spectrometers, such as VAMOS [105, 146], and to fission fragments detection/tagging systems (e.g., the FIFI spectrometer, the SAPhIR solar cell array, the FIPPS active target [164, 194, 290, 291]), in addition to the most recent use of beam pulsing with fast neutron-induced fission with the nu-Ball array [165]. Details are given in Sect. 7.

All these data provide very strong benchmarks for single-particle orbits and shell-model interactions far from stability.

3 Nuclear astrophysics

Since more than 50 years, it is well known that about half of the elements heavier than iron are produced via rapid neutron capture (the so-called r process) [292]. In the last few years, experimental evidence indicated that the bulk of the r-process nucleosynthesis occurs during the merging of small compact objects, such as binary neutron stars or a neutron star and a black hole [293, 294]. However many uncertainties still remains, in particular on the type of neutron-rich nuclei involved. Indeed, the r-process reaction path involves a vast majority of nuclei lying far away from the β-stability valley and close to the neutron drip line, not yet accessible experimentally. As a consequence, r-process theoretical calculations rely heavily on extrapolations towards heavier and more neutron-rich systems, using some key input parameters, such as nuclear masses, β-decay half-lives ($T_{1/2}$) and β-delayed neutron emission probability (P_n) [295]. Predictions for such quantities may vary greatly for nuclei far from stability, being also strongly influenced by specific nuclear structure properties, in particular the shape and deformation of the nucleus [296]. It is found that change in deformation as nucleons are added results in large uncertainties in the β-decay half-lives, therefore in the placement of the r-process path. Moreover, the properties of nuclei along neutron-shell closures (in particular the so-called waiting point nuclei, for example at $N = 82$, where equilibrium between neutron capture rates and photodisintegration is reached) are expected to impact the element abundance peaks (e.g., around $A = 132$). This calls for detailed spectroscopic studies of poorly known nuclei adjacent to the rapid neutron capture region.

The important role of fission studies for astrophysics resides especially in the fact that fission produces nuclei close to the r-process path (see Figs. 37a in comparison also with Figs. 3 and 4) As discussed in Sect. 2, a key outcome of detailed γ-spectroscopy investigation of fission fragments is the understanding of the evolution of nuclear structure properties far from stability (e.g., shape evolution and shape coexistence), and the degree of single particle orbital migration for neutron rich isotopes, in particular around doubly magic ^{78}Ni and ^{132}Sn and along the $N = 50$ and $N = 82$ neutron-shell closures. As stated above, such properties directly impact lifetimes for β-decay processes, which compete with neutron-capture reactions, thus leading to important constraints on the sites for r-process nucleosynthesis. Fission studies also allow for direct measurements of β-decay lifetime of the ground state and long lived β-decaying isomers of the most exotic fission products, deep into the r-process path. Remarkable examples are the experiments performed at RIKEN within the EURICA campaign [274], employing intense ^{238}U beams ($\sim$ 10 pnA) at 345 MeV/u, impinging on a target. They gave access to β-decay half-lives of 110 neutron-rich isotopes of the elements from Rb ($Z = 37$) to Sn ($Z = 50$) [297], and of 94 neutron-rich isotopes of the elements from Cs ($Z = 55$) to Ho ($Z = 67$) [298], thus allowing to strongly benchmark theory predictions in these exotic regions.

Next to structural properties, fission barriers and fission fragment distributions play also a central role in the modeling of r-process calculations. Such information has become even more critical after the hypothesis that fission recycling could be one of the important processes responsible for the production of heavy elements in explosive scenarios, in combination with neutron capture [302, 303]. In environments with very

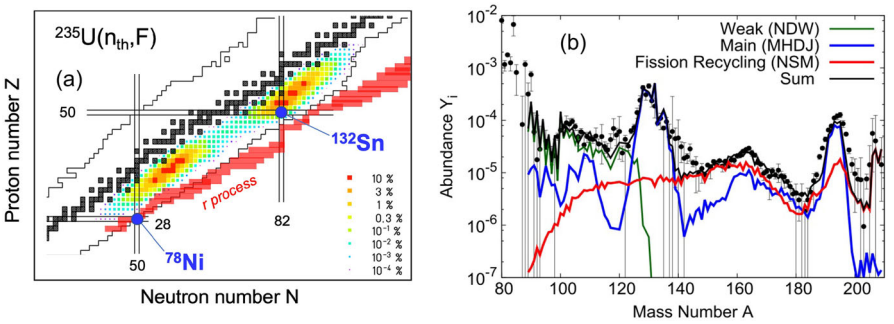

Fig. 37 Panel (**a**): portion of the (N,Z) nuclear chart showing the r-process nucleosynthesis path (in red) for nuclei in the vicinity of doubly magic ^{78}Ni (Z = 28, N = 50) and ^{132}Sn (Z = 50, N = 82). These regions can be approached using fission reaction mechanisms, as indicated by the yield distribution (in %) of thermal-neutron induced fission of ^{235}U (calculated by the ABRABLA code), here used as a reference (see Figs. 3 and 4 for ^{252}Cf spontaneous fission yields). Grey squares show stable isotopes (adapted from [299], see also [300, 301] for fission yields calculations). Panel (**b**): Comparison among observed r-process abundances in the solar system and average final abundance patterns for the fission-recycling environment of neutron star mergers (NSM) (red line), and the main r-process abundances from the MHDJ model (blue line), and the weak r-process abundances (green line) from the neutrino-driven wind model (NDW). The thin black line shows the sum of all contributions (taken from [302])

high number of neutron capture per seed nucleus (e.g., $\sim$1000), the r-process path may proceeds along the neutron drip line all the way to the region of fissile nuclei (A $>>$300). Here the r-process is terminated by β- or neutron-induced fission, and fission recycling can occur: fission fragments continue to experience neutron captures until β- or neutron-induced fission again terminates the r-process path. As a consequence, after a few cycles the abundances can become dominated by the fission fragment distributions, as shown in Fig. 37b. Therefore, fission recycling is expected to account for the underproduction problem above and below the r-process peaks, often found in models for the main r-process abundances.

Concerning fission cross-sections and fragment properties of great interest to nuclear astrophysics, we remind that extended investigations are carried out at the CERN n_TOF facility, for a variety of (radioactive) isotopes [304].

4 Fission isomers

Actinide nuclei are especially interesting since on the one hand they are sufficiently stable to have half-lives sometimes in the range of millions to 10's of billions of years in many cases, yet are sufficiently unstable to be very easily persuaded to fission. Unlike the superheavy nuclei, liquid drop fission barrier heights are greater than zero. However, the role of shell effects in generating extra stability in the actinide nuclei is also very important.

A striking example of shell effects in the actinide nuclei is the phenomenon of shape isomerism, where a second (or in some cases even a third) minimum exists in the potential energy on the pathway towards fission and that generally the fission

barrier has two (or more) humps. The shape isomer phenomenon was first discovered accidentally in the early 1960's. Flerov and collaborators were seeking to produce new superheavy elements beyond $Z = 102$ (Nobellium), the heaviest known at the time. It was recognised that the primary decay mode of $Z = 104$ and beyond would be through spontaneous fission with lifetimes, from extrapolated systematics, in the order of milliseconds. A delayed fission decay signal was indeed observed after bombarding ^{242}Pu with a ^{22}Ne beam with a lifetime of 14 ms. It turned out not to be the new element 104, but rather an unexpected and very interesting phenomenon—a long-lived isomeric state in ^{242}Am produced via transfer reaction [305].

What was extraordinary was that this excited state did not decay via emission of γ rays, but rather decayed via spontaneous fission. It's half-life is 3×10^{11} times shorter than the half-life of ^{242}Am, indicating a significantly lower barrier to fission for the newly found excited isomeric shape. Bjornholm (1967) later discovered that the excitation energy of the isomeric state was around 3 MeV, which made the resistance of γ decay towards the ground state even more inexplicable [306].

The first numerical calculations of Strutinsky applying shell-corrections to liquid drop fission barriers demonstrated a second minimum, or large negative correction, in the potential energy of various actinide nuclei at extremely elongated shapes. This suggested not only the reason for the hinderance of γ decay, i.e., two separate potential energy minima with radically different shape configurations with a barrier in between, but also that the phenomenon would be widespread in the actinide region [307]. This was later confirmed in a series of more and more sensitive experiments revealing the ubiquitous nature of the phenomenon in the actinide region. The island of shape isomerism covers over 30 nuclei and extends from uranium $Z = 92$ to Berkelium $Z = 97$. The middle occurs at Plutonium $Z = 94$, $N = 146$ indicating a new deformed "magic" neutron shell closure at this number [308, 309].

The stability of the shape isomers is governed principally by the fissility parameter Z^2/A, with shorter and shorter lifetimes for increasing nuclear charge as the Coulomb force, which drives towards elongated shapes, begins to dominate.

However, the most interesting part of the island from a γ-ray spectroscopy point of view are the lightest elements exhibiting shape isomers (thorium, uranium and neptunium). As fissility drops, the outer barrier is expected to increase in size, while the inner barrier decreases in size, hence favouring more the γ-decay branch between second and first minima, rather than the fission branch by penetration of the outer barrier and spontaneous fission. Large-scale research into fission isomer properties stopped in the early 1980's and has been relatively dormant. However, a review of the available literature on the γ spectroscopy of fission shape isomers was made in 2002 [313]. The current γ-ray spectroscopy data available for the decay of fission shape isomeric states, either by back-decay to the first minimum or deexcitations in the second well, are very sparse

The only case where high resolution (Ge) γ spectra have been obtained for decay of excited states within the second minimum was seen in ^{240}Pu [310] (see Fig. 38). Only four shape isomers are known where the back decay to the first minimum has been observed in ^{237}Np, ^{236}Np, and ^{236,238}U. However, many more are predicted to exist, particular in the lightest actinides [314–316]. The most well know case is the

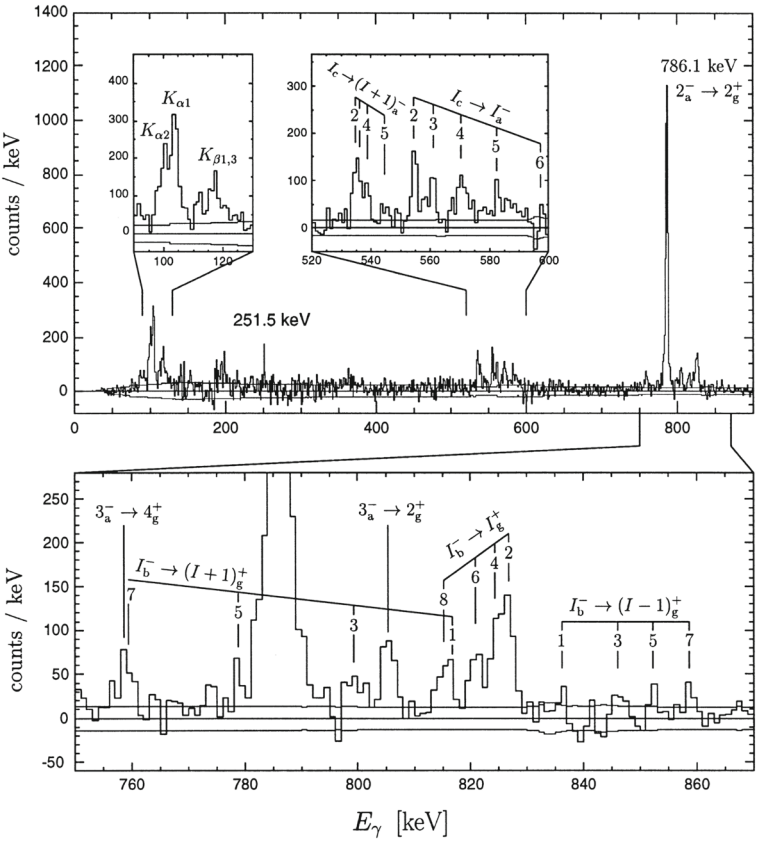

Fig. 38 Gamma ray spectrum of decays within the second minimum of the ^{240}Pu shape isomer [310]. This is the only existing case where a high-resolution Ge spectrum has been acquired

back-decay of ^{236}U [312], where several γ decays to states in the first minimum are known (see Fig. 39).

Some very interesting outstanding questions are, what are the precise energies of the isomeric states and the heights of the inner and outer barriers? What is the nature of the decay processes? What is the branching ratio between γ and spontaneous fission (sf) decay? Which states in the first minimum do the isomers decay to? What is the character of the states within the second minimum? What are their lifetimes, and deformations and moments of inertia? The answer to these questions are important for benchmarking fission models, understanding the path to fission and indeed the fission process itself. More intriguingly, there is some evidence that for some thorium isotopes, the fission barrier actually becomes triple humped and indeed it would be interesting to explore γ decays in these nuclei [309].

A renewed experimental effort on study of γ-ray spectroscopy of fission shape isomers therefore looks a promising avenue for future studies particular with the state of the art high-efficiency, high-resolution γ-ray spectrometers available today.

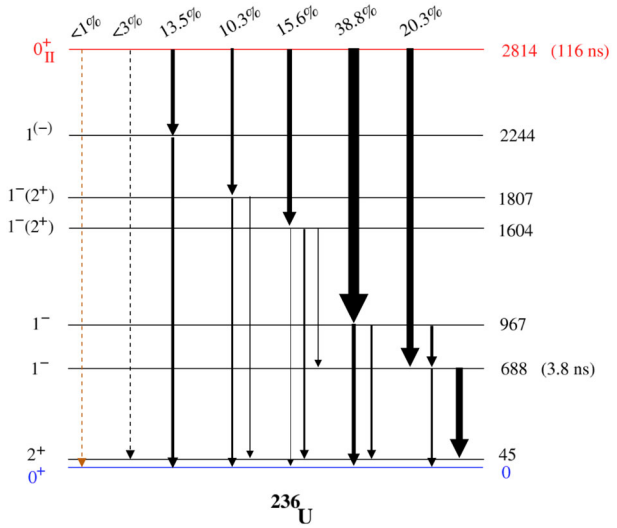

Fig. 39 Level scheme of back-decays from the second minimum to the first minimum in the ^{236}U shape isomer [311, 312]

5 Fission mechanism and dynamics

5.1 Using γ spectroscopy to measure fission yields

One important experimental and theoretical problem since the discovery of fission is to account for the probability distribution of the hundreds of different fragments that are produced, i.e., measuring and explaining the fission yields. This information is needed to understand the configurations at scission and the shell effects which drive the rapidly deforming compound nucleus from the saddle point (point of no return) to the scission point (fragment separation) [317]. Fission of actinide nuclei leads to an asymmetric distribution of fission fragments with a heavy peak centered around mass 140 and a lighter peak which moves up or down in mass with the mass of the fissioning system. Spherical and deformed shell effects are the key driver of these asymmetric mass splits, in particular doubly-magic ^{132}Sn and the octupole double-shell closure at ^{144}Ba.

Fission yields are also crucial for energy applications, the importance of which are explained in Sect. 6.

To measure fission yields directly in normal kinematics is very challenging due to relatively low velocity of the outgoing fragments. It is very difficult to directly measure their mass and charge with good precision. For thermal neutron induced fission of fissile isotopes, spectrometer based techniques (e.g., at LOHENGRIN) have successfully provided important data (see for example Ref. [318]). In recent years, approaches using inverse kinematics [319] have been also very successful at determining high precision ($\Delta A, \Delta Z < 1$) yield information. However, in inverse kinematics the major difficulty is the ability to control the excitation energy and angular momentum of the fission-

ing system. Furthermore, neutron-induced fission cannot be studied directly by this method since neutron targets are unavailable.

Although direct measurements of fragment charge and mass are preferable, the use of high resolution γ spectroscopy to measure fragment yields offers a complementary technique, particularly for systems which cannot be studied directly in inverse kinematics (i.e., neutron-induced fission). The excitation energy and angular momentum inputs are fully controlled, however, performing high precision measurements is challenging.

High resolution γ-ray spectroscopy has thus existed as an alternative method for normal kinematics since the beginning of the 1970's. It enables determination of fission yield information by measuring the intensities of γ rays emitted from individual fragments.

Usually coincidence measurements must be employed to gain the necessary selectivity. Typically the intensities of coincident transitions between low lying states are measured. However, the difficulty of this technique is to ensure that there is no missing intensity from unobserved γ rays that would have contributed to fragment yield. This missing intensity could be from extremely short-lived states, from isomeric states where the γ rays arrive later than the coincidence window, from unincluded weak γ-ray feeding branches, or from statistical side feedings of ground state and low-lying excited states.

For even-even nuclei, the measurement is more straightforward since a large fraction of the intensity usually passes though the $2^+ \rightarrow 0^+$ transition. For odd nuclei, the measurement can be fraught with difficulty since cascades can be highly fragmented forming multiple pathways to the ground state. The considerably higher level densities in these nuclei ensure many γ transitions between states and many low-energy γ rays that are either strongly internally converted or are below the energy detection threshold and hence intensity can be missed, leading to an inaccurate yield. Achieving relative yield accuracies of less than 20–30% is thus challenging. For a detailed description of the various methods for extracting yield information we refer to Ref. [320], which makes use of triple γ coincidences from the ^{235}U(n,f) reaction, measured during the EXILL campaign at the ILL facility.

The first attempt for ^{252}Cf spontaneous fission was made by Cheifetz et al. [10]. Subsequently, the technique was used with the third generation of γ-ray spectrometers to improve accuracy and study many more fragment yields than previous experiments [16], which can be seen in Fig. 40. Extension of the technique to measure yields from heavy ion induced fission reactions have also been performed [321, 322].

Moreover, the phenomenon of ternary fission, where the nucleus splits into two partners plus a third lighter particle (e.g., alpha) has also been explored using the spectroscopic technique [324, 325].

With high statistics data sets an additional possibility exists to measure the relative population intensity of particular fragment *pairs*. For each isotope pair the number of neutrons emitted can be deduced indirectly. For example the coincident detection of γ-rays from ^{142}Ba and ^{106}Mo from a ^{252}Cf spontaneous fission source indicates the emission of 4 neutrons for these events. By comparing relative intensities for a large number of fragment pairs via spectroscopy it is possible to deduce the neutron multiplicity distribution for each pair of Z's. Yield measurements using this method

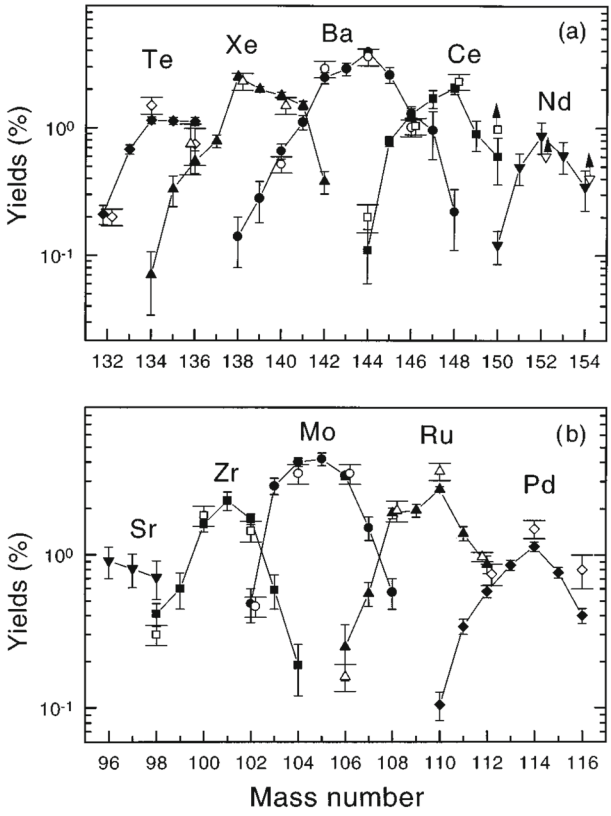

Fig. 40 First measurements of the fission yields for even-even nuclei from the ^{252}Cf spontaneous fission using γ-ray coincidence spectroscopy with the Oak Ridge escape suppressed spectrometer (taken from [323])

led to the discovery of a new type of fission mode in ^{252}Cf spontaneous fission which is interpreted as involving a hyperdeformed scission configuration (3:1 axis ratio), very low total kinetic energy and very high fragment excitation energy. A very large number of neutrons (from 8 to 11) was indirectly observed to be emitted for certain isotope pair [326]. These remarkable results were subsequently confirmed in a later publication [327] albeit using the same large data set but with improved analysis techniques (see Fig. 41).

Fission yields for neutron induced fission are particularly important due to their direct link with energy applications. The evolution of neutron-induced fission yields as a function of the incident neutron energy was first studied for the key fissile nucleus, ^{235}U [328]. Yields for fast neutron induced fission of ^{238}U -the major component in reactor fuel- were measured using the spectroscopic technique [329, 330]. The reported anomaly in [329] can be explained as a heavily-increased statistical side-feeding of 2^+ states around the doubly-magic ^{132}Sn rather than a decreased spherical (S1) fission mode which was originally suggested [331]. These results highlight the importance of the inclusion or correction for potential missing sources of γ feeding when using γ-ray intensities to measure fission yields [320].

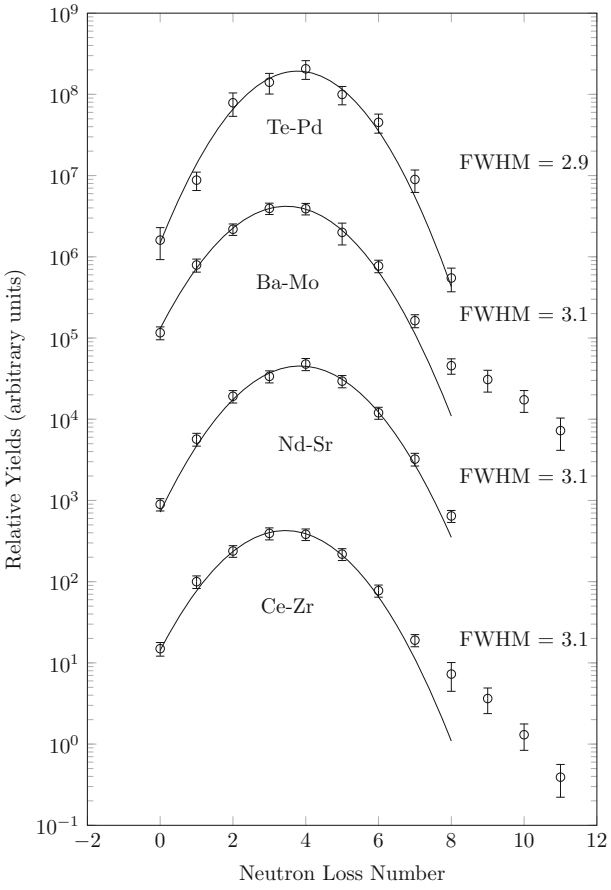

Fig. 41 Confirmation of an excess of neutron evaporation which populates certain isotope pairs in the ^{252}Cf spontaneous fission reaction. It is interpreted as the existence of a hyperdeformed fission mode (taken from [327])

5.2 Gamma rays as a probe of fission dynamics and reaction mechanism

Another important aspect of the study of fission is the fission mechanism itself. Recent reviews on the recent experimental results on the mechanism and dynamics of fission have been published in Ref. [332] and accompanying theoretical approaches have been reviewed in [333].

For spectroscopic studies the prompt fission γ rays carry important information on the angular momentum generated in the fission process. Fission neutrons and statistical γ rays evacuate mainly energy in the decay towards the yrast line, followed by mainly quadrupole transitions along or near yrast which mainly evacuate spin. The surprising feature of the fission process is that the fragments emerge spinning with an average spin of around 7–8 $\hbar$ in each. Angular momentum in fission was first studied in the 1970's [11], where discrete transitions to high spin were seen for the first time, but

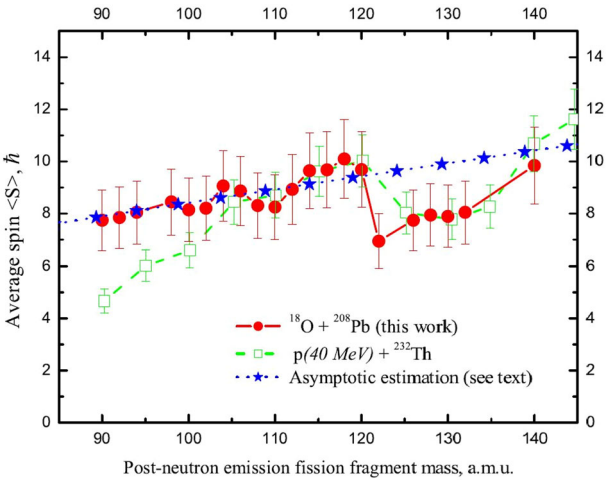

Fig. 42 Dependence of the average fragment spin at or near the yrast line for fragments produced in the ^{208}Pb(^{18}O,f) reaction (taken from [321])

also the angular correlations between γ emission and the fission axis suggested that the fragment angular momentum is produced in a plane perpendicular to the fission axis.

The average spin of a fission fragment at or near the yrast line can be determined from combining information on the transition intensities of γ rays feeding into and out of every observed level, with the spin of these states [15]. This technique has primarily been used to study spin effects in heavy-ion induced fission[1, 15, 321, 334, 335]. Figure 42 shows and example of the measurement of the mass dependence of average spin for the ^{208}Pb(^{18}O,f) reaction using the EUROBALL array. No strong trend is observed, but the average spin values are considerably higher than that subsequently observed in low-energy fission reactions. More recently this method was applied to neutron-induced reactions and spontaneous fission for the first time, allowing for a full investigation of the intrinsic generation of angular momentum in fission [336] and confirming earlier sawtooth patterns observed in the γ-multiplicity in experiments in the early 1970's [337, 338]. Additionally, the lack of correlation between the magnitude of the spins of fragment partners on an event-by-event basis was observed in [336] which places additional constraints on models of the fission mechanism.

Recent γ-ray spectroscopy of isomeric decays at the focal plane of the LOHENGRIN spectrometer also allowed for determination of the average spin dependence on the kinetic energy of the fragments [339]. Figure 43 reveals this anti-correlation which can be interpreted as increased deformation at scission leading to a higher average spin and lower kinetic energy and vice-versa. Similar effects are observed in more recent γ-multiplicity measurements [340].

However, many open questions still remain such as how energy is shared betwen the fragments and what fraction of it is excitation, kinetic and rotational. In order to understand the sharing of angular momentum and excitation energy at the scission point the

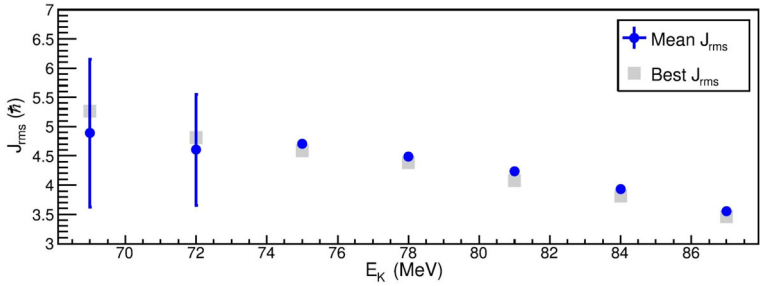

Fig. 43 Dependence of the average fragment spin in ^{132}Sn on the kinetic energy of the fragment measured at the focal plane of the LOHENGRIN spectrometer using isomeric decays (taken from [339])

simultaneous measurement of different observables is needed, often achievable only via indirect measurements or requiring model-dependent corrections.

Theoretical study of the reaction mechanism is currently very active. There is disagreement between theorists on whether neck formation and rupture after the saddle point is fast and non-adiabatic [341] or slow and adiabatic with multiple exchange of nucleons occurring during the process [342]. Much recent theoretical work has also focused on the mechanism behind the angular momentum generation in fission and the interpretation of the available experimental data [343–347].

Other ways in which γ-ray spectroscopy has been used to probe the fission reaction mechanism includes the detection of GDR γ rays which can be used to gain information on the timescale of the process [348] and the study of fission modes in heavy ion induced fission [349]. The use of gamma-ray angular correlations can also provide information on the relative orientations of angular momentum vectors in pairs of fragments [350], which may also give insights into the reaction mechanism.

6 Applications

The study of γ-ray emission in nuclear fission has a direct relevance for nuclear energy applications. Firstly, direct γ heating effects arise during reactor operation as the chain reaction procedes. Secondly, there is a continued energy release after reactor shutdown in the form of decay heat which arises from β-decays and γ decays of long-lived isomeric states. Thirdly, the unique γ-decay patterns and intensities from fission fragments allow deduction of fission product yields with a mass and charge resolution of 1 unit.

Important experimental programs related to nuclear data for applications are carried out at the European Commission's Joint Research Centre (JRC) of Geel in Belgium [351], at the Los Alamos Neutron Science Center (LANSCE) [352], and at the Budapest Research Reactor in Hungary [353].

6.1 Uses of fission yield data

The extraction of fission yields from measurements of γ-ray transition intensities is covered in Sect. 5, since these data are also useful for modelling of the fission process. As previously mentioned, they permit an understanding of the energy landscape between saddle and scission point which in the actinides leads to asymmetric fragment mass splits and the production of hundreds of different nuclei within the fuel. However, for energy applications these data are directly relevant to calculation of the following important quantities:

- the production rates of the β-delayed neutron emitting precursor nuclei which permit the control of the chain reaction via the small fraction (typically 1%) of delayed neutrons emitted from these very neutron-rich isotopes [354];
- the production rates of β-decaying nuclei which contribute strongly to the reactor decay heat in the seconds, minutes, hours, days and weeks after shutdown. These rates are necessary for the modeling of transients after shutdown such as incidental or accidental scenarios (e.g., the Fukushima accident) [355];
- the production rates and equilibrium concentrations of neutron poisons (e.g., ^{135}Xe $T_{1/2} = 9.2\,h$) which lead to increases in reactivity in the period after shutdown as these isotopes decay away [356];
- the production of long-lived nuclear waste components, complementary to neutron capture studies (see, e.g., [357]);
- the production of gaseous fission products such as Xenon and Krypton, which account for up to 25% of all released and contribute to the degredation and aging of fuel rods and cladding over time and can cause pressure build-up in between the two [358];
- the understanding of partial and total reactor anti-neutrino spectra which can be used for non-invasive core-monitoring and reactor neutrino physics experiments [359].

6.2 Gamma-ray heating effects in reactor cores

Prompt and delayed γ rays produced in fission carry away energy and thus contribute to the total heating in a nuclear reactor core. While the fission fragment kinetic energy accounts for the majority of the energy release, around 10% of the energy at any one moment is in the form of γ rays [360]. The calculation of reactor core temperatures is a difficult problem because of the multitude of different nuclear reactions taking place in the core and the complex processes by which heat is generated, transported and evacuated. Fission products deposit their kinetic energy (typically 160 MeV/fission) in the fuel rods within micrometres of the site where the fission occured. However, core γ rays can transport heat over much larger distances of several 10's of centimetres. Hence γ rays completely dominate the deposition of energy in the non-fissile elements of the core: structural materials, reflectors, blankets or samples to be irradiated [361]. Gamma rays in a reactor core are either produced directly, e.g., via prompt emission, or indirectly after secondary reactions, e.g., neutron capture or inelastic neutron scattering. Prompt fission γ-rays are a major component of this total

reactor γ spectrum and need to be understood fully, with knowledge of the multiplicty of γ emission (typically 8 prompt γ rays for each fission) and total γ energy release needed to facilitate modeling of these heating effects. Advanced reactor simulations require a multi-physics approach (neutronics, thermal hydraulics, etc.) of which γ-ray heating is a component. In particular, advanced simulation tools are essential for the developing the next generation of reactor designs [362].

Moreover, it has been suggested that accurate data of the multiplicities of prompt γ rays from fission could be used in applications such as non-destructive assay using neutron induced fissions to help identify the mass and enrichment of fissile isotopes present in any particular sample of material (e.g., legacy nuclear waste, spent nuclear fuel, etc.) by measuring the multiplicity of prompt γ rays emitted.

Since around 2010, renewed experimental efforts have yielded many important results on the spectroscopy of global prompt fission γ-ray spectral characteristics. Measurements of total γ-ray emission spectra, average multiplicity and average transition energies have been performed for a range of important fissile and fertile actinide nuclei [363–366]. Furthermore, the multiplicity of fission prompt γ-ray emission and the population of isomeric states are spin-dependent phenomena which can only be understood within the detailed framework of the fission reaction mechanism. The measurement of fragment spin distributions and average spins and the role of angular momentum in fission is described in Sect. 5.

To summarise, the study of the γ decay of excited nuclear states in neutron-rich fission products has its main direct link with energy applications through the prompt and delayed contributions to γ-ray energy deposition. This form of energy transport and deposition cannot be ignored and is a component that needs to be included as part of the complex multi-physics of advanced reactor modeling to ensure safe and efficient designs for future energy production.

7 Technical aspects

The limits of the fission production mechanism in terms of N is of particular importance since the most neutron-rich isotopes are the most difficult to study and are by definition the most weakly populated. For confrontation of nuclear structure theory with nuclear structure experiment, it is these nuclei that provide the most extreme test of nuclear models. To populate and study the most neutron-rich nuclei generally requires that the compound nuclear system which fissions is as neutron rich as possible, and the reaction which populates it imparts as little energy as possible to avoid excessive evaporation of neutrons from the resulting fragments. For this reason, spontaneous fission and neutron-induced fission are the reactions of choice. The lack of Coulomb barrier for neutrons facilitates production of much "cooler" compound nuclei with the extra advantage of the addition of one more neutron to the compound system. While spontaneous fission sources were exploited heavily in the 1990's and 2000s to perform high-resolution spectroscopy of neutron-rich fission fragments, the trend in recent years has been towards the use of both thermal and fast neutron-induced fission as fragment production mechanisms. Moreover, inverse kinematics reactions employing U beams, at both Coulomb barrier and relativistic energies, have become

Table 1 Survey of major spectroscopy fission campaigns performed in the last three decades. Detection systems and reaction mechanisms are given in the first column, selectivity methods in column two, while typical total statistics and sources of backgrounds are listed in column three and four

Instrumentation Reaction mechanism	Selectivity	Total statistics	Backgrounds
GAMMASPHERE/EUROBALL ^{252}Cf(sf) ^{248}Cm(sf)	γ coincidences	 $\sim 10^{11}$ $\sim 10^{10}$	β decay
FIPPS/EXILL ^{233,235}U(n,f) ^{241}Pu(n,f) thermal/cold neutrons	γ coincidences	 $\sim 10^{10}$ $\sim 10^{8}$	β decay neutron capture
FIPPS ^{233,235}U(n,f) thermal neutrons active target	γ coincidences fission tag	 $\sim 10^{9}$	none, pileup
LICORNE nu-Ball ^{238}U(n,f) ^{232}Th(n,f) fast neutrons	γ coincidences beam pulse calorimeter	 $\sim 10^{9}$ $\sim 10^{10}$	(n,n'), (^{7}Li,^{7}Li') intrinsic activity
AGATA at VAMOS ^{238}U(6.2 MeV/u)+^{9}Be fusion-, transfer-induced fission	ΔA$\sim$1, ΔZ$\sim$1 γ coincidences	 $\sim 10^{8}$	Doppler from partner fragment
IC + nu-Ball (one fragment) ^{252}Cf(sf)	ΔA$\sim$20 γ coincidences	 $\sim 10^{9}$	Doppler from partner fragment
EUROBALL ^{18}O+^{208}Pb ^{12}C+^{238}U heavy-ion induced fission	γ coincidences SAPhIR fragment detection	 $\sim 10^{9}$	fusion-evaporation bkg β decay
GAMMASPHERE ^{48}Ca(6.9 MeV/u)+^{238}U ^{64}Ni(6.7 MeV/u)+^{238}U deep inelastic and fission thick target	γ coincidences	 $\sim 10^{9}$	deep-inelastic bkg β decay Coulomb excitation
Few HPGe Clovers at LOHENGRIN focal plane ^{233,235}U(n,f), ^{241}Pu(n,f) thermal neutrons isomer-decay spectroscopy	delayed γ coinc. conversion e^{-} coinc. ΔA$<$1, ΔZ $\sim$ 1	 $\sim 10^{8}$	β decay environmental bkg
EURICA at BigRIPS focal plane ^{238}U(345 MeV/u)+^{9}Be RISING at FRS focal plane ^{238}U(650 MeV/u)+^{9}Be in-flight fission isomer-decay spectroscopy	delayed γ coinc. ΔA$<$ 1, ΔZ $\sim$ 1	 $\sim 10^{6}$	β decay environmental bkg

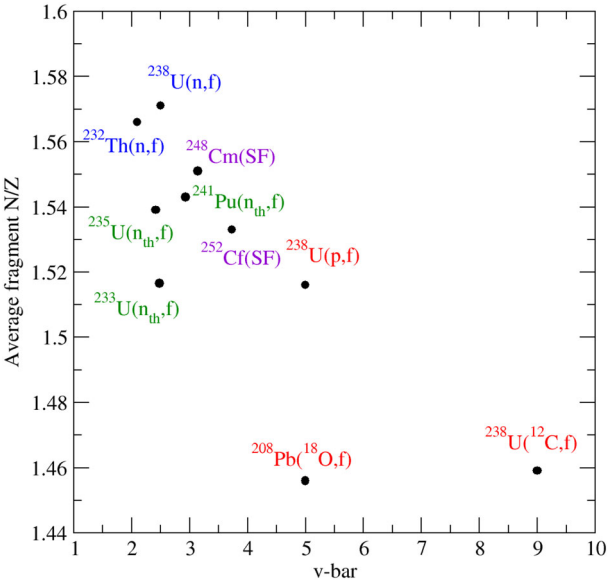

Fig. 44 Summary of the available spontaneous fission and direct-kinematics fission reaction mechanisms used to populate neutron-rich nuclei. The dependence of the neutron/proton ratio N/Z on the average number of emitted neutrons in each reaction is shown

an important tool for γ-spectroscopy studies of neutron rich fragments, in conjunction with advanced instrumentation.

7.1 Available fission production mechanisms

The ability of the various spontaneous fission and direct kinematics production mechanisms available to reach the most neutron-rich nuclei is shown in Fig. 44. The two major variables affecting this are the ratio (N/Z) on the average compound system and the average neutron multiplicity of the reaction, ν-bar. In the following, such reaction mechanisms will be briefly discussed and confronted with fission in inverse kinematics.

7.1.1 Spontaneous fission

Spontaneous fission is a natural decay process that arises in the actinide region of the nuclear chart and occurs because the nuclear surface energy and Coulomb energy are roughly in balance for nuclei with $90 < Z < 100$. The barrier against fission is low leading potentially to an unstoppable shape evolution towards deformed shapes and fission due to barrier tunneling effects. Since the Coulomb energy increases as the square of the number of protons, spontaneous fission rates increase strongly with Z and the process becomes a dominant decay mode for very heavy nuclei as the fission barrier decreases in height. Spontaneous fission sources, therefore offer the

opportunity to provide a neutron-rich nucleus factory in the laboratory without the need for accelerators, or nuclear reactors to induce the fission with a reaction.

Common spontaneous fission sources (e.g., ^{248}Cm and ^{252}Cf) have half-lives of typically several years, so there is no time constraint on their use, and no (theoretical) constraint on their activity. For this reason it is possible to accumulate very large data sets of fission events when studied with a powerful γ-ray spectrometer (e.g., GAMMASPHERE or EUROBALL) since the limiting factor is only instrument-time rather than accelerator-time which is more precious due to the resources needed to provide continuous beams. Often such sources have been used at nuclear facilities and inserted during periods of accelerator maintenance or vacations to maximize otherwise-unused instrument time. The maximum rate in the Germanium detectors (typically 10–15 kHz) limits fission rates to around 100 kHz total. Since unused instrument time is fairly abundant, huge data sets of fission events have been collected (up to 10^{11} fissions total) and therefore this method offers the largest counting statistics of all the possible fission production mechanisms.

7.1.2 Thermal-neutron induced fission

Thermal neutron induced fission of actinides can be exploited at reactor facilities. The coupling of an intense thermal neutron beam and a high sensitivity spectrometer is ideal to study fission fragments at high spin. The fission mass yields for neutron induced fission on some actinides vs spontaneous fission can be found in Fig. 45. The yields of isotopes towards mass 80 are more than one order of magnitude higher compared to spontaneous fission sources. Moreover, the large cross-section for neutron-induced fission on the main actinides can be exploited in order to make high-statistics experiments with relatively "thin" targets. Typical order of magnitudes are: beam intensity: 10^8 n/s/cm^2, target mass (^{235}U): 0.6 mg, corresponding to a fission rate of 80 kHz. The main challenge in this kind of experiments is the suppression of the neutron-beam induced background and the choice of low background inducing materials facing the neutron beam. A collimation of the neutron beam is needed, together with a proper choice of shielding materials around target position. ^{6}Li based shielding are preferred around the HPGe setup with respect to ^{10}B based shielding because of the suppression of n-induced γ background.

At the ILL, in 2013–2014 the EXILL (EXOGAM at ILL) campaign [29] of about 100 days of n-induced fission on ^{235}U and ^{239}Pu targets was operated at the cold neutron beam facility PF1B. It was the first experimental campaign of a large HPGe array (up to 46 detectors) in a reactor facility. The high flux pencil-like neutron beam allowed, with an in-beam target, both neutron capture and neutron-induced fission experiments. The use of different fissile targets showed the advantage for the comparison of γ-ray peaks in coincidence with different fission partners. In recent days, a permanent HPGe setup was installed at ILL, named FIPPS [30] (see Fig. 46), and campaigns of about 30 days were performed up to now, using ^{233}U and ^{235}U targets.

A setup with two clover HPGe detector is also installed at the facility at the CIRUS reactor (Bhabha Atomic Research Centre (BARC), Mumbai), where thermal-neutron-induced prompt γ-ray spectroscopic studies are performed [368].

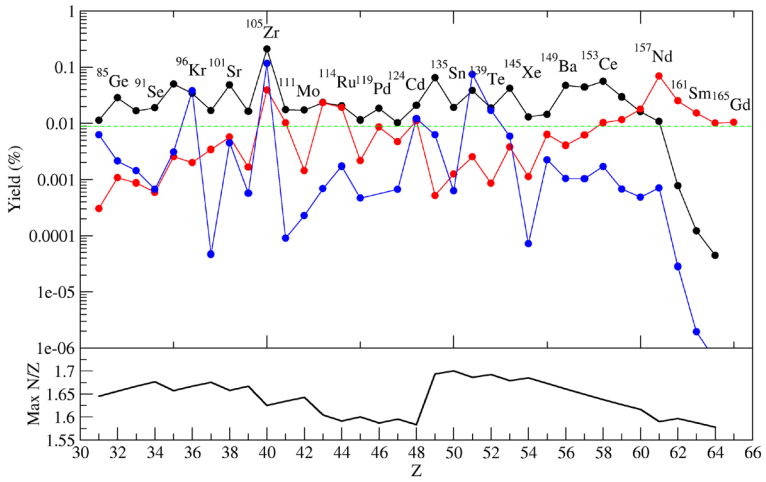

Fig. 45 Fission yields (from the JENDL evlauation [367]) of the most neutron-rich isotopes potentially accessible using *only* high efficiency, high-resolution γ-ray spectroscopy and the most favorable fission reaction mechanisms. Top panel: Black line is ^{238}U(n,f), blue line is ^{235}U(n$_{th}$,f) and red line is ^{252}Cf(sf). Bottom panel: maximum achievable N/Z ratio

In this type of experiments with continuous beam, the determination of the time of fission is very useful not only to suppress the uncorrelated background from β decay, etc..., but also to provide a start time for spectroscopy of delayed, isomeric decays. This can be done either by using γ-ray multiplicity information or, more recently, via the direct detection of fission fragments in an active target [291].

7.1.3 Fast neutron induced fission

Exploiting fast neutron induced fission as a production method is more difficult than for thermal induced fission for three reasons. Firstly, fast neutron induced fission cross sections are typically 3 orders of magnitude lower than thermal neutron induced fission (around 0.5 barns as opposed to 500 barns). Secondly the only currently viable method is to use an accelerator-based source of neutrons, which limits realistic experiment durations to two-three weeks. Thirdly, a collimated accelerator-based source is required and artificial collimation may place constraints on the source-target distance and hence the available neutron flux. To obtain the high fission rates necessary to perform high-statistics studies of fragments via γ-ray spectroscopic techniques ($>$ 10 kHz) requires neutron fluxes at least 10^7 n/s/cm^2 and targets containing tens of grams of material. Massive targets present additional problems of attenuation of low-energy γ-ray emission due to self-absorption. This problem can be mitigated by reducing the average density and extending the target volume over several centimeters.

Figure 47 shows the fast-neutron-induced setup at the ALTO facility of IJC Lab. Here, the problems of production and study of neutron-rich fission fragments by fast neutron-induced fission have been overcome using the LICORNE inverse kinematics neutron source [369, 370] coupled to the nu-Ball spectrometer [31]. LICORNE pro-

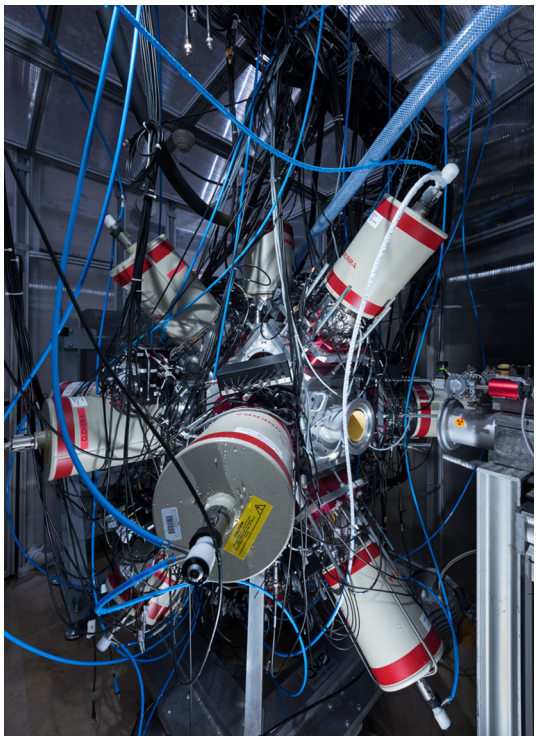

Fig. 46 The FIssion Product Prompt γ-ray Spectrometer (FIPPS) at the Institut Laue-Langevin (ILL). The array is devoted to spectroscopic studies of nuclei produced in thermal neutron-induced reactions. The basic configuration consists of 8 HPGe clover detectors and an intense collimated neutron beam. In the picture the array is coupled with additional 8 HPGe clovers from the IFIN-HH collaboration [30]

duces neutrons with energies between 0.5 and 4 MeV, just above the fission threshold of fertile actinides (e.g., ^{238}U).

A Compton-suppressed, high-resolution γ-ray spectrometer, made of 26 HeGe detectors (named GEANIE, i.e., GErmanium Array for Neutron Induced Excitations) [371], is also installed at the white high-energy neutron facility at facility of the Los Alamos Neutron Science Center (LANSCE) [352].

7.1.4 Heavy-ion induced fission

Fission induced by charged particles has an inherent disadvantage if the goal is to study nuclei as far from stability as possible. The Coulomb barrier of the target nucleus must be overcome to initiate the reaction and the extra energy needed will lead to an extra evaporation of neutrons from the fragments bringing them closer to stability. The Coulomb barrier is typically 15 MeV for protons to induce fission on a typical actinide nucleus and for heavy-ion reactions such as ^{238}U(^{12}C,f) and ^{208}Pb(^{18}O,f) as much as 78 and 92 MeV are needed, respectively. This necessary extra energy input into the compound nuclear system is evacuated through neutron emission both before and after the fission occurs. In the case of ^{238}U(^{12}C,f) this can extend from 7 to 14 neutrons in total [99]. Nevertheless, heavy-ion reactions can be very useful to access nuclei just to the right of the stability line which cannot be accessed by transfer reactions or other means.

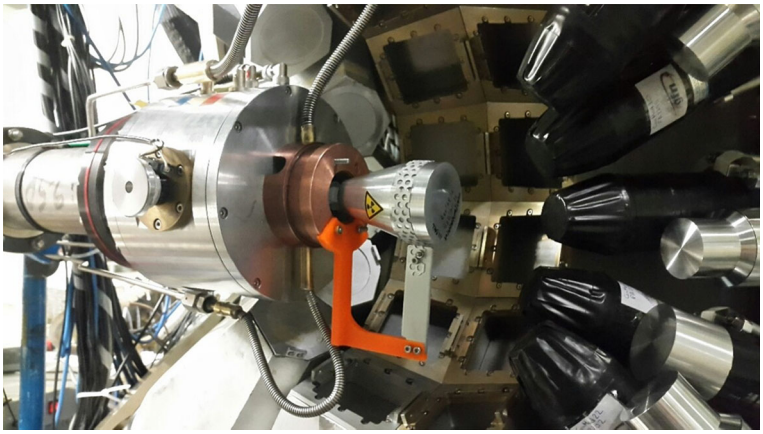

Fig. 47 The LICORNE neutron source coupled to the nu-Ball spectrometer [31] at the ALTO facility, IJC Lab. The sample in the center of the array is 71 g of ^{238}U metal turnings encapsulated in a thin aluminum case and is irradiated via the direction cone from LICORNE [369, 370]. The average target density is 0.7 g/cm^3 thus minimizes attenuation of low-energy γ rays

7.1.5 Fission in inverse kinematics

The exchange of direct kinematics fission reactions for inverse kinematics facilitates unambiguous identification of fragments and charge and mass at the focal plane of separators.

Inverse kinematics fusion- and transfer-induced fission of U beams on Be and C targets, at energy around the Coulomb barrier, permit high-precision γ spectroscopy of very neutron-rich fission fragments (at fairly high angular momenta), fully identified at the focal plane of large angle magnetic spectrometers, like VAMOS at GANIL [32, 33]. Moreover, intense, high-energy U beams available at large scale facilities, such as GSI and RIKEN, permit excellent selectivity in A and Z of the fission products via the use of in-flight separators, like FRS [34] and BigRIPS [35], to perform direct fragment detection at the focal plane. For the subset of nuclei which have isomeric states longer than the flight time of the separator (about few hundreds ns), a rich γ-spectroscopy program can be carried out for excited nuclear states in the stopped fragments, with intrinsic Ge energy resolution (see Sect. 2.6). Secondary reactions induced by fission fragments, like Coulomb excitation, transfer, pick up and knock out,..., facilitate discovery of excited states in hitherto completely inaccessible isotopes. This is at the cost of a significant Doppler broadening of the detected γ-ray transitions, due to the high fragment velocity and finite detector opening angles. As previously mentioned, such secondary reactions are beyond the scope of this review.

7.2 Resolving power of the γ-ray spectrometer

The advent of arrays of Compton suppressed HPGe detectors allowed for breakthroughs in nuclear structure studies of neutron-rich fission products. In particular,

the high sensitivity of arrays such as EUROBALL [18] and GAMMASPHERE [21] has been crucial to detect the large number of photons emitted by about 150 different nuclides simultaneously produced in the fission process. In this approach, the exceptional selectivity needed to assign γ rays to a particular fragment has been achieved. New γ rays are assigned by selecting events, among the high-fold data, with γ rays from well-known partner nuclei (see early reviews by Ahmad and Phillips [1] and by Hamilton et al., [2]).

As shown in Ref. [17], the resolving power R of an array is proportional to the Peak-to-total ratio (PT), and inversely proportional to the energy resolution ΔE

$$R = (SE \times PT/\Delta E)^F \tag{1}$$

where SE is the average separation in energy of γ rays in a particular cascade, and F is the fold of the analysis. The above formula shows the advantage of performing spectroscopy of γ rays in direct kinematics emitted from stopped fission fragments. At high v/c emission, the ΔE term from Doppler broadening degrades the resolution, and high detector granularity, or γ-ray tracking (e.g., AGATA and GRETINA [372–376]) become essential to maintain resolving power. Indeed, beam-induced fission studies performed at GANIL in inverse kinematics greatly profited from the use of the AGATA tracking array, for the study of the structure of isotopically-identified fission fragments (see, e.g., Fig. 14 and 15). Where advanced γ tracking is not available, the clover geometry is usually chosen to gain in peak-over-background via the add-back procedure, as in the case of the FIPPS and nu-ball arrays [30, 31].

7.3 HPGe detector damage from neutrons

The fission process itself is a source of fast neutrons, so fission rates of up to 100 kHz in the center of an array can produce neutron fluxes in Ge detectors of up to 200 n/s/cm^2 or fluences of 5×10^8 n/cm^2 in a 4-week experiment. For fast fission induced by fast neutrons additional fast neutron-induced flux will be present due to elastic and inelastic scattering from the target. For thermal neutron-induced fission absorption of the scattered thermal neutrons is desirable since neutron capture on ^{70,74,76}Ge isotopes will lead to transmutation of the Ge nucleus and make an irreversible lattice defect. Similarly, fast neutrons with energies > 5 MeV can transmute Ge atoms through the opening of (n, p) and (n, α) threshold reactions. Most neutron damage can be easily reversed trhough an annealing (heating) process, which restores the displaced Ge atoms back into the lattice. Gamma-tracking arrays, like AGATA and GRETINA, can recover the degraded energy resolution from neutron damage, taking advantage of information on the γ interaction point [377, 378], hence can run longer without an annealing.

7.3.1 Selectivity and background suppression

The possibility to perform detailed, high-fold γ-ray coincidence spectroscopy (fold $F \geq 3$) of fission fragments came with the advent of high efficiency, high-resolution γ-ray spectrometers. Since the resolution of Germanium is excellent (ΔE typically

2–3 keV), the selection achieved by placing a double γ gate on known transitions is sufficient in most cases. Additional selectivity (e.g., with information on fragment mass or charge) although potentially helpful is not strictly necessary. The resolving power of an array was shown in Eq. 1 to be proportional to the power of the analysis fold divided by the detector resolution. Practically, this means that it is possible to detect fragment γ rays with yields as low as approx 10^{-4} of the total. Beyond this limit, additional selectivity (e.g., in A and Z) becomes mandatory and a γ spectrometer alone is not enough. The signal sinks rapidly into the background and there is a double penalty. Gamma ray peaks in more weakly populated nuclei have fewer absolute number of counts hence resulting increased statistical fluctuations, but also fewer counts relative to the main background created by all the other fragments combined. It is this background from the other fragments that must be reduced via additional selection techniques for the signals from the most weakly populated fragments are to remain significant. Figure 45 shows the effective limit on what can realistically be studied using large γ-ray array selection power alone and the most fission favorable reaction mechanisms.

To overcome the limitation associated with the use of a γ spectrometer alone, different devices have been employed in conjunction with direct-kinematics fission studies. At ILL, for example, the use of a fission tag in neutron-induced fission reactions has been recently proved extremely efficient in the suppression of β-decay induced γ background [291]. In this case, ^{233}U or ^{235}U target material were diluted in a liquid scintillator (deuterated toluene) and fission events were distinguished from β/α decays by means of pulse shape discrimination techniques (see Fig. 48). Figure 49 shows an example of the improved selectivity in the γ spectrum from the FIPPS array, requiring the fission tag. The presence of a fission tag proved also beneficial for the study of transitions across the isomers.

Figure 50 shows instead the enhanced selectivity obtained in the γ spectrum of ^{94}Rb, populated by neutron-induced fission of ^{235}U, by gating on the complementary fragment identified in one arm of the Manchester Fission-Fragment Identifier (FiFi). The latter is based on time-of-flight (TOF) detectors and one axial ionization chamber (IC) for kinetic energy measurements of fission products, from which the mass spectrum of the complementary fission fragments can be reconstructed [162].

A solar cell array, named SAPhIR [290], was also employed with EUROGAM-2 and EUROBALL for fission-fragment spectroscopy of very neutron-rich nuclei produced in induced or spontaneous fission reaction, as schematically shown in Fig. 51. SAPhIR was used for mass identifcation, trigger and kinematic reconstruction of the fission events, for Doppler correction. The device had large efficiency, good granularity and a reduced size (suitable to fit into the scattering chamber of the HPGe array) and a weak absorption of γ rays, which preserves the sensitivity of the HPGe array.

In general, measurements in direct kinematics permit high resolving power due to the intrinsic resolution of germanium and hence neutron-rich nuclei can be explored to medium spin (typically $10\hbar$). However, to reach the most exotic species requires an extra mass selectivity from direct detection of the fragments which is best performed in inverse kinematics with U beams at either Coulomb barrier or relativistic energies, to gain a resolution in A and Z to a precision of $\leq$1 unit. This approach is used at

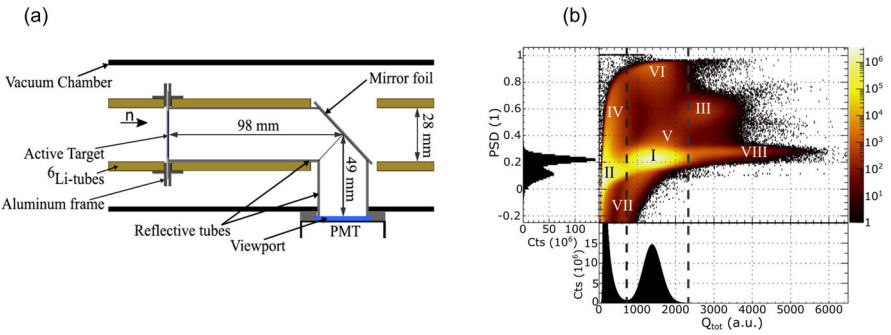

Fig. 48 Panel (**a**): Schematic view of the light readout system for the active target setup used at ILL with the FIPPS array. The scintillation light exits the target cell through the downstream sapphire window, it is guided by a highly reflective tube along the neutron beam, hits a mirror foil and is reflected towards a Photo Multiplier Tube (PMT). Panel (**b**): Example of distribution of Pulse Shape Discrimination (PSD) and total charge for a run of neutron-induced fission on a scintillating active target loaded with ^{235}U material. Side panels show the axis projections. Labels refer to different classes of events: (I) fission events, (II) electron events, (III) fission-fission pileup, (IV) electron–electron pile-up, (V) fission-electron pile-up, (VI) electron-fission pile-up, (VII) incomplete pulse integration for fission and electron events, (VIII) tail caused by particles from ternary fission. Dashed lines indicate the Q_{tot} range used as fission gate for γ-ray spectroscopy (taken from [291])

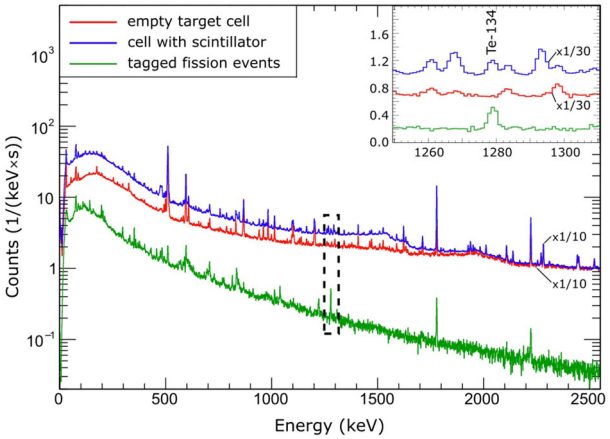

Fig. 49 Examples of FIPPS γ-ray energy spectra obtained from neutron-induced fission of ^{235}U. In red: spectra corresponding to the neutron beam impinging on the empty cell. In blue: spectra from the cell filled with U-loaded scintillator (scaled for illustration purposes). In green: spectrum tagged by the PMT signal of the active target setup, as fission events, showing an evident background suppression. In the inset: the γ-ray peak corresponding to the $2^+ \rightarrow 0^+$ transition in ^{134}Te is highlighted with a dashed box (taken from [291])

GANIL with the VAMOS magnetic spectrometer [32, 33], and at RIKEN and GSI with the BIG-RIPS [35] and FRS [34] recoil separators, respectively.

As illustrated in Fig. 52, a full isotopic separation of fission fragments is achieved, which boosts the resolving power by around two orders of magnitude. However, the statistics of collected γ-γ-recoil coincidences is considerably lower than the event rates

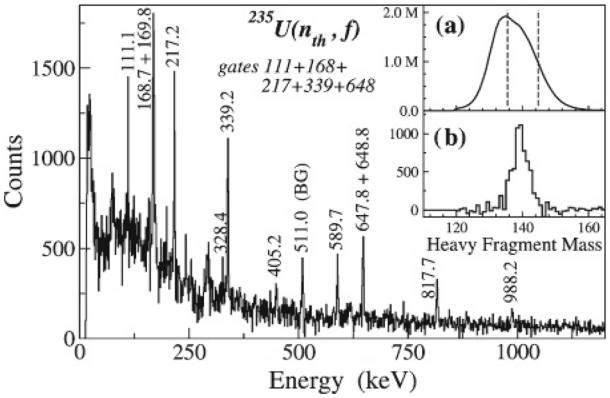

Fig. 50 Example of summed γ spectrum of coincident isomeric γ-ray transitions of ^{94}Rb obtained from the total fragment γ decay gated on the heavy complementary-fragment mass, as shown in inset (**a**). The complementary-fragment mass distribution, obtained after gating on the isomeric γ rays, is shown in panel (**b**). Data from the FIFI campaign at ILL (taken from [162])

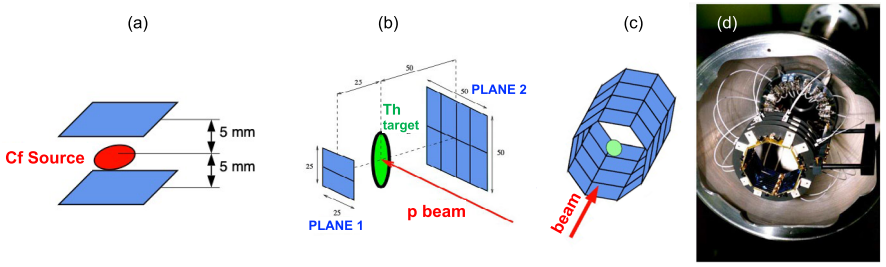

Fig. 51 Examples of the different configurations employed by the SAPhIR fission fragment solar cell array [290], in experiments with EUROGAM-2 (**a**)–(**b**) and EUROBALL (**c**). Panel (**a**): planar geometry used in ^{252}Cf spontaneous fission experiments. Panel (**b**): planar geometry used in proton induced fission experiments with a ^{232}Th target. Panels (**c**) and (**d**): barrel geometry used in fission reactions induced by a ^{12}C beam on a ^{238}U target. (See text and Ref. [20])

from γ-coincidence experiments using Ge arrays only, due to the small acceptance of the separators.

The complementarity of the various approaches is shown in Table 1 which summarizes the multitude of production and selection techniques used up until the present time. There is no one method that dominates over the others, because each one has its particular advantages and particular drawbacks. The number of γ coincidences collected also plays a significant role, with accelerator-based fission production mechanisms restricted to experiments which usually can last no longer than two or three weeks. On the contrary, spontaneous fission or thermal-neutron induced fission production can be maintained on time-scales of up to many months. For the setups with the highest A and Z selectivity, the total statistics of the data set is a less relevant figure than the individual statistics of the isotope to be studied, which is almost perfectly selected from the background of all other fragments. The limiting factor of these experiments is the requirement to observe at least few counts in the γ-ray spectrum,

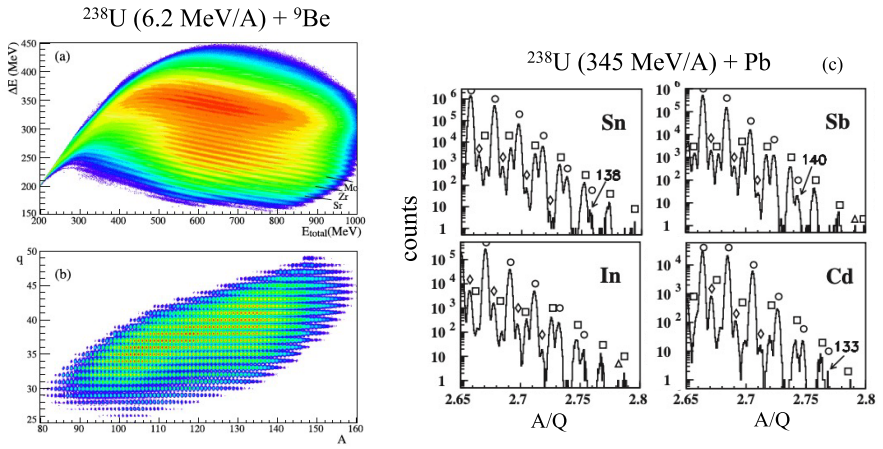

Fig. 52 Left: data from fission induced by a ^{238}U beam at 6.2 MeV/u bombarding energy on a ^{9}Be target (VAMOS data). Panel (**a**), two dimensional histograms of the ΔE vs total energy, E_{tot} of fragments detected at the focal plane of VAMOS. Panel (**b**), isotopic identification in mass and charge of the fragments [146]. Right: data from fission induced by a ^{238}U beam at 345 MeV/u bombarding energy on a Pb target (RIKEN data). A/Q spectra of Cd, In, Sn and Sb isotopes (Z=48-51) are shown. The peaks labeled with their mass number correspond to newly identified isotopes, as discussed in Ref. [379]

constituting a statistically significant peak. In the table, sources of backgrounds are also given, although they cannot be directly compared since they are unique to the particular setup and reaction mechanism.

7.4 Lifetime measurements

To understand the structure of exotic nuclei produced in fission, lifetime measurements of excited states are needed in order to determine the transition strengths and extract quadrupole moments and deformations. Approximately 95% of the γ decay of excited states of fission fragments occurs within a nanosecond [380]. For lifetimes longer than nanoseconds, lifetimes are relatively easy to measure using direct coincidence timing techniques. In the ps to ns range, fast timing techniques have recently open new possibilities, as discussed in Sect. 7.4.1. Plunger techniques are also possible (Sect. 7.4.2.1). For lifetimes lower than few ps, it becomes more challenging to extract the experimental information. Techniques are mainly based on Doppler shifted lineshape analyses, and require a full understanding of the slowing down process in the medium of the target (see Sect. 7.4.2.2).

7.4.1 Fast timing

The new scintillator matierials, $LaBr_3$(Ce) and $CeBr_3$, have been developed with an excellent timing resolution and reasonable energy resolution. Fast-timing lifetime measurements with these types of detectors give access to lifetimes in the 10 ps-100 ns range. The technique can be used with collection of Ge-LaBr3-LaBr3 coincidences or,

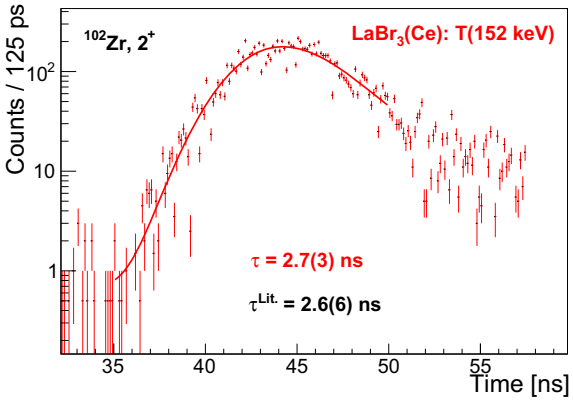

Fig. 53 Fast-timing direct measurement of the first excited 2^+ state in ^{102}Zr using nu-Ball ^{238}U(n,f) data and Ge-LaBr$_3$-BeamPulse coincidences (taken from [381])

in the case of accelerator based experiments, with Ge-LaBr$_3$-BeamPulse coincidences. The intrinsic time resolution of these detectors is dependent on size but for typicaly crystals is around 300 ps (FWHM). Figure 53 shows the reference case of the direct measurement of the lifetime of the first excited 2^+ state in ^{102}Zr (nu-Ball ^{238}U(n,f) data using Ge-LaBr$_3$-BeamPulse coincidences).

Fast timing campaigns were performed at GAMMASPHERE, EXILL and nu-Ball, using spontaneous fission sources and thermal and fast neutron-induced fission (see for example Fig. 12 and Refs. [90, 91, 143, 144, 168]). The challenge in this kind of studies is the efficiency for channel selection via γ rays. This is discussed in Refs. [382, 383], where the determination of systematic effects influencing the prompt response function of the system are considered and the analysis needed to go down to tens of ps is described. When additional selectivity is available, as provided for example by mass separator such as LOHENGRIN, the technique for decays of states fed by long-lived isomers can be pushed down to the ps limit [384].

7.4.2 Doppler shift based methods

7.4.2.1 Plunger

In direct kinematics, the recoil distance method - a Doppler based method - can be exploited due to the natural velocity of the emerging fission fragments which is around 1−1.4 cm/ns or around 4% the speed of light. The difficulty is to control precisely the velocity and the angle of emission with respect to a stopper foil, as firstly exploited in Refs. [385, 386]. Plunger devices for spontaneous fission sources were later developed by Krucken and Smith [22, 387]. In this kind of experiments a detection of the fission fragments is needed in order to constrain the angle of the recoiling fragment, as shown in Fig. 54.

Plunger measurements for fission studies in inverse kinematics were also done with EXOGAM and AGATA at VAMOS [173, 175, 223, 224, 388] (see Fig. 55). In these kinds of experiments attention needs to be paid to the mechanical stability of target and degrader, due to thermal expansion caused by the beam. The isotopic identification

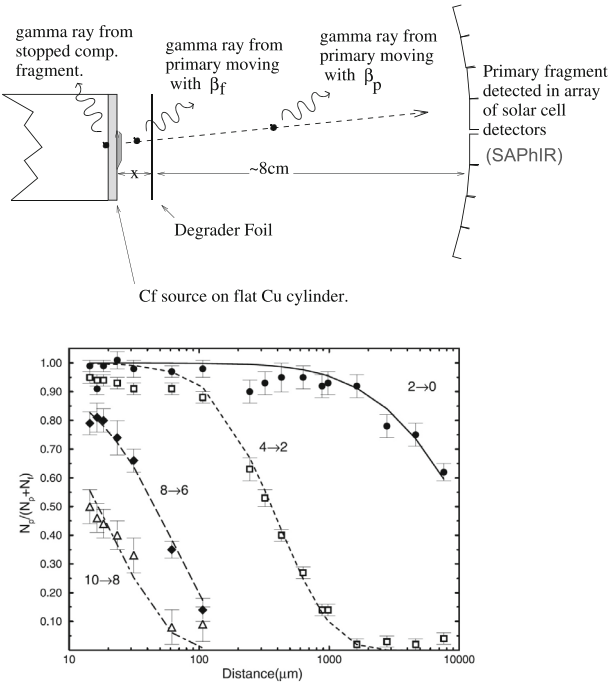

Fig. 54 Top: Schematic diagram of the differential plunger arrangement used with a ^{252}Cf spontaneous fission source, with the SAPhIR solar cell array detecting the primary fragment. The devise was used with the EUROBALL array. Bottom: Examples of curves of the ratio $f_p = N_p/(N_p + N_f)$ (N_p and N_f being the intensity of the partially- and fully-shifted components of the γ-ray lineshape) versus the distance between the source and the degrader foil. Experimental data refer to yrast states in ^{104}Mo [387]

provided by the separator together with the Doppler correction capabilities of the γ spectrometer are essential in these studies.

7.4.2.2 Line shape analysis

In the ps-fs range, lifetimes are shorter than the slowing-down time of the fragment in a heavy medium (typically the order of a 1–2 ps). If γ rays are emitted over a range of different velocities, then emitted transition will acquire a line shape that changes depending on the angle at which it is detected relative to the direction of travel. If the slowing down process is correctly modeled, then the line shape of a particular transition can be simulated and the information exploited to extract a lifetime for the state which emitted it. Doppler broadened lines were successfully analysed in this way for light fission fragments from spontaneous fission of ^{248}Cm embedded in KCl, in pioneering experiments performed with pre-EUROBALL arrays [23, 145, 389], as shown in Fig. 56.

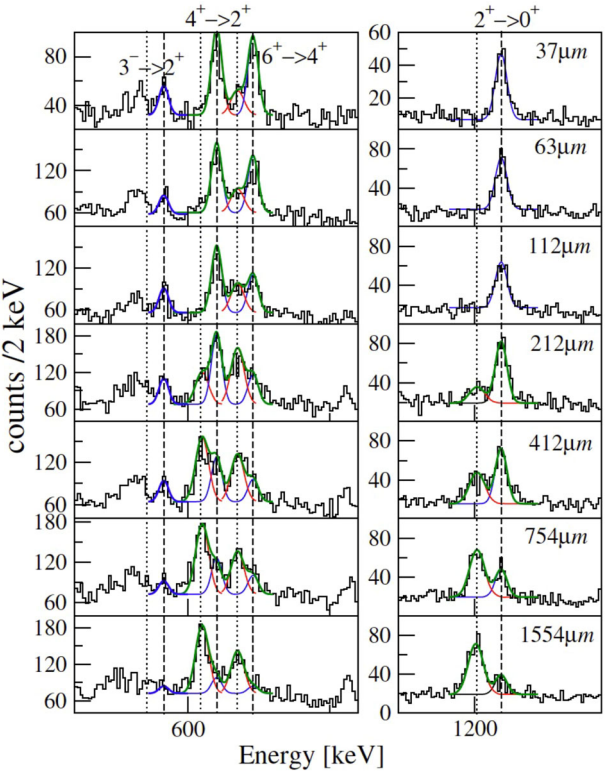

Fig. 55 Example of differential plunger measurements for γ-rays emitted by fission fragments produced by a beam of ^{238}U (6.2 MeV/u) impinging on a ^{9}Be target. The $2^+ \rightarrow 0^+$, $4^+ \rightarrow 2^+$, $6^+ \rightarrow 4^+$ and $3^- \rightarrow 2^+$ transitions of ^{98}Zr are shown as detected by the EXOGAM array (at various target-to-degrader distances). The spectra are Doppler corrected using the velocity measured in VAMOS++ after the degrader. Dotted and dashed lines indicate the positions of the shifted and unshifted components, respectively. Individual Gaussian fits to the shifted (red) and unshifted (blue) components are also shown, together with the total fits to the spectra (green lines). The extracted half-lives are $T_{1/2}$ = 2.63 (55) ps, 5.2(10) ps and 1.80(62) ps for the 2^+, 4^+ and 6^+ state, respectively (taken from [173])

7.5 g-factor measurements

Techniques have been developed to perform perform g-factor measurements of excited states using spontaneous fission sources in conjunction with a large array of Ge. A first pioneering experiment was performed by Smith et al., [390] with EUROBALL, and allowed to determine a number of g factors of 2^+ states in the A$\sim$100 region [20]. The method involved the direct implantation of the fission fragments into a thin foil of a ferromagnetic host (Gd or Fe), which was magnetized by a pair of small permanent magnets, as shown in Fig. 57a–b. In this type of experiments the fragment direction is not measured, therefore the Larmor precession angle of the nuclear magnetic moments is determined via the measurement of perturbed $\gamma - \gamma$ angular correlations, as displayed in Fig. 57b.

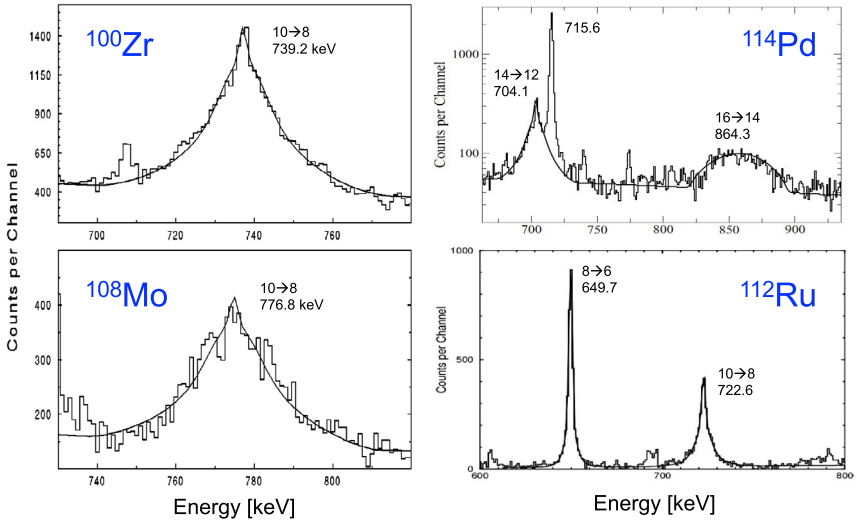

Fig. 56 Examples of analysis of line shapes corresponding to the decay of medium spin yrast states (from 8^+ to 16^+) of ^{100}Zr, ^{108}Mo, ^{112}Ru and ^{114}Pd, measured with EUROGAM-2 following spontaneous fission of ^{248}Cm. The data are represented by histograms and the fit by solid lines. The extracted half-lives are $T_{1/2}$ = 0.75(8) ps (10^+ state of ^{100}Zr), 0.77(13) ps (10^+ state of ^{108}Mo), 1.84(27) and 1.05(16) ps (8^+ and 10^+ state of ^{112}Ru, respectively), and 1.05(17) and 0.45(8) ps ((14^+) and (16^+) state of ^{114}Pd, respectively). (Adapted from [23, 145])

An alternative technique was developed by Daniel et al., [391] and applied to the analysis of spontaneous fission data from ^{252}Cf, measured with GAMMASPHERE. In this case, the fission fragments are stopped in an unmagnetized iron foil and the g factor is deduced from the attenuations of the angular correlations caused by the hyperfine fields in the iron lattice. The method relies on high-statistics triple γ coincidences and it is limited to state lifetimes which are much longer than the fragment stopping time (which is about few picoseconds), to avoid transient field effects. As discussed in Sect. 2.1.1, g factors of excited states in several neutron-rich nuclei in the ^{132}Sn region were determined with this approach [84, 86].

Measurements of g factors can also be performed at relativistic energies. Figure 58a shows a schematic layout of the FRS separator and RISING set-up (with a drawing of the magnet in (b)) for the GSI experimental campaign devoted to g-factor measurements of relativistic isomeric beams produced by fragmentation and ^{238}U fission. With this set-up, for the first time, spin alignment was established in a relativistic fission reaction, thus giving strong support to subsequent g-factor measurements [286], as discussed in Sect. 2.6.

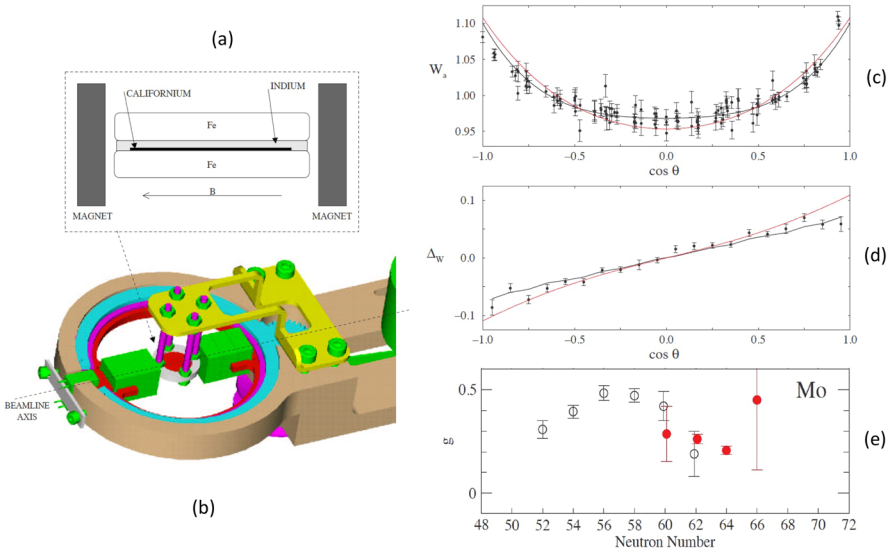

Fig. 57 Panels (**a**) and (**b**): sketch of the apparatus used with EUROBALL for g-factor measurements of excited states of spontaneous fission fragments from ^{252}Cf. Panel (**c**): example of perturbed E2-E2 γ-ray angular correlation of the $4^+ \rightarrow 2^+ \rightarrow 2^+ \rightarrow 0^+$ cascade in ^{104}Mo, as a function of the cosine of the angle θ between the γ rays. Panel (**d**): Corresponding measurement of the Larmor precession angle via the use of the double-ratios technique, which eliminates uncertainties in detector efficiencies. Panel (**e**): survey of g-factor measurements of 2^+ states in neutron-rich Mo isotopes (red symbols for the present technique). Similar data were obtained for neutron-rich Rb and Pd isotopes (taken from [20])

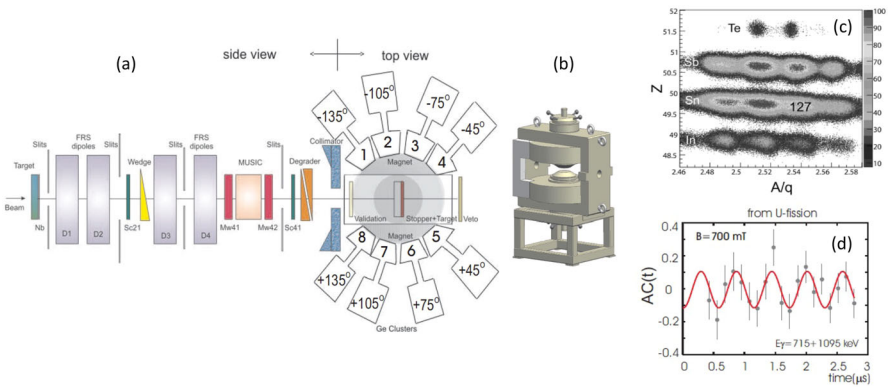

Fig. 58 Schematic layout of the FRS and RISING set-up (**a**) and drawing of the magnet (**b**), as employed at GSI during the g-factor experimental campaign using U relativistic fission. Panel (**c**) shows the isotopes selection in a U-fission reaction, while panel (**d**) displays the analysis of the $R(t)$ function for the $(19/2^+)$ isomer in ^{127}Sn, from which the spin alignment has been established for the first time (the $R(t)$ function is constructed by combining the decay curves measured for individual detectors with opposite directions of the vertically applied magnetic field) (adapted from [286])

8 Conclusion and perspectives

In recent years, simultaneous developments in both fission induced in inverse kinematics with separator technology at in-flight facilities, and fission induced by thermal and fast neutrons in direct kinematics, have produced a wealth of new complementary experimental information. However, the story of γ-ray spectroscopy of nuclear fission is far from over. A number of promising new avenues are emerging which will help to further exploit this crucial reaction mechanism and extract information from the γ-rays emitted in the process from exotic neutron-rich nuclei.

- *Twin branch spectroscopy*
  Promising technical developments are on the horizon which intend to exploit the possibility of treating the two fission fragments differently. For example by using a separator to characterize the mass and charge of one fragment, while performing prompt spectroscopy of the other. The phase II of the FIPPS project will use this technique to detect and characterize one fragment in a gas filled magnet (GFM) with high acceptance and high sensitivity, while stopped γ-rays from prompt decay at the target position will be detected in the γ ray spectrometer with high resolution [392]. A similar idea also lies behind the construction of a second branch to detect and perform spectroscopy of the partner fragment at the VAMOS/EXOGAM setup at GANIL.
- *Fission with γ-tracking arrays*
  In recent years, the unprecedented energy resolution capabilities offered by γ-tracking arrays like AGATA, coupled to large acceptance spectrometer such as VAMOS at GANIL, have allowed a significant step forward in spectroscopic studies of fully identified fission fragments in inverse kinematics reactions. A rich experimental program, making use of Pb and U beams on C targets, is now foreseen at Legnaro National Laboratory of INFN with the AGATA array (with enhanced efficiency), coupled with the PRISMA large solid angle magnetic spectrometer [393, 394]. Both dynamical and structure properties will be studied exploiting in particular transfer-induced fission, selected by tagging the C-like target ions with a coincident Si-detector array (the technique has been recently demonstrated by Ramos et al., in GANIL [395]). Such a powerful setup opens the possibility to explore production yields and spectroscopic properties of very neutron-rich nuclei by selecting the events with low excitation energy, thus minimizing secondary effects like neutron evaporation. The proposed measurements are expected to assess the limits of in-beam γ-ray spectroscopy with fission reactions in the poorly known ^{78}Ni region, in particular for the Se, Ge, Ga and possibly Zn isotopes around N = 50.
- *Active targets for lifetime measurements in the sub-picosecond range*
  Photopeak line shape fitting as a method of determining the very shortest lifetimes in the sub ps range has barely began to be explored. The pioneering experiments of Smith and collaborators [145] showed the promise of this tehcnique, which is now subsequently being developed with the use of active targets at the FIPPS setup at the ILL reactor.

– *Detection of short lived isomers in fission*
While the large-scale facilities have unprecedented selectivity for studying microsecond (or longer) isomeric states in very exotic nuclei at separator focal planes, the technique is constrained by the flight times of the nuclei through separators over several 10's of meters which are the order of several hundred nanoseconds. A complementary approach is to use beam pulsation techniques in the hundreds of ns range to detect shorter-lived isomeric states. Such techniques have been successfully used in particular at the nu-Ball/LICORNE setup at the ALTO facility in Orsay [31].
– *Dedicated fast-timing array for fission fragments*
To date, few fast-timing arrays have been built, often used in hybrid (Ge/$LaBr_3$) configurations, as for example nu-ball, ROSPHERE and FATIMA [31, 396–398]. However, while Ge arrays have been retrofitted with several $LaBr_3$ scintillators to combine selectivity from the high energy resolution of germanium detectors with the fast-timing properties of fast scintillators, the detector ratios have not been optimal. To optimise the number of Ge-$Labr_3$-$LaBr_3$ coincidences requires substantially more scintillator efficiency than germanium efficiency. An optimised hybrid setup would have an $LaBr_3$ efficiency of approximately double that of the germanium efficiency. An alternative promising avenue would be instead to better develop the buncher technology employed at some facilities (e.g., Canberra University or ALTO facility Tandem accelerators). Reducing the pulse width from the ns range to the 100 ps range (similar to the intrinsic time resolution of fast scintillators) would permit instead the exclusive use of Ge-$LaBr_3$-BeamPulse coincidences and achieve an unprecedented sensitivity to directly measure lifetimes of very weak transitions from nuclear states.
– *Multi observable fission experiments*
While ionisation chambers are well-developed technology at neutron facilities to detect the mass, kinetic energy and direction of fission fragments, their coupling to high resolution, high efficiency germanium spectrometers has not yet been attempted. The latest generation of position-sensitive ionisation chambers [399] would allow to collect an impressive range of multi-observable data on an event-by-event basis. This would facilitate a deeper understanding of the fission process, where the correlations between variables (e.g., γ-ray angular distributions with respect to the fission axis) could be exploited. Moreover, it could also provide a large increase in selectivity for the spectroscopy of spontaneous fission sources since the mass resolution of 3–4 mass units would reduce the background created by the other fragments by perhaps a factor of 30 or more.
– *High energy γ-rays from collective vibrational modes in fission (PDR, GDR)*
A key open question is related to the high-energy γ rays in fission which may be emitted by highly collective modes of excitation in fission fragments such as Giant Dipole Resonances (GDR) and Pygmy Dipole Resonances (PDR). Bump structures have been observed in the prompt fission γ-ray spectra of spontaneous fission sources between 3 and 8 MeV [400, 401]. Which particular fragments emit these γ rays and the origin of these de-excitations remains unclear. Moreover, there is very little experimental information about the evolution of these high-energy spectral components as a function of the mass and charge of the fragments.

– *Fission isomer spectroscopy*
As noted in the previous Sect. 4, very promising avenues exist for spectroscopy of the decay of states within the second potential energy minimum of these shape isomers and their decay back to the first minimum. The lowest mass actinides where the outer fission barrier is higher than the inner barrier (Th, U and Np nuclei) would be the most promising region to study to understand these exotic states sitting on the pathway to nuclear fission.
– *Exploitation of the photofission mechanism for prompt decay studies*
Photofission is a fission reaction mechanism which is used successfully as part of the ISOL technique at the TRIUMF and ALTO facilities. In the future, when the high beam flux of the quasi-monoenergetic γ beams of the ELI-NP facility come online, photofission as a production mechanism for prompt decay studies will become a reality along with new opportunities to study fission reaction mechanism induced by high-energy photons [402].

Supplementary Information The online version contains supplementary material available at https://doi.org/10.1007/s40766-022-00033-2.

Acknowledgements The authors acknowledge the AGATA, FIPPS and nu-ball collaborations which provided a large fraction of the most recent experimental results discussed in this review.

Funding Open access funding provided by Università degli Studi di Milano within the CRUI-CARE Agreement.

References

1. I. Ahmad, W.R. Phillips, Rep. Prog. Phys. **58**(11), 1415 (1995). https://doi.org/10.1088/0034-4885/58/11/002
2. J.H. Hamilton et al., Prog. Part. Nucl. Phys. **35**, 635 (1995). https://doi.org/10.1016/0146-6410(95)00048-N
3. J. Eberth, J. Simpson, Prog. Part. Nucl. Phys. **60**(2), 283 (2008). https://doi.org/10.1016/j.ppnp.2007.09.001
4. I.Y. Lee, M.A. Deleplanque, K. Vetter, Rep. Prog. Phys. **66**, 1095 (2003). https://doi.org/10.1088/0034-4885/66/7/201
5. E.M. Pell, J. Appl. Phys. **31**(2), 291 (1960). https://doi.org/10.1063/1.1735561
6. D.V. Freck, J. Wakefield, Nature **193**(4816), 669 (1962). https://doi.org/10.1038/193669a0
7. H.R. Bowman, S.G. Thompson, J.O. Rasmussen, Phys. Rev. Lett. **12**, 195 (1964). https://doi.org/10.1103/PhysRevLett.12.195
8. E. Cheifetz, R.C. Jared, S.G. Thompson, J.B. Wilhelmy, Phys. Rev. Lett. **25**, 38 (1970). https://doi.org/10.1103/PhysRevLett.25.38
9. J.B. Wilhelmy, S.G. Thompson, R.C. Jared, E. Cheifetz, Phys. Rev. Lett. **25**, 1122 (1970). https://doi.org/10.1103/PhysRevLett.25.1122

10. E. Cheifetz, J.B. Wilhelmy, R.C. Jared, S.G. Thompson, Phys. Rev. C **4**, 1913 (1971). https://doi.org/10.1103/PhysRevC.4.1913
11. J.B. Wilhelmy et al., Phys. Rev. C **5**, 2041 (1972). https://doi.org/10.1103/PhysRevC.5.2041
12. W.R. Phillips et al., Phys. Rev. Lett. **57**, 3257 (1986). https://doi.org/10.1103/PhysRevLett.57.3257
13. W. Phillips et al., Phys. Lett. B **212**(4), 402 (1988). https://doi.org/10.1016/0370-2693(88)91787-X
14. J. Leigh et al., Phys. Lett. B **159**(1), 9 (1985). https://doi.org/10.1016/0370-2693(85)90109-1
15. Y. Abdelrahman et al., Phys. Lett. B **199**(4), 504 (1987). https://doi.org/10.1016/0370-2693(87)91617-0
16. G.M. Ter-Akopian et al., Phys. Rev. Lett. **73**, 1477 (1994). https://doi.org/10.1103/PhysRevLett.73.1477
17. P. Nolan, F. Beck, D.B. Fossan, Annu. Rev. Nucl. Part. Sci. **45**(1), 561 (1994). https://doi.org/10.1146/annurev.ns.44.120194.003021
18. J. Simpson, Z. Phys. A **358**, 139 (1997). https://doi.org/10.1007/s002180050290
19. G. de Angelis, A. Bracco, D. Curien, Europhys. News **34**, 181 (2003). https://doi.org/10.1051/epn:2003503
20. W. Korten, S. Lunardi, Achievements with the EUROBALL spectrometer, Scientific and Technical Activity Report 1997-2003 (2003). Available at http://euroball.lnl.infn.it/EBmore/EB_Final_Report.pdf
21. M.A. Delaplanque, R.M.D. (Eds.), Gammasphere Proposal, Preprint LBNL-5202 (1997)
22. R. Krücken et al., Phys. Rev. C **64**, 017305 (2001). https://doi.org/10.1103/PhysRevC.64.017305
23. A.G. Smith et al., Phys. Rev. C **86**, 014321 (2012). https://doi.org/10.1103/PhysRevC.86.014321
24. J. Genevey et al., Phys. Rev. C **59**, 82 (1999). https://doi.org/10.1103/PhysRevC.59.82
25. J.A. Pinston, J. Genevey, J. Phys. G: Nucl. Part. Phys. **30**(2), R57 (2004). https://doi.org/10.1088/0954-3899/30/2/r02
26. B. Fogelberg et al., Nucl. Instrum. Methods Phys. Res. B **70**(1), 137 (1992). https://doi.org/10.1016/0168-583X(92)95921-D
27. H. Lawin et al., Nuc. Instr. Methods **137**(1), 103 (1976). https://doi.org/10.1016/0029-554X(76)90255-X
28. E. Moll, H. Schrader, G. Siegert, Kerntechnik und Atompraxis **19**, 374 (1977)
29. M. Jentschel et al., J. Instr. **12**(11), P11003 (2017). https://doi.org/10.1088/1748-0221/12/11/p11003
30. C. Michelagnoli et al., Eur. Phys. J. Web Conf. **193**, 04009 (2018). https://doi.org/10.1051/epjconf/201819304009
31. M. Lebois et al., Nucl. Instrum. Methods Phys. Res. A **960**, 145 (2020). https://doi.org/10.1016/j.nima.2020.163580
32. M. Rejmund et al., Nucl. Instrum. Methods Phys. Res. A **646**, 184 (2011). https://doi.org/10.1016/j.nima.2011.05.007
33. S. Pullanhiotan et al., Nucl. Instrum. Methods Phys. Res. A **593**, 343 (2008). https://doi.org/10.1016/j.nima.2008.05.003
34. H. Geissel et al., Nucl. Instrum. Methods Phys. Res. B **70**(1), 286 (1992). https://doi.org/10.1016/0168-583X(92)95944-M
35. T. Kubo, Nucl. Instrum. Methods Phys. Res. B **204**, 97 (2003). https://doi.org/10.1016/S0168-583X(02)01896-7
36. National Nuclear Data Center, Brookhaven; (https://www.nndc.bnl.gov)
37. O. Sorlin, M.G. Porquet, Prog. Part. Nucl. Phys. **61**(2), 602 (2008). https://doi.org/10.1016/j.ppnp.2008.05.001
38. T. Otsuka et al., Rev. Mod. Phys. **92**, 015002 (2020). https://doi.org/10.1103/RevModPhys.92.015002
39. L. Olivier et al., Phys. Rev. Lett. **119**, 192501 (2017). https://doi.org/10.1103/PhysRevLett.119.192501
40. V. Vaquero et al., Phys. Rev. Lett. **124**, 022501 (2020). https://doi.org/10.1103/PhysRevLett.124.022501
41. E. Flynn et al., Phys. Rev. C **3**(6), 2371 (1971). https://doi.org/10.1103/PhysRevC.3.2371
42. M. Czerwiński et al., Phys. Rev. C **92**, 014328 (2015). https://doi.org/10.1103/PhysRevC.92.014328
43. F. Nowacki, A. Poves, E. Caurier, B. Bounthong, Phys. Rev. Lett. **117**, 272501 (2016). https://doi.org/10.1103/PhysRevLett.117.272501
44. J. Blomqvist, Acta Phys. Pol. B **30**, 697 (1999)
45. H. Grawe, K. Langanke, G. Martínez-Pinedo, Rep. Prog. Phys. **70**(9), 1525 (2007). https://doi.org/10.1088/0034-4885/70/9/r02

46. W. Urban et al., Phys. Rev. C **62**, 027301 (2000). https://doi.org/10.1103/PhysRevC.62.027301
47. W. Urban et al., Eur. Phys. J. A **5**(3), 239 (1999). https://doi.org/10.1007/s100500050280
48. P. Hoff et al., Phys. Rev. Lett. **77**, 1020 (1996). https://doi.org/10.1103/PhysRevLett.77.1020
49. M. Sanchez-Vega et al., Phys. Rev. C **60**, 024303 (1999). https://doi.org/10.1103/PhysRevC.60.024303
50. B. Fogelberg et al., Phys. Rev. C **70**, 034312 (2004). https://doi.org/10.1103/PhysRevC.70.034312
51. J. Taprogge et al., Phys. Rev. Lett. **112**, 132501 (2014). https://doi.org/10.1103/PhysRevLett.112.132501
52. K.L. Jones et al., Nature **465**(7297), 454 (2010). https://doi.org/10.1038/nature09048
53. J.M. Allmond et al., Phys. Rev. Lett. **112**, 172701 (2014). https://doi.org/10.1103/PhysRevLett.112.172701
54. P. Bhattacharyya et al., Phys. Rev. C **64**, 054312 (2001). https://doi.org/10.1103/PhysRevC.64.054312
55. G. Bocchi et al., Phys. Lett. B **760**, 273 (2016). https://doi.org/10.1016/j.physletb.2016.06.065
56. W. Urban et al., Phys. Rev. C **79**, 037304 (2009). https://doi.org/10.1103/PhysRevC.79.037304
57. J. Genevey et al., Eur. Phys. J. A **7**(4), 463 (2000). https://doi.org/10.1007/PL00013643
58. M. Górska et al., Phys. Lett. B **672**(4), 313 (2009). https://doi.org/10.1016/j.physletb.2009.01.027
59. P. Bhattacharyya et al., Phys. Rev. Lett. **87**, 062502 (2001). https://doi.org/10.1103/PhysRevLett.87.062502
60. D. Rosiak et al., Phys. Rev. Lett. **121**, 252501 (2018). https://doi.org/10.1103/PhysRevLett.121.252501
61. P. Bhattacharyya et al., Phys. Rev. C **56**, R2363 (1997). https://doi.org/10.1103/PhysRevC.56.R2363
62. B. Fornal et al., Phys. Rev. C **63**, 024322 (2001). https://doi.org/10.1103/PhysRevC.63.024322
63. R. Lozeva et al., Phys. Rev. C **98**, 024323 (2018). https://doi.org/10.1103/PhysRevC.98.024323
64. J.K. Hwang et al., Phys. Rev. C **65**, 034319 (2002). https://doi.org/10.1103/PhysRevC.65.034319
65. C.T. Zhang et al., Z. Phys. A **358**(1), 9 (1997). https://doi.org/10.1007/s002180050269
66. C.T. Zhang et al., Phys. Rev. Lett. **77**, 3743 (1996). https://doi.org/10.1103/PhysRevLett.77.3743
67. S. Biswas et al., Phys. Rev. C **93**, 034324 (2016). https://doi.org/10.1103/PhysRevC.93.034324
68. J. Genevey et al., Eur. Phys. J. A **9**(2), 191 (2000). https://doi.org/10.1007/s100500070036
69. A. Astier et al., Phys. Rev. C **85**, 064316 (2012). https://doi.org/10.1103/PhysRevC.85.064316
70. A. Astier et al., Phys. Rev. C **87**, 054316 (2013). https://doi.org/10.1103/PhysRevC.87.054316
71. A. Astier et al., Phys. Rev. C **89**, 034310 (2014). https://doi.org/10.1103/PhysRevC.89.034310
72. S.H. Liu et al., Phys. Rev. C **80**, 044314 (2009). https://doi.org/10.1103/PhysRevC.80.044314
73. J.P. Schiffer, W.W. True, Rev. Mod. Phys. **48**, 191 (1976). https://doi.org/10.1103/RevModPhys.48.191
74. D. Nesterenko et al., Phys. Lett. B **808**, 135642 (2020). https://doi.org/10.1016/j.physletb.2020.135642
75. A. Korgul, et al., Eur. Phys. J. A **7**(2) (2000). https://doi.org/10.1007/PL00013594
76. A. Jungclaus et al., Phys. Rev. Lett. **99**, 132501 (2007). https://doi.org/10.1103/PhysRevLett.99.132501
77. A. Scherillo et al., Phys. Rev. C **70**, 054318 (2004). https://doi.org/10.1103/PhysRevC.70.054318
78. A. Jungclaus et al., Phys. Rev. C **93**, 041301 (2016). https://doi.org/10.1103/PhysRevC.93.041301
79. D. Kameda et al., Phys. Rev. C **86**, 054319 (2012). https://doi.org/10.1103/PhysRevC.86.054319
80. R. Machleidt, F. Sammarruca, Y. Song, Phys. Rev. C **53**, R1483 (1996). https://doi.org/10.1103/PhysRevC.53.R1483
81. L. Coraggio, A. Covello, A. Gargano, N. Itaco, T. Kuo, Prog. Part. Nucl. Phys. **62**(1), 135 (2009). https://doi.org/10.1016/j.ppnp.2008.06.001
82. L. Coraggio, A. Covello, A. Gargano, N. Itaco, Phys. Rev. C **80**, 021305 (2009). https://doi.org/10.1103/PhysRevC.80.021305
83. N. Cieplicka-Oryńczak et al., Phys. Lett. B **802**, 135222 (2020). https://doi.org/10.1016/j.physletb.2020.135222
84. S.H. Liu et al., Phys. Rev. C **81**, 014316 (2010). https://doi.org/10.1103/PhysRevC.81.014316
85. G. Neyens, Rep. Prog. Phys. **66**(4), 633 (2003). https://doi.org/10.1088/0034-4885/66/4/205
86. C. Goodin et al., Phys. Rev. C **78**, 044331 (2008). https://doi.org/10.1103/PhysRevC.78.044331
87. A. Korgul et al., Eur. Phys. Jour. A **15**(1), 181 (2002). https://doi.org/10.1140/epja/i2001-10250-8
88. M.G. Porquet et al., Eur. Phys. J. A **40**(2), 131 (2009). https://doi.org/10.1140/epja/i2008-10740-1
89. G.S. Simpson et al., Phys. Rev. C **76**, 041303 (2007). https://doi.org/10.1103/PhysRevC.76.041303
90. G. Häfner et al., Phys. Rev. C **103**, 034317 (2021). https://doi.org/10.1103/PhysRevC.103.034317

91. G. Häfner et al., Phys. Rev. C **104**, 014316 (2021). https://doi.org/10.1103/PhysRevC.104.014316
92. P. Spagnoletti et al., Phys. Rev. C **95**, 021302 (2017). https://doi.org/10.1103/PhysRevC.95.021302
93. S. Ilieva et al., Phys. Rev. C **94**, 034302 (2016). https://doi.org/10.1103/PhysRevC.94.034302
94. G. Simpson et al., J. Phys. G: Nucl. Part. Phys. **46**(6), 065108 (2019). https://doi.org/10.1088/1361-6471/ab1a75
95. B.A. Brown, et al., OXBASH Code, Technical Report No. 524, MSU- NSCL (1985). Available at ftp://ftp.nscp.msu.edu/pub/oxbash
96. B. Brown, W. Rae, Nucl. Data Sheets **120**, 115 (2014). https://doi.org/10.1016/j.nds.2014.07.022
97. E. Caurier, G. Martínez-Pinedo, F. Nowacki, A. Poves, A.P. Zuker, Rev. Mod. Phys. **77**, 427 (2005). https://doi.org/10.1103/RevModPhys.77.427
98. L.W. Iskra et al., Phys. Rev. C **89**, 044324 (2014). https://doi.org/10.1103/PhysRevC.89.044324
99. A. Astier et al., Phys. Rev. C **85**, 054316 (2012). https://doi.org/10.1103/PhysRevC.85.054316
100. R. Lucas et al., Eur. Phys. J. A **15**(3), 315 (2002). https://doi.org/10.1140/epja/i2002-10042-8
101. S. Biswas et al., Phys. Rev. C **99**, 064302 (2019). https://doi.org/10.1103/PhysRevC.99.064302
102. S. Biswas et al., Phys. Rev. C **102**, 014326 (2020). https://doi.org/10.1103/PhysRevC.102.014326
103. M. Rejmund et al., Phys. Lett. B **753**, 86 (2016). https://doi.org/10.1016/j.physletb.2015.11.077
104. R. Banik et al., Phys. Rev. C **102**, 044329 (2020). https://doi.org/10.1103/PhysRevC.102.044329
105. Y.H. Kim et al., Eur. Phys. J. A **53**(8), 162 (2017). https://doi.org/10.1140/epja/i2017-12353-y
106. R. Broda et al., Phys. Rev. Lett. **68**, 1671 (1992). https://doi.org/10.1103/PhysRevLett.68.1671
107. J.A. Pinston et al., Phys. Rev. C **61**, 024312 (2000). https://doi.org/10.1103/PhysRevC.61.024312
108. R.L. Lozeva et al., Phys. Rev. C **77**, 064313 (2008). https://doi.org/10.1103/PhysRevC.77.064313
109. J. Dudouet et al., Phys. Rev. C **100**, 011301 (2019). https://doi.org/10.1103/PhysRevC.100.011301
110. T. Rząca-Urban, W. Urban, J.L. Durell, A.G. Smith, I. Ahmad, Phys. Rev. C **76**, 027302 (2007). https://doi.org/10.1103/PhysRevC.76.027302
111. A. Prévost et al., Eur. Phys. J. A **22**(3), 391 (2004). https://doi.org/10.1140/epja/i2004-10063-3
112. E. Sahin et al., Nucl. Phys. A **893**, 1 (2012). https://doi.org/10.1016/j.nuclphysa.2012.08.007
113. P. Bączyk et al., Phys. Rev. C **91**, 047302 (2015). https://doi.org/10.1103/PhysRevC.91.047302
114. M.G. Porquet et al., Eur. Phys. J. A **39**(3), 295 (2009). https://doi.org/10.1140/epja/i2008-10723-2
115. J. Kurpeta et al., Phys. Rev. C **85**, 027302 (2012). https://doi.org/10.1103/PhysRevC.85.027302
116. J. Hakala et al., Phys. Rev. Lett. **101**, 052502 (2008). https://doi.org/10.1103/PhysRevLett.101.052502
117. W. Huang, M. Wang, F. Kondev, G. Audi, S. Naimi, Chin. Phys. C **45**(3), 030002 (2021). https://doi.org/10.1088/1674-1137/abddb0
118. M. Wang, W. Huang, F. Kondev, G. Audi, S. Naimi, Chin. Phys. C **45**(3), 030003 (2021). https://doi.org/10.1088/1674-1137/abddaf
119. M. Moinester, J.P. Schiffer, W.P. Alford, Phys. Rev. **179**, 984 (1969). https://doi.org/10.1103/PhysRev.179.984
120. A. Astier et al., Eur. Phys. J. A **30**(3), 541 (2006). https://doi.org/10.1140/epja/i2006-10151-4
121. B.M. Nyakó et al., Phys. Rev. C **103**, 034304 (2021). https://doi.org/10.1103/PhysRevC.103.034304
122. M. Czerwiński et al., Phys. Rev. C **93**, 034318 (2016). https://doi.org/10.1103/PhysRevC.93.034318
123. I.N. Gratchev et al., Phys. Rev. C **95**, 051302 (2017). https://doi.org/10.1103/PhysRevC.95.051302
124. W. Urban et al., Phys. Rev. C **94**, 044328 (2016). https://doi.org/10.1103/PhysRevC.94.044328
125. D. Montanari et al., Phys. Lett. B **697**(4), 288 (2011). https://doi.org/10.1016/j.physletb.2011.01.046
126. D. Montanari et al., Phys. Rev. C **85**, 044301 (2012). https://doi.org/10.1103/PhysRevC.85.044301
127. G. Bocchi et al., Phys. Rev. C **89**, 054302 (2014). https://doi.org/10.1103/PhysRevC.89.054302
128. S. Bottoni et al., Phys. Rev. C **103**, 014320 (2021). https://doi.org/10.1103/PhysRevC.103.014320
129. S. Leoni, A. Bracco, G. Colò, B. Fornal, Eur. Phys. J. A **55**, 247 (2019). https://doi.org/10.1140/epja/i2019-12925-9
130. B. Alex Brown, Phys. Rev. C **58**, 220 (1998). https://doi.org/10.1103/PhysRevC.58.220
131. S. Bottoni et al., Acta Phys. Pol. B **50**, 285 (2019). https://doi.org/10.5506/APhysPolB.50.285
132. K. Heyde, J.L. Wood, Rev. Mod. Phys. **83**, 1467 (2011). https://doi.org/10.1103/RevModPhys.83.1467
133. K. Wimmer et al., Phys. Rev. Lett. **105**, 252501 (2010). https://doi.org/10.1103/PhysRevLett.105.252501
134. S. Leoni et al., Phys. Rev. Lett. **118**, 162502 (2017). https://doi.org/10.1103/PhysRevLett.118.162502
135. N. Marginean et al., Phys. Rev. Lett. **125**, 102502 (2020). https://doi.org/10.1103/PhysRevLett.125.102502

136. C. Kremer et al., Phys. Rev. Lett. **117**, 172503 (2016). https://doi.org/10.1103/PhysRevLett.117.172503
137. P.E. Garrett et al., Phys. Rev. Lett. **123**, 142502 (2019). https://doi.org/10.1103/PhysRevLett.123.142502
138. A.N. Andreyev et al., Nature **405**, 430 (2000). https://doi.org/10.1038/35013012
139. S.G. Nilsson, I. Ragnarsson, *Shapes and Shells in Nuclear Structure* (Cambridge University Press, Cambridge, 1995)
140. D. Arseniev, A. Sobiczewski, V. Soloviev, Nuc. Phys. A **139**(2), 269 (1969). https://doi.org/10.1016/0375-9474(69)91109-9
141. W. Urban et al., Nuc. Phys. A **689**, 605 (2001). https://doi.org/10.1016/S0375-9474(00)00612-6
142. W. Urban et al., Eur. Phys. J. A **22**(2), 241 (2004). https://doi.org/10.1140/epja/i2004-10037-5
143. J.M. Régis et al., Phys. Rev. C **95**, 054319 (2017). https://doi.org/10.1103/PhysRevC.95.054319
144. S. Ansari et al., Phys. Rev. C **96**, 054323 (2017). https://doi.org/10.1103/PhysRevC.96.054323
145. A.G. Smith et al., Phys. Rev. Lett. **77**, 1711 (1996). https://doi.org/10.1103/PhysRevLett.77.1711
146. A. Navin et al., Phys. Lett. B **728**, 136 (2014). https://doi.org/10.1016/j.physletb.2013.11.024
147. L.W. Iskra et al., Phys. Rev. C **102**, 054324 (2020). https://doi.org/10.1103/PhysRevC.102.054324
148. Ł.W. Iskra et al., EPL (Europhys. Lett.) **117**(1), 12001 (2017). https://doi.org/10.1209/0295-5075/117/12001
149. W. Urban et al., Phys. Rev. C **96**, 044333 (2017). https://doi.org/10.1103/PhysRevC.96.044333
150. E.H. Wang et al., Phys. Rev. C **103**, 034301 (2021). https://doi.org/10.1103/PhysRevC.103.034301
151. M. Matejska-Minda et al., Phys. Rev. C **80**, 017302 (2009). https://doi.org/10.1103/PhysRevC.80.017302
152. W. Urban et al., Eur. Phys. J. A **16**(1), 11 (2003). https://doi.org/10.1140/epja/i2002-10104-y
153. J.A. Pinston et al., Phys. Rev. C **71**, 064327 (2005). https://doi.org/10.1103/PhysRevC.71.064327
154. M. Rudigier et al., Phys. Rev. C **87**, 064317 (2013). https://doi.org/10.1103/PhysRevC.87.064317
155. C.Y. Wu et al., Phys. Rev. C **70**, 064312 (2004). https://doi.org/10.1103/PhysRevC.70.064312
156. A. Esmaylzadeh et al., Phys. Rev. C **100**, 064309 (2019). https://doi.org/10.1103/PhysRevC.100.064309
157. A. Złomaniec et al., Phys. Rev. C **72**, 067302 (2005). https://doi.org/10.1103/PhysRevC.72.067302
158. L. Bettermann et al., Phys. Rev. C **82**, 044310 (2010). https://doi.org/10.1103/PhysRevC.82.044310
159. G.S. Simpson et al., Phys. Rev. C **74**, 064308 (2006). https://doi.org/10.1103/PhysRevC.74.064308
160. T. Rząca-Urban et al., Phys. Rev. C **98**, 064315 (2018). https://doi.org/10.1103/PhysRevC.98.064315
161. G.S. Simpson et al., Phys. Rev. C **82**, 024302 (2010). https://doi.org/10.1103/PhysRevC.82.024302
162. I. Tsekhanovich et al., Phys. Rev. C **78**, 011301 (2008). https://doi.org/10.1103/PhysRevC.78.011301
163. W. Urban et al., Phys. Rev. C **85**, 014329 (2012). https://doi.org/10.1103/PhysRevC.85.014329
164. C.J. Pearson, B.J. Varley, W.R. Phillips, J.L. Durell, Rev. Sci. Inst. **66**, 3367 (1995). https://doi.org/10.1063/1.1145509
165. R.B. Gerst et al., Phys. Rev. C **102**, 064323 (2020). https://doi.org/10.1103/PhysRevC.102.064323
166. M. Albers et al., Phys. Rev. Lett. **108**, 062701 (2012). https://doi.org/10.1103/PhysRevLett.108.062701
167. M. Albers et al., Nuc. Phys. A **899**, 1 (2013). https://doi.org/10.1016/j.nuclphysa.2013.01.013
168. J.M. Régis et al., Phys. Rev. C **90**, 067301 (2014). https://doi.org/10.1103/PhysRevC.90.067301
169. J. Genevey et al., Phys. Rev. C **73**, 037308 (2006). https://doi.org/10.1103/PhysRevC.73.037308
170. C. Lizarazo et al., Phys. Rev. Lett. **124**, 222501 (2020). https://doi.org/10.1103/PhysRevLett.124.222501
171. T. Rząca-Urban et al., Phys. Rev. C **79**, 024319 (2009). https://doi.org/10.1103/PhysRevC.79.024319
172. J. Dudouet et al., Phys. Rev. Lett. **118**, 162501 (2017). https://doi.org/10.1103/PhysRevLett.118.162501
173. P. Singh et al., Phys. Rev. Lett. **121**, 192501 (2018). https://doi.org/10.1103/PhysRevLett.121.192501
174. T. Rząca-Urban et al., Phys. Rev. C **95**, 064302 (2017). https://doi.org/10.1103/PhysRevC.95.064302
175. C. Delafosse et al., Phys. Rev. Lett. **121**, 192502 (2018). https://doi.org/10.1103/PhysRevLett.121.192502
176. T. Materna et al., Phys. Rev. C **92**, 034305 (2015). https://doi.org/10.1103/PhysRevC.92.034305
177. M. Hotchkis et al., Nuc. Phys. A **530**, 111 (1991). https://doi.org/10.1016/0375-9474(91)90758-X
178. J. Skalski, S. Mizutori, W. Nazarewicz, Nuc. Phys. A **617**(3), 282 (1997). https://doi.org/10.1016/S0375-9474(97)00125-5

179. P. Möller, A. Sierk, R. Bengtsson, H. Sagawa, T. Ichikawa, At. Data Nucl. Data Tab. **98**(2), 149 (2012). https://doi.org/10.1016/j.adt.2010.09.002
180. S. Hilaire, M. Girod, Eur. Phys. J. A **33**(2), 237 (2007). https://doi.org/10.1140/epja/i2007-10450-2
181. A. Petrovici, Phys. Rev. C **85**, 034337 (2012). https://doi.org/10.1103/PhysRevC.85.034337
182. T. Togashi, Y. Tsunoda, T. Otsuka, N. Shimizu, Phys. Rev. Lett. **117**, 172502 (2016). https://doi.org/10.1103/PhysRevLett.117.172502
183. J.K. Hwang et al., Phys. Rev. C **67**, 014317 (2003). https://doi.org/10.1103/PhysRevC.67.014317
184. K. Sieja, F. Nowacki, K. Langanke, G. Martínez-Pinedo, Phys. Rev. C **79**, 064310 (2009). https://doi.org/10.1103/PhysRevC.79.064310
185. J.E. García-Ramos, K. Heyde, Phys. Rev. C **102**, 054333 (2020). https://doi.org/10.1103/PhysRevC.102.054333
186. W. Urban et al., Phys. Rev. C **102**, 064321 (2020). https://doi.org/10.1103/PhysRevC.102.064321
187. J.F. Sharpey-Schafer et al., Eur. Phys. J. A **55**(2), 15 (2019). https://doi.org/10.1140/epja/i2019-12665-x
188. R.F. Casten, Nat. Phys. **2**(12), 811 (2006). https://doi.org/10.1038/nphys451
189. P. Koseoglou et al., Phys. Rev. C **101**, 014303 (2020). https://doi.org/10.1103/PhysRevC.101.014303
190. T. Otsuka, Y. Tsunoda, T. Abe, N. Shimizu, P. Van Duppen, Phys. Rev. Lett. **123**, 222502 (2019). https://doi.org/10.1103/PhysRevLett.123.222502
191. G.S. Simpson et al., Phys. Rev. C **80**, 024304 (2009). https://doi.org/10.1103/PhysRevC.80.024304
192. E. Ideguchi et al., Phys. Rev. C **94**, 064322 (2016). https://doi.org/10.1103/PhysRevC.94.064322
193. Z. Patel et al., Phys. Lett. B **753**, 182 (2016). https://doi.org/10.1016/j.physletb.2015.12.026
194. C. Gautherin et al., Eur. Phys. J. A **1**, 391 (1998). https://doi.org/10.1007/s100500050074
195. P. Walker, G. Dracoulis, Nature **399**(6731), 35 (1999). https://doi.org/10.1038/19911
196. V. Vandone et al., Phys. Rev. C **88**, 034312 (2013). https://doi.org/10.1103/PhysRevC.88.034312
197. R. Yokoyama et al., Phys. Rev. C **95**, 034313 (2017). https://doi.org/10.1103/PhysRevC.95.034313
198. Z. Patel et al., Phys. Rev. C **96**, 034305 (2017). https://doi.org/10.1103/PhysRevC.96.034305
199. Z. Patel et al., Phys. Rev. Lett. **113**, 262502 (2014). https://doi.org/10.1103/PhysRevLett.113.262502
200. G. Zhang et al., Phys. Lett. B **799**, 135036 (2019). https://doi.org/10.1016/j.physletb.2019.135036
201. P.A. Söderström et al., Phys. Lett. B **762**, 404 (2016). https://doi.org/10.1016/j.physletb.2016.09.058
202. H. Watanabe et al., Phys. Lett. B **760**, 641 (2016). https://doi.org/10.1016/j.physletb.2016.07.057
203. M.R. Mumpower, G.C. McLaughlin, R. Surman, Phys. Rev. C **85**, 045801 (2012). https://doi.org/10.1103/PhysRevC.85.045801
204. A. Davydov, G. Filippov, Nuc. Phys. **8**, 237 (1958). https://doi.org/10.1016/0029-5582(58)90153-6
205. L. Wilets, M. Jean, Phys. Rev. **102**, 788 (1956). https://doi.org/10.1103/PhysRev.102.788
206. P. Möller et al., At. Data Nucl. Data Tab. **94**(5), 758 (2008). https://doi.org/10.1016/j.adt.2008.05.002
207. E. Grosse, A.R. Junghans, J.N. Wilson, Phys. Scr. **94**(1), 014008 (2018). https://doi.org/10.1088/1402-4896/aaec92
208. N. Zamfir, R. Casten, Phys. Lett. B **260**(3), 265 (1991). https://doi.org/10.1016/0370-2693(91)91610-8
209. S.W. Ødegård et al., Phys. Rev. Lett. **86**, 5866 (2001). https://doi.org/10.1103/PhysRevLett.86.5866
210. D.R. Jensen et al., Phys. Rev. Lett. **89**, 142503 (2002). https://doi.org/10.1103/PhysRevLett.89.142503
211. N. Sensharma et al., Phys. Rev. Lett. **124**, 052501 (2020). https://doi.org/10.1103/PhysRevLett.124.052501
212. T. Koike et al., J. Phys. G: Nucl. Part. Phys. **31**(10), S1741 (2005). https://doi.org/10.1088/0954-3899/31/10/065
213. S. Frauendorf, Rev. Mod. Phys. **73**, 463 (2001). https://doi.org/10.1103/RevModPhys.73.463
214. A.M. Forney et al., Phys. Rev. Lett. **120**, 212501 (2018). https://doi.org/10.1103/PhysRevLett.120.212501
215. A.D. Ayangeakaa et al., Phys. Rev. Lett. **123**, 102501 (2019). https://doi.org/10.1103/PhysRevLett.123.102501
216. J. Snyder et al., Phys. Lett. B **723**(1), 61 (2013). https://doi.org/10.1016/j.physletb.2013.04.046
217. H. Watanabe et al., Phys. Lett. B **704**(4), 270 (2011). https://doi.org/10.1016/j.physletb.2011.09.050
218. A. Guessous et al., Phys. Rev. Lett. **75**, 2280 (1995). https://doi.org/10.1103/PhysRevLett.75.2280
219. Y. Luo et al., Phys. Lett. B **670**(4), 307 (2009). https://doi.org/10.1016/j.physletb.2008.10.067
220. S. Lalkovski et al., Eur. Phys. J. A **18**(4), 589 (2003). https://doi.org/10.1140/epja/i2003-10098-x

221. E.R. Gamba et al., Phys. Rev. C **100**, 044309 (2019). https://doi.org/10.1103/PhysRevC.100.044309
222. A. Navin et al., Phys. Lett. B **767**, 480 (2017). https://doi.org/10.1016/j.physletb.2016.11.020
223. T.W. Hagen et al., Eur. Phys. J. A **54**(3), 50 (2018). https://doi.org/10.1140/epja/i2018-12482-9
224. T.W. Hagen et al., Phys. Rev. C **95**, 034302 (2017). https://doi.org/10.1103/PhysRevC.95.034302
225. H.B. Ding et al., Phys. Rev. C **74**, 054301 (2006). https://doi.org/10.1103/PhysRevC.74.054301
226. J. Wang et al., Nuc. Phys. A **834**(1), 94c (2010). https://doi.org/10.1016/j.nuclphysa.2010.01.028. The 10th International Conference on Nucleus-Nucleus Collisions (NN2009)
227. J. Ha et al., Phys. Rev. C **101**, 044311 (2020). https://doi.org/10.1103/PhysRevC.101.044311
228. W. Urban et al., Eur. Phys. J. A **20**(3), 381 (2004). https://doi.org/10.1140/epja/i2004-10023-y
229. A. Bohr, B.R. Mottelson, Nuclear Structure Vol. 1 and 2 (World Scientific Publishing, Singapore, 1999)
230. P. Garrett, J.L. Wood, S.W. Yates, Phys. Scr. **93**(6), 063001 (2018). https://doi.org/10.1088/1402-4896/aaba1c
231. C. Fahlander, A. Axelsson, M. Heinebrodt, T. Härtlein, D. Schwalm, Phys. Lett. B **388**(3), 475 (1996). https://doi.org/10.1016/S0370-2693(96)01203-8
232. Y. Tsunoda, T. Otsuka, Phys. Rev. C **103**, L021303 (2021). https://doi.org/10.1103/PhysRevC.103.L021303
233. J.A. Pinston et al., Phys. Rev. C **74**, 064304 (2006). https://doi.org/10.1103/PhysRevC.74.064304
234. A. Guessous et al., Phys. Rev. C **53**, 1191 (1996). https://doi.org/10.1103/PhysRevC.53.1191
235. R. Orlandi et al., Phys. Rev. C **73**, 054310 (2006). https://doi.org/10.1103/PhysRevC.73.054310
236. H. Hua et al., Phys. Rev. C **69**, 014317 (2004). https://doi.org/10.1103/PhysRevC.69.014317
237. Y.X. Luo et al., Phys. Rev. C **74**, 024308 (2006). https://doi.org/10.1103/PhysRevC.74.024308
238. G. Simpson et al., Phys. Rev. C **75**, 027301 (2007). https://doi.org/10.1103/PhysRevC.75.027301
239. A.M. Bruce et al., Phys. Rev. C **82**, 044312 (2010). https://doi.org/10.1103/PhysRevC.82.044312
240. M. Stoyer et al., Nuc. Phys. A **787**(1), 455 (2007). https://doi.org/10.1016/j.nuclphysa.2006.12.068. Proceedings of the Ninth International Conference on Nucleus-Nucleus Collisions
241. X.Q. Zhang et al., Phys. Rev. C **63**, 027302 (2001). https://doi.org/10.1103/PhysRevC.63.027302
242. Y.X. Luo et al., Phys. Rev. C **69**, 024315 (2004). https://doi.org/10.1103/PhysRevC.69.024315
243. J.A. Sheikh, K. Hara, Phys. Rev. Lett. **82**, 3968 (1999). https://doi.org/10.1103/PhysRevLett.82.3968
244. P.A. Butler, J. Phys. G: Nucl. Part. Phys. **43**(7), 073002 (2016). https://doi.org/10.1088/0954-3899/43/7/073002
245. Y. Cao et al., Phys. Rev. C **102**, 024311 (2020). https://doi.org/10.1103/PhysRevC.102.024311
246. F. Asaro, F. Stephens, I. Perlman, Phys. Rev. **92**, 1495 (1953). https://doi.org/10.1103/PhysRev.92.1495
247. F. Stephens, F. Asaro, I. Perlman, Phys. Rev. **96**, 1568 (1954). https://doi.org/10.1103/PhysRev.96.1568
248. F.S. Stephens, F. Asaro, I. Perlman, Phys. Rev. **100**, 1543 (1955). https://doi.org/10.1103/PhysRev.100.1543
249. N.F. Ramsey, Annu. Rev. Nucl. Part. Sci. **40**(1), 1 (1990). https://doi.org/10.1146/annurev.ns.40.120190.000245
250. J. Cocks et al., Nuc. Phys. A **645**, 61 (1999). https://doi.org/10.1016/S0375-9474(98)00586-7
251. P.A. Butler, W. Nazarewicz, Rev. Mod. Phys. **68**, 349 (1996). https://doi.org/10.1103/RevModPhys.68.349
252. G. Scamps, C. Simenel, Nature **564**(7736), 382 (2018). https://doi.org/10.1038/s41586-018-0780-0
253. S.J. Zhu et al., Phys. Rev. Lett. **124**, 032501 (2020). https://doi.org/10.1103/PhysRevLett.124.032501
254. W. Urban et al., Nuc. Phys. A **613**, 107 (1997). https://doi.org/10.1016/S0375-9474(96)00393-4
255. L.P. Gaffney et al., Nature **497**(7448), 199 (2013). https://doi.org/10.1038/nature12073
256. P.A. Butler et al., Nat. Commun. **10**(1), 2473 (2019). https://doi.org/10.1038/s41467-019-10494-5
257. B. Bucher et al., Phys. Rev. Lett. **118**, 152504 (2017). https://doi.org/10.1103/PhysRevLett.118.152504
258. B. Bucher et al., Phys. Rev. Lett. **116**, 112503 (2016). https://doi.org/10.1103/PhysRevLett.116.112503
259. R. Lică et al., Phys. Rev. C **97**, 024305 (2018). https://doi.org/10.1103/PhysRevC.97.024305
260. T. Rząca-Urban et al., Phys. Rev. C **87**, 031305 (2013). https://doi.org/10.1103/PhysRevC.87.031305
261. M. Jones et al., Nuc. Phys. A **605**(2), 133 (1996). https://doi.org/10.1016/0375-9474(96)00194-7
262. W. Urban et al., Phys. Rev. C **54**, 945 (1996). https://doi.org/10.1103/PhysRevC.54.945
263. Y.J. Chen et al., Phys. Rev. C **73**, 054316 (2006). https://doi.org/10.1103/PhysRevC.73.054316

264. T. Rzaca-Urban et al., Phys. Lett. B **348**, 336 (1995). https://doi.org/10.1016/0370-2693(95)00146-C
265. W. Urban et al., Eur. Phys. J. A **16**(3), 303 (2003). https://doi.org/10.1140/epja/i2002-10127-4
266. W. Urban et al., Phys. Rev. C **69**, 017305 (2004). https://doi.org/10.1103/PhysRevC.69.017305
267. W. Urban et al., Eur. Phys. J. A **8**(1), 5 (2000). https://doi.org/10.1007/s100500070113
268. T. Malkiewicz et al., Phys. Rev. C **85**, 044314 (2012). https://doi.org/10.1103/PhysRevC.85.044314
269. S. Bhattacharyya et al., Phys. Rev. C **98**, 044316 (2018). https://doi.org/10.1103/PhysRevC.98.044316
270. T. Rzaca-Urban et al., Eur. Phys. J. A **9**(2), 165 (2000). https://doi.org/10.1007/s100500070033
271. G.D. Dracoulis, P.M. Walker, F.G. Kondev, Rep. Prog. Phys. **79**(7), 076301 (2016). https://doi.org/10.1088/0034-4885/79/7/076301
272. T. Rząca-Urban et al., Phys. Rev. C **75**, 054319 (2007). https://doi.org/10.1103/PhysRevC.75.054319
273. H. Wollersheim et al., Nuc. Instr. Methods Phys. Res. A **537**(3), 637 (2005). https://doi.org/10.1016/j.nima.2004.08.072
274. P.A. Söderström, et al., Nuc. Instr. Methods Phys. Res. B **317**, 649 (2013). https://doi.org/10.1016/j.nimb.2013.03.018. XVIth International Conference on ElectroMagnetic Isotope Separators and Techniques Related to their Applications, December 2-7, 2012 at Matsue, Japan
275. V.H. Phong et al., Phys. Rev. C **100**, 011302 (2019). https://doi.org/10.1103/PhysRevC.100.011302
276. L. Cáceres et al., Phys. Rev. C **79**, 011301 (2009). https://doi.org/10.1103/PhysRevC.79.011301
277. A. Jungclaus et al., Phys. Lett. B **772**, 483 (2017). https://doi.org/10.1016/j.physletb.2017.07.006
278. J. Taprogge et al., Phys. Lett. B **738**, 223 (2014). https://doi.org/10.1016/j.physletb.2014.09.047
279. G.S. Simpson et al., Phys. Rev. Lett. **113**, 132502 (2014). https://doi.org/10.1103/PhysRevLett.113.132502
280. R. Lozeva et al., Phys. Rev. C **92**, 024304 (2015). https://doi.org/10.1103/PhysRevC.92.024304
281. R. Lozeva et al., Phys. Rev. C **93**, 014316 (2016). https://doi.org/10.1103/PhysRevC.93.014316
282. P.A. Söderström et al., Phys. Rev. C **92**, 051305 (2015). https://doi.org/10.1103/PhysRevC.92.051305
283. H. Watanabe et al., Phys. Lett. B **792**, 263 (2019). https://doi.org/10.1016/j.physletb.2019.03.053
284. H. Watanabe et al., Phys. Rev. Lett. **113**, 042502 (2014). https://doi.org/10.1103/PhysRevLett.113.042502
285. H. Watanabe et al., Phys. Rev. Lett. **111**, 152501 (2013). https://doi.org/10.1103/PhysRevLett.111.152501
286. G. Neyens et al., Acta Phys. Pol. B **38**(4), 1237 (2007)
287. G. Ilie et al., Phys. Lett. B **687**(4), 305 (2010). https://doi.org/10.1016/j.physletb.2010.03.033
288. M. Kmiecik et al., Eur. Phys. J. A **45**(2), 153 (2010). https://doi.org/10.1140/epja/i2010-11003-4
289. L. Atanasova et al., Europhys. Lett. **91**(4), 42001 (2010). https://doi.org/10.1209/0295-5075/91/42001
290. C. Theisen, et al., AIP Conf. Proc. **447**(143) (2008). https://doi.org/10.1063/1.56696
291. F. Kandzia et al., Eur. Phys. J. A **56**(8), 207 (2020). https://doi.org/10.1140/epja/s10050-020-00201-0
292. E.M. Burbidge, G.R. Burbidge, W.A. Fowler, F. Hoyle, Rev. Mod. Phys. **29**, 547 (1957). https://doi.org/10.1103/RevModPhys.29.547
293. F.K. Thielemann, M. Eichler, I. Panov, B. Wehmeyer, Annu. Rev. Nucl. Part. Sci. **67**(1), 253 (2017). https://doi.org/10.1146/annurev-nucl-101916-123246
294. C. Broggini et al., Riv. Nuovo Cim. **42**, 103 (2019). https://doi.org/10.1393/ncr/i2019-10157-1
295. M. Mumpower, R. Surman, G. McLaughlin, A. Aprahamian, Prog. Part. Nucl. Phys. **86**, 86 (2016). https://doi.org/10.1016/j.ppnp.2015.09.001
296. P. Möller, B. Pfeiffer, K.L. Kratz, Phys. Rev. C **67**(5), 055802 (2003). https://doi.org/10.1103/PhysRevC.67.055802
297. G. Lorusso et al., Phys. Rev. Lett. **114**, 192501 (2015). https://doi.org/10.1103/PhysRevLett.114.192501
298. J. Wu et al., Phys. Rev. Lett. **118**, 072701 (2017). https://doi.org/10.1103/PhysRevLett.118.072701
299. K.H. Schmidt, A. Kelić, S. Lukić, M.V. Ricciardi, M. Veselsky, Phys. Rev. ST Accel. Beams **10**, 014701 (2007). https://doi.org/10.1103/PhysRevSTAB.10.014701
300. UK Atomic Agency Authority, Fission Yields; https://fispact.ukaea.uk/nuclear-data/fission-yields/
301. K.H. Schmidt, B. Jurado, C. Amouroux, C. Schmitt, Nucl. Data Sheets **131**, 107 (2016). https://doi.org/10.1016/j.nds.2015.12.009
302. S. Shibagaki et al., Astron. J. **816**(2), 79 (2016). https://doi.org/10.3847/0004-637x/816/2/79

303. S. Goriely, Europhys. Phys. J. A **51**(2), 22 (2015). https://doi.org/10.1140/epja/i2015-15022-3
304. A. Tsinganis et al., Phys. Procedia **64**, 130 (2015). https://doi.org/10.1016/j.phpro.2015.04.017
305. S. Polikanov et al., Soy. Phys. JETP **15**, 1016 (1962)
306. S. Bjørnholm, J. Borggreen, L. Westgaard, V. Karnaukhov, Nucl. Phys. A **95**(3), 513 (1967). https://doi.org/10.1016/0375-9474(67)90846-9
307. V. Strutinsky, Nucl. Phys. A **95**(2), 420 (1967). https://doi.org/10.1016/0375-9474(67)90510-6
308. V. Metag, D. Habs, H. Specht, Phys. Rep. **65**(1), 1 (1980). https://doi.org/10.1016/0370-1573(80)90006-X
309. S. Bjørnholm, J.E. Lynn, Rev. Mod. Phys. **52**, 725 (1980). https://doi.org/10.1103/RevModPhys.52.725
310. D. Pansegrau et al., Phys. Lett. B **484**, 1 (2000). https://doi.org/10.1016/S0370-2693(00)00638-9
311. P. Reiter, PhD. Thesis University of Heidelberg (1988)
312. J. Schirmer, J. Gerl, D. Habs, D. Schwalm, Phys. Rev. Lett. **63**, 2196 (1989). https://doi.org/10.1103/PhysRevLett.63.2196
313. P. Thirolf, D. Habs, Prog. Part. Nucl. Phys. **49**(2), 325 (2002). https://doi.org/10.1016/S0146-6410(02)00158-8
314. S.J.P. Delaroche, M. Girod, H. Goutte, J. Libert, Nucl. Phys. A **771**, 103 (2006). https://doi.org/10.1016/j.nuclphysa.2006.03.004
315. P. Jachimowicz, M. Kowal, J. Skalski, Phys. Rev. C **85**, 034305 (2012). https://doi.org/10.1103/PhysRevC.85.034305
316. B. Nerlo-Pomorska, K. Pomorski, J. Bartel, C. Schmitt, Eur. Phys. J. A **53**(4), 1 (2017). https://doi.org/10.1140/epja/i2017-12259-8
317. J. Randrup, P. Möller, Phys. Rev. Lett. **106**, 132503 (2011). https://doi.org/10.1103/PhysRevLett.106.132503
318. A. Chebboubi et al., Eur. Phys. J. A **57**(12), 335 (2021). https://doi.org/10.1140/epja/s10050-021-00645-y
319. K.H. Schmidt, J. Benlliure, A. Junghans, Nucl. Phys. A **693**(1), 169 (2001). https://doi.org/10.1016/S0375-9474(01)00648-0
320. A. Dey et al., Phys. Rev. C **103**, 044322 (2021). https://doi.org/10.1103/PhysRevC.103.044322
321. A. Bogachev et al., Eur. Phys. J. A **34**(1), 23 (2007). https://doi.org/10.1140/epja/i2007-10485-3
322. P. Banerjee et al., Phys. Rev. C **92**, 024318 (2015). https://doi.org/10.1103/PhysRevC.92.024318
323. G.M. Ter-Akopian et al., Phys. Rev. C **55**, 1146 (1997). https://doi.org/10.1103/PhysRevC.55.1146
324. G.M. Ter-Akopian et al., Phys. Atom. Nucl. **67**(10), 1860 (2004). https://doi.org/10.1134/1.1811191
325. D. Fong et al., Phys. Atom. Nucl. **69**(7), 1161 (2006). https://doi.org/10.1134/S1063778806070118
326. G.M. Ter-Akopian et al., Phys. Rev. Lett. **77**, 32 (1996). https://doi.org/10.1103/PhysRevLett.77.32
327. B.M. Musangu et al., Phys. Rev. C **101**, 034610 (2020). https://doi.org/10.1103/PhysRevC.101.034610
328. W. Younes et al., Phys. Rev. C **64**, 054613 (2001). https://doi.org/10.1103/PhysRevC.64.054613
329. J.N. Wilson et al., Phys. Rev. Lett. **118**, 222501 (2017). https://doi.org/10.1103/PhysRevLett.118.222501
330. N. Fotiades et al., Phys. Rev. C **99**, 024606 (2019). https://doi.org/10.1103/PhysRevC.99.024606
331. J. Wilson et al., EPJ Web Conf. **256**, 00019 (2021). https://doi.org/10.1051/epjconf/202125600019. (Barga, Belgium, September 24 - 26, 2019)
332. A. Andreyev, K. Nishio, K.H. Schmidt, Rep. Prog. Phys. **81**, 016301 (2018). https://doi.org/10.1088/1361-6633/aa82eb
333. M. Bender et al., J. Phys. G: Nucl. Part. Phys. **47**(11), 113002 (2020). https://doi.org/10.1088/1361-6471/abab4f
334. J. Shannon, PhD. Thesis University of Manchester (1995)
335. E. Kozulin, et al., AIP Conf. Proc. **853**(336) (2006). https://doi.org/10.1063/1.2338399
336. J.N. Wilson et al., Nature **590**(7847), 566 (2021). https://doi.org/10.1038/s41586-021-03304-w
337. P. Armbruster, H. Labus, K. Reichelt, Z. Naturforsch. A **26**(3), 512 (1971). https://doi.org/10.1515/zna-1971-0320
338. F. Pleasonton, Nuc. Phys. A **213**(2), 413 (1973). https://doi.org/10.1016/0375-9474(73)90161-9
339. A. Chebboubi et al., Phys. Lett. B **775**, 190 (2017). https://doi.org/10.1016/j.physletb.2017.10.067
340. M. Travar et al., Phys. Lett. B **817**, 136293 (2021). https://doi.org/10.1016/j.physletb.2021.136293
341. A. Bulgac et al., Phys. Rev. Lett. **116**, 122504 (2016). https://doi.org/10.1103/PhysRevLett.116.122504

342. K.H. Schmidt, B. Jurado, Phys. Rev. Lett. **104**, 212501 (2010). https://doi.org/10.1103/PhysRevLett.104.212501
343. A. Bulgac et al., Phys. Rev. Lett. **126**, 142502 (2021). https://doi.org/10.1103/PhysRevLett.126.142502
344. R. Vogt, J. Randrup, Phys. Rev. C **103**, 014610 (2021). https://doi.org/10.1103/PhysRevC.103.014610
345. J. Randrup, R. Vogt, Phys. Rev. Lett. **127**, 062502 (2021). https://doi.org/10.1103/PhysRevLett.127.062502
346. P. Marević, N. Schunck, J. Randrup, R. Vogt, Phys. Rev. C **104**, L021601 (2021). https://doi.org/10.1103/PhysRevC.104.L021601
347. I. Stetcu et al., Phys. Rev. Lett. **127**, 222502 (2021). https://doi.org/10.1103/PhysRevLett.127.222502
348. R.P. Schmitt et al., Phys. Atom. Nucl. **66**(6), 1163 (2003). https://doi.org/10.1134/1.1586431
349. G.G. Chubarian et al., Phys. Rev. Lett. **87**, 052701 (2001). https://doi.org/10.1103/PhysRevLett.87.052701
350. A.G. Smith et al., Phys. Rev. C **60**, 064611 (1999). https://doi.org/10.1103/PhysRevC.60.064611
351. The European Commission's Joint Research Centre (JRC) in Geel (Belgium); (https://ec.europa.eu/jrc/en/about/jrc-site/geel)
352. P.W. Lisowski, K.F. Schoenberg, Nucl. Instrum. Methods Phys. Res. A **562**(2), 910 (2006). https://doi.org/10.1016/j.nima.2006.02.178
353. The Budapest Research Reactor (BRR) in Hungary; https://www.bnc.hu/BRR
354. L. Tomlinson, At. Data Nucl. Data Tab. **12**(2), 179 (1973). https://doi.org/10.1016/0092-640X(73)90018-1
355. B. Ade, C. Gauld, Oak Ridge National Laboratory Report ORNL/TM-2011/290
356. O. Moreira, Ann. Nucl. Energy **39**(1), 62 (2012). https://doi.org/10.1016/j.anucene.2011.09.007
357. N. Cieplicka-Oryńczak et al., Phys. Rev. C **94**, 014311 (2016). https://doi.org/10.1103/PhysRevC.94.014311
358. B. Marchand et al., J. Nucl. Mat. **440**(1), 562 (2013). https://doi.org/10.1016/j.jnucmat.2013.04.005
359. M. Fallot et al., Phys. Rev. Lett. **109**, 202504 (2012). https://doi.org/10.1103/PhysRevLett.109.202504
360. G. Rimpault, et al., Physics Procedia **31**, 3 (2012). https://doi.org/10.1016/j.phpro.2012.04.002. GAMMA-1 Emission of Prompt Gamma-Rays in Fission and Related Topics
361. M. Lemaire et al., J. Nucl. Sci. Technol. **52**(9), 1093 (2015). https://doi.org/10.1080/00223131.2015.1009957
362. GenIV International Forum https://www.gen-4.org/gif/
363. A. Chyzh et al., Phys. Rev. C **87**, 034620 (2013). https://doi.org/10.1103/PhysRevC.87.034620
364. A. Oberstedt et al., Phys. Rev. C **87**(5), 051602 (2013). https://doi.org/10.1103/PhysRevC.87.051602
365. R. Billnert, F.J. Hambsch, A. Oberstedt, S. Oberstedt, Phys. Rev. C **87**, 024601 (2013). https://doi.org/10.1103/PhysRevC.87.024601
366. L. Qi et al., Phys. Rev. C **98**, 014612 (2018). https://doi.org/10.1103/PhysRevC.98.014612
367. National Data Center, Japan Atomic Energy Agency; https://wwwndc.jaea.go.jp
368. D. Biswas et al., Nucl. Instrum. Methods Phys. Res. A **703**, 163 (2013). https://doi.org/10.1016/j.nima.2012.11.132
369. M. Lebois, et al., Nucl. Instrum. Methods Phys. Res.A **735**, 145 (2014). https://doi.org/10.1016/j.nima.2013.07.061
370. J. Wilson, M. Lebois, P. Halipre, S. Oberstedt, A. Oberstedt, Phys. Proc. **59**, 31 (2014). https://doi.org/10.1016/j.phpro.2014.10.005
371. N. Fotiades et al., Phys. Rev. C **69**, 024601 (2004). https://doi.org/10.1103/PhysRevC.69.024601
372. S. Akkoyun et al., Nucl. Instr. Methods Phys. Res. A **668**, 26 (2012). https://doi.org/10.1016/j.nima.2011.11.081
373. W. Korten et al., Eur. Phys. J. A **56**, 137 (2020). https://doi.org/10.1140/epja/s10050-020-00132-w
374. A. Bracco, G. Duchêne, Z. Podolyák, P. Reiter, Prog. Part. Nucl. Phys. **121**, 103887 (2021). https://doi.org/10.1016/j.ppnp.2021.103887
375. S. Paschalis et al., Nucl. Instrum. Methods Phys. Res. A **709**, 44 (2013). https://doi.org/10.1016/j.nima.2013.01.009
376. P. Fallon, A. Gade, I.Y. Lee, **66**(1), 321 (2016). https://doi.org/10.1146/annurev-nucl-102115-044834
377. B. Bruyneel et al., Nucl. Instrum. Methods Phys. Res. A **608**, 99 (2009). https://doi.org/10.1016/j.nima.2009.06.037
378. B. Bruyneel et al., Eur. Phys. J. A **49**, 61 (2013). https://doi.org/10.1140/epja/i2013-13061-4

379. T. Ohnishi et al., J. Phys. Soc. Jpn. **79**(7), 073201 (2010). https://doi.org/10.1143/JPSJ.79.073201
380. P. Talou et al., Phys. Rev. C **94**, 064613 (2016). https://doi.org/10.1103/PhysRevC.94.064613
381. G. Häfner, PhD. Thesis University of Paris-Saclay (2021)
382. J.M. Régis et al., Nucl. Instrum. Methods Phys. Res. A **763**, 210 (2014). https://doi.org/10.1016/j.nima.2014.06.004
383. E. Gamba, A. Bruce, M. Rudigier, Nucl. Instrum. Methods Phys. Res. A **928**, 93 (2019). https://doi.org/10.1016/j.nima.2019.03.028
384. S. Bottoni, et al., in preparation
385. H.T.S. Jared, R.C.; Nifenecker, International Atomic Energy Agency (IAEA) (1974)
386. G. Mamane, E. Cheifetz, E. Dafni, A. Zemel, J. Wilhelmy, Nucl. Phys. A **454**(2), 213 (1986). https://doi.org/10.1016/0375-9474(86)90265-4
387. A.G. Smith et al., J. Phys. G: Nucl. Part. Phys. **28**(8), 2307 (2002). https://doi.org/10.1088/0954-3899/28/8/316
388. J. Ljungvall et al., Nucl. Instrum. Methods Phys. Res. A **679**, 61 (2012). https://doi.org/10.1016/j.nima.2012.03.041
389. A.G. Smith et al., Phys. Rev. Lett. **73**, 2540 (1994). https://doi.org/10.1103/PhysRevLett.73.2540
390. A. Smith et al., Phys. Lett. B **453**(3), 206 (1999). https://doi.org/10.1016/S0370-2693(99)00332-9
391. A. Daniel et al., Nucl. Instr. Methods Phys. Res B **262**(2), 399 (2007). https://doi.org/10.1016/j.nimb.2007.06.008
392. Y. Kim et al., Nuc. Instr. Methods Phys. Res B **463**, 269 (2020). https://doi.org/10.1016/j.nimb.2019.05.022
393. A. Stefanini et al., Nucl. Phys. A **701**(1), 217 (2002). https://doi.org/10.1016/S0375-9474(01)01578-0
394. D. Montanari et al., Eur. Phys. J. A **47**(1), 4 (2011). https://doi.org/10.1140/epja/i2011-11004-9
395. D. Ramos et al., Phys. Rev. C **97**, 054612 (2018). https://doi.org/10.1103/PhysRevC.97.054612
396. D. Bucurescu et al., Nucl. Instrum. Methods Phys. Res. A **837**, 1 (2016). https://doi.org/10.1016/j.nima.2016.08.052
397. M. Rudigier et al., Nucl. Instrum. Methods Phys. Res. A **969**, 163967 (2020). https://doi.org/10.1016/j.nima.2020.163967
398. M. Rudigier et al., Acta Phys. Pol. B **48**, 351 (2017). https://doi.org/10.5506/APhysPolB.48.351
399. A. Gook et al., Nuc. Instr. Methods Phys. Res. A **830**, 366 (2016). https://doi.org/10.1016/j.nima.2016.06.002
400. A. Hotzel et al., Z. Phys. A **356**(1), 299 (1996). https://doi.org/10.1007/BF02769233
401. H. Makii et al., Phys. Rev. C **100**, 044610 (2019). https://doi.org/10.1103/PhysRevC.100.044610
402. D.L. Balabanski et al., Eur. Phys. J. Web Conf. **193**, 04005 (2018). https://doi.org/10.1051/epjconf/201819304005